DISS. ETH NO. 24472

DEVELOPMENT OF PRE-CLINICAL AND CLINICAL POSITRON EMISSION TOMOGRAPHY DETECTORS

A thesis submitted to attain the degree of

DOCTOR OF SCIENCES of ETH ZURICH

(Dr. sc. ETH Zurich)

presented by

JANNIS NIKOLAUS RUDOLF FISCHER

M.Sc., Humboldt-Universität zu Berlin

born on 26.01.1988

citizen of Germany

accepted on the recommendation of

Prof. Dr. Günther Dissertori
Prof. Dr. Bruno Weber
Dr. Werner Lustermann

2017

JANNIS NIKOLAUS RUDOLF FISCHER

DEVELOPMENT OF PRE-CLINICAL AND CLINICAL POSITRON EMISSION TOMOGRAPHY DETECTORS

Meinen Eltern Karsten und Christine
Meiner Partnerin Friederike

ABSTRACT

This dissertation is about the development of two positron emission tomography (PET) scanners: Small Animal Fast Insert for mRi (SAFIR) and Brain PET (BPET). While the first is a preclinical insert for a magnetic resonance imaging (MRI) scanner with unprecedented temporal resolution designed for use with mice and rats, the latter is an application specific and cost-effective clinical brain scanner to aid the early diagnosis of Alzheimer's disease (AD).

The preclinical scanner's development is guided by Monte Carlo (MC) simulations and lab tests. Noise equivalent count rate, spatial resolution, and sensitivity are assessed and components are tested with respect to their coincidence resolving time (CRT) and MRI compatibility. Simulations following the National Electrical Manufacturers Association (NEMA) standard support the claim that the reference design can be used for the intended studies by the users. The results of the lab tests show that the selected components can deliver the necessary timing performance and at the same time work inside the harsh environment of the MRI with its strong magnetic field and regular radio frequency (RF) pulses without mutual interference.

For the clinical PET device, the performance of the device is studied by MC simulations as well. The results show reasonable spatial resolution and sensitivities with respect to the target application. Lab tests of photo-sensors of small size compared to the scintillating crystal's surface prove the possibility of a minimalistic approach with limited sensitive area.

ZUSAMMENFASSUNG

Diese Abhandlung beschreibt die Entwicklung zweier Positron-Emissions-Tomographen (PET): Dem vorklinischen SAFIR-Einsatz für einen Magnet-Resonanz-Tomographen (MRI) für Mäuse und Ratten und dem Brain-Positron-Emissions-Tomographen (BPET), einem anwendungsspezifischen und kosteneffizientem Gehirn-PET zur frühen Diagnose der Alzheimerschen Krankheit.

Die Entwicklung des vorklinischen SAFIR wird durch Monte-Carlo-Simulationen (MC) und Labortests gestützt. Rauschäquivalente Zählrate (NECR), Ortsauflösung und Sensitivität werden nach dem NEMA-Standard ermittelt und die Komponenten werden im Hinblick auf ihre Zeitauflösung in Koinzidenz (CRT) und ihre Kompatibilität mit dem MRI getestet. Die Resultate der Simulationen zeigen die Eignung des Referenzdesigns für die beabsichtigten Studien der zukünftigen Nutzer des SAFIR-Einsatzes. Ferner beweisen die Tests der ausgewählten Komponenten, dass sie ohne gegenseitige Störung für den Einsatz in der Umgebung des MRIs mit seinem starken magnetischen Feld und seinen regelmässigen Hochfrequenz (RF)-Pulsen geeignet sind.

Das klinische BPET-Gerät wurde ebenfalls mittels Monte-Carlo-Simulationen untersucht. Ortsauflösung und Sensitivität erlauben den Schluss, dass es sich für die beabsichtigte Anwendung eignen wird. Labormessungen mit einem kleinen Lichtsensor auf einer Seitenfläche eines szintillierenden Kristalles beweisen darüber hinaus, dass dieses minimalistische Konzept mit reduzierter lichtempfindlicher Oberfläche möglich ist.

ACKNOWLEDGMENTS

Doing research within the SAFIR collaboration and writing this dissertation has been a very instructive and wonderful experience. Even after more than three years of working on this topic, I am very excited about it and hope to continue working in the field. The described small-animal PET as well as the proposed BPET scanner will hopefully enable research for biologists and diagnostic tools for physicians, which were not available before.

I am very thankful to everyone who has supported and guided me during this challenging venture. First and foremost, I would like to thank my advisors at ETH Zurich for their continuous support. Günther Dissertori has given me the opportunity to work in his group, whose activities in SAFIR started almost at the same time as my PhD work. He never declined any question or request I could have with respect to my research, attending conferences and schools, and improving my understanding of the subject. Werner Lustermann was always ready to sit down and discuss my research with an open mind. I could greatly profit from his vast knowledge on detector design, production, and construction – in the fields of physics, electronics, and software. Bruno Weber was the initiator of both PET scanners and was always ready to answer questions about using the future scanners. I thank all of them for their guidance and expertise they shared with me.

This work would not have been possible without the many colleagues within the collaboration, the Institute for Particle Physics, and external supporters. Alfred Buck, Volker Commichau, Satish Dhawan, Peter Fischer, Kris Thielemans, and Charalampos Tsoumpas gave important hints to understanding many aspects of this work. Chiara Casella, Alexander S. Howard, Mikiko Ito, Josep F. Oliver, Paola Solevi, and Geoffrey Warnock were always supportive when taking and simulating data as well as discussing the results. My fellow students Max Ahnen, Simon Corrodi, Afroditi Eleftheriou, Astrik Jeitler, Parisa Khateri, Kevin Kramer, Christian Ritzer, Ilaria Sacco, and Quilin Wang often had similar tasks, questions, and problems, which could be resolved together. Without the engineering and technicians team comprising Robert Becker, Diogo R. di Calafiori, Lubomir Djambazov, Michael Dröge, Patrick Gomez, Christian Haller, Ulf Röser, Agnieszka Zagoździńska-Bochenek, and Bruno Zehr there would probably not be a single working piece of hardware and no steady supply of sweets and hot caffeinated beverages. Finally without the administrative pool with Gabriela Amstutz, Rosa Bächli, Caroline Keufer-Platz, Gabriele

Kogler, and Bettina Lareida, I would have often been lost in bureaucratic details.

Last but not least, I would like to thank those who have known and supported me for the longest time: My parents Karsten and Christine have shaped the path I am going down. Three years ago, my partner Friederike stepped into my life and has since gone down this road with me together. Thank you for your love and care. It is comforting to be able to always count on a large family with many brothers, grandparents, great-grandparents, aunts, uncles, friends, and many more, who I cannot name personally here.

This work was generously support through ETH Grant no. ETH-30 14-2.

CONTENTS

LIST OF FIGURES

LIST OF TABLES

LISTINGS

ACRONYMS

Abeta amyloid beta

AD Alzheimer's disease

ADC analog to digital converter

APD avalanche photo diode

ASIC application specific integrated circuit

ATOM analysis tool and online monitor

BER bit error ratio

BGO bismuth germanate

BPET Brain PET

Ce Cerium

CERN conseil européen pour la recherche nucléaire

CMOS complementary metal-oxide-semiconductor

CRT coincidence resolving time

CT computed tomography

CTW coincidence time window

DAQ data acquisition system

DC direct current

DDR double data rate

DOI depth of interaction

DUT device under test

EM expectation maximization

EMI electromagnetic interference

EPI echo-planar imaging

ESR enhanced specular reflector

FBK Fondazione Bruno Kessler

FBP filtered back projection

FBP3DRP filtered back projection 3D with re-projection

FDG fluordeoxyglucose

FIFO first in first out

FORE Fourier re-binning

FOV field of view

FPGA field programmable gate array

FWHM full width at half maximum

FWTM full width at tenth maximum

IBERT integrated bit error rate test

IC integrated circuit

GATE Geant4 application for emission tomography

JTAG Joint Task Action Group

LDO low dropout

LOR line of response

LSO lutetium oxyorthosilicate

LTCC low temperature co-fired ceramics

LVDS low voltage differential signaling

LYSO lutetium-yttrium oxyorthosilicate

MAP maximum a posteriori

MC Monte Carlo

MLEM maximum likelihood expectation maximization

MRI magnetic resonance imaging

MPPC multi pixel photon counter

NECR noise equivalent count rate

NEMA National Electrical Manufacturers Association

OSL one step late

PC personal computer

PCB printed circuit board

PDE photon detection efficiency

PDF probability density function

PET positron emission tomography

PETA position energy timing ASIC

PETA6SE single-ended PETA version 6

PiB Pittsburgh compound B

PLL phase-locked loop

PMT photo multiplier tube

PRBS pseudo random binary sequence

QA SNR quality assurance signal-to-noise

QE quantum efficiency

RF radio frequency

ROI region of interest

SAFIR Small Animal Fast Insert for mRi

SAS SAFIR analog signal

SBT SAFIR bias and temperature

SDIP SAFIR digital interface PETA

SDIS SAFIR digital interface STiC

SFP small form-factor pluggable

SI Système international d'unités

SiPM silicon photo multiplier

SNR signal to noise

SPAD single photon avalanche diode

SSRB single slice re-binning

SST SAFIR STiC

STiC SiPM Timing Chip

STIR Software for Tomographic Image Reconstruction

TAC time activity curve

TDC time-to-digital converter

TOFPET time-of-flight PET

ToT time over threshold

USB universal serial bus

VCO voltage controlled oscillator

Part I

THE BASICS

1 INTRODUCTION

Until the discovery of x-rays by Wilhelm Conrad Röntgen in 1895, physicists and physicians have found it both impossible and desirable to look inside of living organisms to study them non-invasively and in greater detail. Since the discovery of this "invisible light", the subject of medical imaging as been established as an important diagnostic and research subject. From the first x-ray images over 3D computed tomography (CT) images up to modern age magnetic resonance imaging (MRI) and positron emission tomography (PET), a long history of improvements and new developments has taken place. These three modalities can be divided into mostly anatomical (CT and MRI) and mostly functional imaging modalities (PET).

The advantage of PET is its intrinsically functional principle of operation, which will be described in detail in chapter 2. In short, PET devices measure the arrival times of the two 511 keV photons originating from an electron-positron annihilation in coincidence. This information is processed and used to reconstruct the spatial distribution of the substance emitting the positrons – the radiotracer – within the organism. In 4D PET, one is furthermore interested in the temporal evolution of the spatial radiotracer distribution – hence the additional dimension. This is typically visualized by time activity curves (TACs) of region of interests (ROIs), i.e. the quantitative activity values at several times in a specified region of the studied organism.

The Small Animal Fast Insert for mRi (SAFIR) scanner was envisioned to make previously impossible measurements possible for the first time. A prime use case will be the measurement of the oxygen uptake in the mouse brain. This has been previously measured by another measurement technique called betaprobe [1], where a probe is surgically inserted into the mouse brain to directly measure the emitted positrons from the tracer. The disadvantages are predominantly the invasive procedure as well as the lack of spatial resolution as only the activity value at a certain point is measured. However, the betaprobe measurements have shown the time scale on which the relevant processes take place. The requirement to a PET system capable of temporally resolving this TAC is a temporal resolution of a few seconds. Other preclinical PET scanners are not able to deliver such performance. The accuracy of a quantitative PET measurement is statistically limited by the number of counts detected from a given voxel by Poisson statistics $\delta N = 1/\sqrt{N}$. Typical activities for the operation of preclinical PET devices are smaller than 50 MBq. Assuming a fifth of this maximum activity (10 MBq) in the brain with a size of 1 cm^3, a

voxel size of $(0.67\,\mathrm{mm})^3$, a sensitivity of 10 %, and a desired accuracy of 1 %, the scan time has to be at least

$$t_{scan} \geqslant \frac{1\,\mathrm{cm}^3}{(1\,\%)^2 \cdot 10\,\mathrm{MBq} \cdot 10\,\% \cdot (0.67\,\mathrm{mm})^3} \approx 34\,\mathrm{s} \tag{1}$$

making it impossible to temporally resolve the TAC to the desired level of a few seconds. Additional count losses in the real system as well as the reduced activity at later times due to the decay of the radiotracer are not even taken into account. Since the sensitivity cannot be improved by an order of magnitude, a certain accuracy is desired, and the mouse brain ROI has a determined size, the only adjustable parameter left is the injected activity. If it were increased by a factor of ten without losing the additional counts in the measurement process, the scan time could be reduced by the same factor. This is the aim of the SAFIR project: to develop a scanner capable of handling injected activities of up to 500 MBq in mice and rats. Furthermore, the SAFIR scanner is designed as a PET insert, which can operate in a commercial Bruker BioSpec 70/30 USR MRI device with a 7 T magnet. This adds additional constraints on available space and compatibility requirements on the SAFIR scanner. Both modalities have to operate simultaneously without disturbing each other. This additional effort is taken to enable comparative studies using the images of both modalities, e.g. for a thorough validation of the functional MRI methods against the intrisically functional PET.

Beyond its preclinical usage, PET is an important tool for the diagnosis of diseases in the clinic. It is used for the early diagnosis of Alzheimer's disease (AD) [2, 3], i.e. the detection of amyloid beta (Abeta) plaques in the human cortex, which are suspected to cause the neurodegeneration referred to as AD [4]. With the advent of promising treatments for AD [5], a reliable and readily available diagnostic method is of prime importance. The development of Brain PET (BPET) will fulfill this requirement. As a dedicated and cost-effective PET scanner specifically designed for scanning the brain for Abeta depositions, it has the potential to revolutionize the field of pre-symptomatic AD diagnostic. With the result of the scan it can be decided if the prospective treatment is to be triggered.

The following chapter 2 explains the physical background of the PET detection process including the positron emission and detector technology. Simulation results for SAFIR and BPET of standardized performance measures for preclinical and clinical PET scanners such as spatial resolution and sensitivity are presented in chapter 3. The evaluation of essential electronics components with respect to their suitability for SAFIR are shown in chapter 4. Chapter 5 includes the presentation of the performance of different photo-sensors for BPET and the results from a high-rate test of the position energy timing ASIC (PETA) application specific integrated circuit (ASIC). The results are summarized in chapter 6.

2 THE PRINCIPLE OF PET

In this chapter I will describe the idea behind PET imaging and the necessary physical background to understand the important steps towards designing and building a PET scanner. As the goal is to find the spatial and temporal distribution of a positron emitting isotope by measuring the annihilation gamma photons – referred to as gammas in the following – in coincidence, the detector has to be able to detect these gammas. A typical PET detector such as the SAFIR or BPET scanner does this using scintillating crystals, photo-sensors, and a readout electronics system recording the time and energy information of the detected gamma for subsequent coincidence processing. The coincidence events are used to calculate an estimate of the original isotope distribution by means of tomographic image reconstruction. In the following sections the relevant details about the underlying physical processes, the scintillator, the photo-sensor, and image reconstruction techniques are presented. Whenever examples are presented, they are selected such as to be applicable to the SAFIR or BPET scanner design, e.g. lutetium oxyorthosilicate (LSO) as scintillating crystal material and silicon photo multipliers (SiPMs) as photo-sensor.

2.1 THE IDEA OF PET

The principle of PET was first developed by Michael Phelps and Michel Ter-Pogossian in the 1970s [6, 7]. PET imaging aims at finding the distribution of a certain molecule in an animal or human. PET is different from other tomographic modalities such as CT and MRI. The latter two modalities work with external stimuli: In CT, the transmission of externally applied radiation is measured and in MRI an external stimulus triggers a measurable nuclear spin resonance. In PET, however, the radiation is emitted within the body. The molecule to be tracked is labeled with a positron emitting radioactive isotope. The most common isotope is ^{18}F – often in fluordeoxyglucose (FDG), but also in many other tracers – although special applications make use of other isotopes such as ^{11}C or ^{15}O. The labeled molecules are injected into the animal, where they participate in the metabolism.

A positron emitted during a β^+ decay has a certain average range within the tissue depending on the positron kinetic energy and the type of tissue. The positron annihilates with an electron and two gammas with each 511 keV energy are emitted almost back-to-back. Although there might be a small acollinearity, the gammas can be approximated to be back-to-back. The process is illustrated in figure 1.

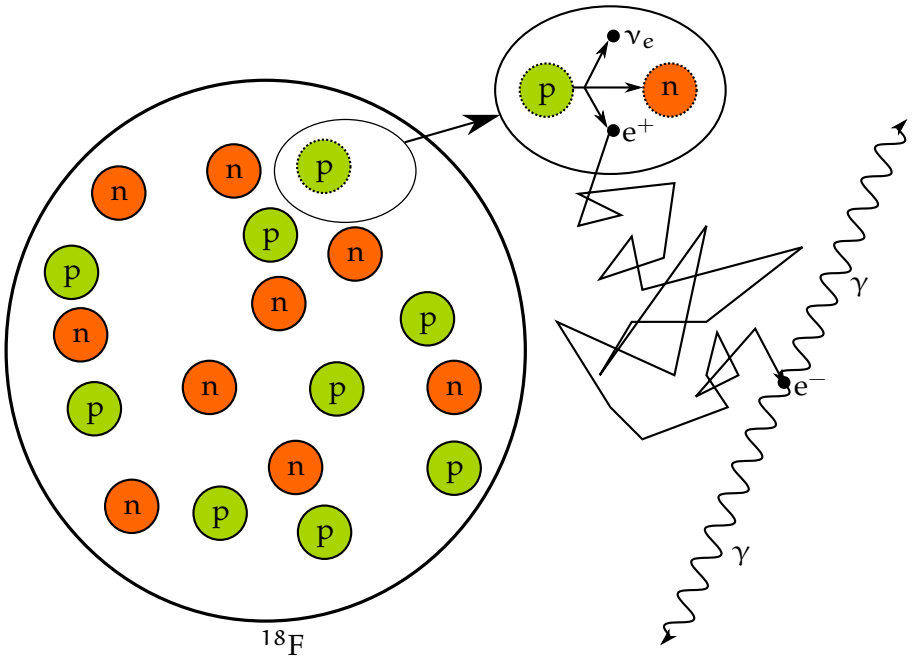

Figure 1: Illustration of the β^+ decay and the $e^+ - e^-$ annilation.

Detecting the two emitted gammas in coincidence is necessary to reconstruct the tracer distribution in a PET detector. This requires sufficiently precise timing of every detection element combined with a synchronization of the times between all elements. Otherwise no coincidence events can be found between detection elements. A single coincidence event with both gamma photons having photo-peak energy, i.e. 511 keV, carries the information that an annihilation has taken place along the line joining the two detection elements in coincidence. This line is called a line of response (LOR). The coincidence event carries no information about where along this line the two gammas originated from, unless time-of-flight techniques are employed [8]. However, even without time-of-flight information, it is possible to estimate the activity distribution, see section 2.5.

2.2 DETECTOR TECHNOLOGY – DETECTING A GAMMA

2.2.1 *Scattering and Absorption*

To detect a particle, the device used to do so has to interact with the particle to be detected. In the case of gammas, five effects are known for their interaction: photoelectric absorption, pair production in the proximity of a nucleus (nuclear pair production) or of an electron (electron pair production), and incoherent (Compton) and

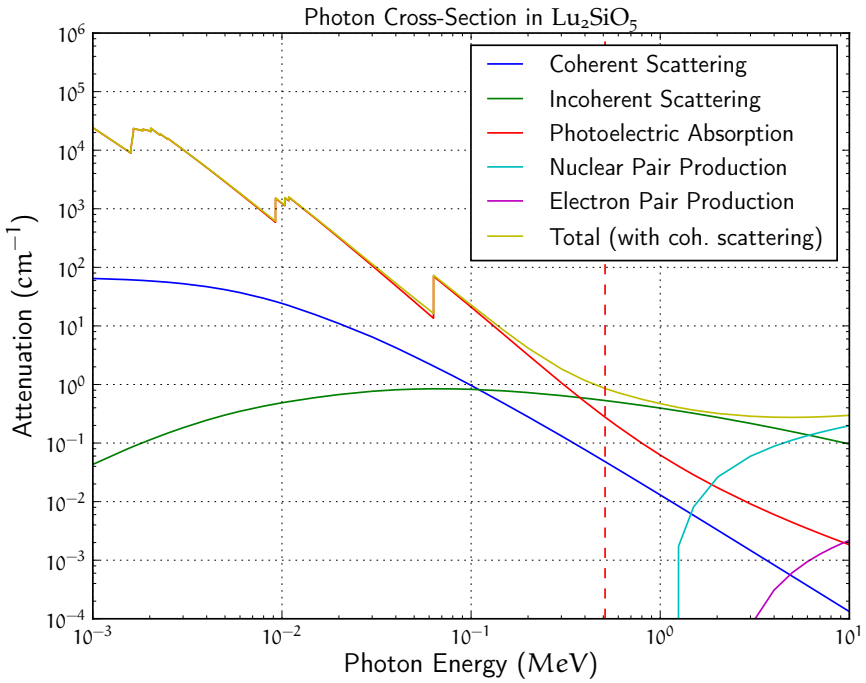

Figure 2: Photon cross-sections in Lu_2SiO_5 according to [9]. The dashed red line marks the energy of the 511 keV gamma.

coherent (Rayleigh) scattering. Thomson scattering is the low energy limit of Compton scattering and as such included in the Compton cross-section. The corresponding cross-sections in Lu_2SiO_5 (LSO [10]) are plotted for the energy relevant to PET in figure 2. LSO is used as an example because contrary to lutetium-yttrium oxyorthosilicate (LYSO) – a variant with an additional Yttrium component –, there is only a single manufacturer making the properties unique. The properties of LYSO are very similar to LSO, for a comprehensive list of scintillator properties see `http://scintillator.lbl.gov`. At the energy of an annihilation gamma, the dominant effects are Compton scattering (62.1 %) followed by photoelectric absorption (32.3 %). The Rayleigh scattering cross-section is approximately one order of magnitude smaller (5.6 %) and pair production is impossible since at least twice the energy would be necessary. In the following I will thus focus on photoelectric absorption and Compton scattering.

In both types of interaction, energy is transferred from the gamma to an electron in the material. This photo electron interacts with the matter further, most prominently by Cherenkov radiation ($\approx$ 14 photons per gamma [11]) and scintillation ($\approx$ 14000 photons per gamma [11]) in the energy range relevant to PET. Both are explained in more detail in the following subsections.

2.2.2 *Cherenkov Radiation*

Cherenkov radiation is emitted when a charged particle travels through a medium with a velocity greater than the speed of light in that medium. Since the emission of the photons is prompt, they are very useful to precisely measure the time of interaction. The discussion about and formulae for Cherenkov radiation are taken from [12]. The relevant parameter is the opening angle θ_c of the Cherenkov emission cone around the particle's track given by

$$\cos\theta_c = \frac{1}{n\beta}, \tag{2}$$

where n is the refractive index of the material and $\beta = \frac{v}{c}$ is the velocity of the particle in the medium with respect to the vacuum speed of light c. The Cherenkov photon yield per unit path length and per unit energy is given by

$$\frac{d^2N}{dxdE} = \frac{\alpha z^2}{\hbar c}\sin^2\theta_c \tag{3}$$

$$\approx 370\sin^2\theta_c(E)\,eV^{-1}\,cm^{-1} \quad (z=1) \tag{4}$$

or equivalently per unit wavelength λ

$$\frac{d^2N}{dxd\lambda} = \frac{2\pi\alpha z^2}{\lambda^2}\left(1 - \frac{1}{\beta^2 n^2(\lambda)}\right) \tag{5}$$

for a particle with charge ze, where α is the fine structure constant and $\hbar$ is the reduced Planck constant. Since the electron loses energy via scintillation processes, its velocity β decreases along the travelled path. Therefore, the formula only yields a maximum value if the change of velocity is not taken into account.

For LSO with refractive index $n = 1.82$, $z = 1$ for an electron, and a fixed electron kinetic energy of $511\,keV (\Leftrightarrow \beta = \frac{3}{4})$, the yield per unit wavelength and per unit travelled path is shown in figure 3 for fixed β. This is the case when the gamma has transferred all its energy to the electron in a photoelectric absorption. As mentioned in the beginning, Cherenkov radiation is not a dominant effect for the energy loss of the photo electron, which loses energy mainly by the processes involved in scintillation. It is however crucial to precision timing. Bremsstrahlung does not play a role because the energies are well below the critical energy $E_{crit,e^-} = 11.72\,MeV$ [13].

2.2.3 *Scintillation*

Several processes take place when the electron travels through the crystal [14]. The primary photo electron and its corresponding hole in the crystal lose energy by creating secondary electron-hole pairs in the crystal. A secondary x-ray or an electron are created by radiative

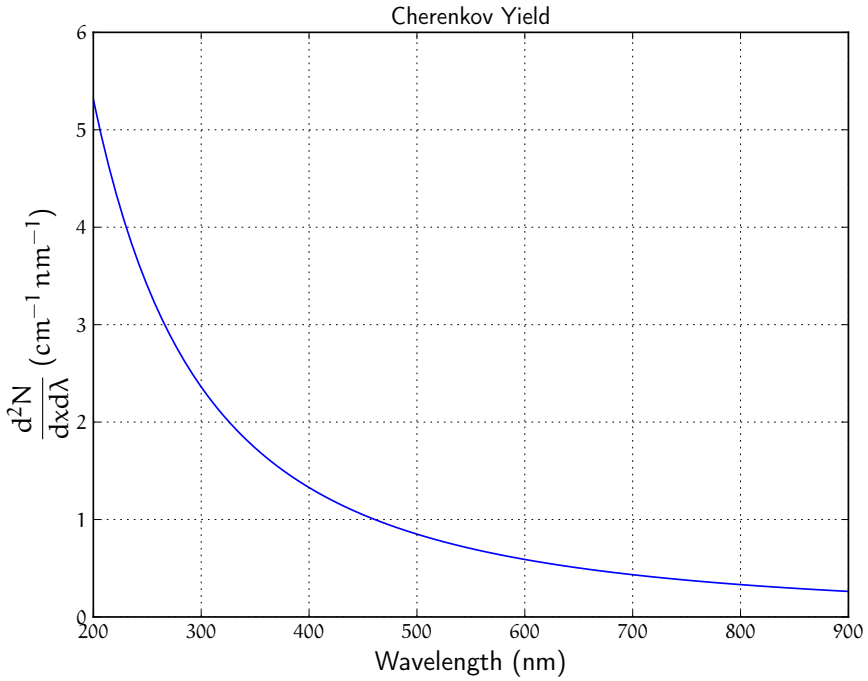

Figure 3: Differential Cherenkov yield in LSO as a function of the wavelength for $n = 1.82$, $z = 1$, and $\beta = \frac{3}{4}$.

decay or the Auger process, respectively. Given sufficient energy, the secondary x-ray generates more electron-hole pairs via the photoelectric or Compton effect. At energies above the ionization threshold, the secondary electron can create an electron-hole pair just as the primary photo electron, leading to a cascade. Furthermore, inelastic electron-electron scattering [15] takes place. At electron energies below the ionization threshold, the hot electrons thermalize by electron-phonon relaxation and by inducing band transitions.

Cerium (Ce)-doped LSO is a commonly used scintillator in PET. The dopant's single 4f electron is excited and the following transition through the 5d states to the ground state causes the emission of light in the visible range[1] [10]. The absolute average light output of LSO has been measured to be between 21 200 photons/MeV (0.02% Ce) [16], 22 200 photons/MeV (1.00% Ce) [16], and 29 000 photons/MeV [17], thus indeed many more than from Cherenkov radiation.

The decay of the excited states to the ground states with the release of the energy as optical scintillation photons follows an exponential

1 The transition energy from the lowest 5d state to the ground state (4f) is $\approx 3\,eV$, equivalent to an emission wavelength of $\approx 413\,nm$.

decay law, i.e. the rate of arriving photons λ per unit time t follows an exponential law

$$\frac{d\lambda}{dt} = -\frac{\lambda}{\tau} \tag{6}$$

$$\Rightarrow \lambda(t) = \frac{N}{\tau} e^{-t/\tau} \tag{7}$$

with scintillation time constant τ and a total light output of N photons. This will be used in the following subsection to deduce a limit on the achievable timing resolution.

2.2.4 *Photon Arrival Time Distribution*

The arrival of the individual scintillation photons is a stochastic process, which can be assumed to be Poissonian. Consequently, the arrival time of each photon has a probability distribution. In the following, I will introduce mathematical tools to calculate the mean and variance of arrival times to find the lower limit of the possible timing resolution.

2.2.4.1 *Poisson Processes*

The Poisson distribution with parameter λ is defined through the probability

$$P_{\lambda\Delta t}(k) = \frac{(\lambda\Delta t)^k}{k!} e^{-(\lambda\Delta t)}, \tag{8}$$

which is the probability of observing k events when on average $\lambda\Delta t$ events are expected within the observation interval Δt.

The following discussion uses some material from [18]. A process is called a Poisson process with intensity λ if the following three conditions are fulfilled:

1. The occurence of an event in the (sufficiently small) interval $[t, t + \Delta t]$ is independent of previous events (independence);
2. Within the interval $[t, t + \Delta t]$, there is at most one event (rareness);
3. The probability of finding an event within the interval $[t, t + \Delta t]$ is proportional to its length Δt with proportionality constant λ.

There is a large group of natural processes with Poissonian nature. Additionally, it is hard to "destroy" the Poisson property of a process, e.g. the radioactive decay is a Poisson process, but also the arrival of the gamma at the crystal and the arrival of the individual scintillation photons, independent of the physical processes leading to the photon being created and arriving at a photo-sensitive surface. If the parameter λ is constant, the Poisson process is called homogeneous

or stationary. In a generalization when $\lambda = \lambda(t)$, it is called inhomogeneous. For the following discussion, let $m(t) := \int_0^t \lambda(t')dt'$, which is often called the mean function. Please note that $\dot{m} := \frac{dm}{dt} = \lambda(t)$.

The distribution of the arrival time of the n-th photon can be calculated: Consider the probability of observing $n-1$ events of a Poisson process with rate $\lambda(t)$ in the time interval $[0, t]$

$$P_{m(t)}(n-1) = \frac{m^{n-1}(t)}{(n-1)!} e^{-m(t)}. \tag{9}$$

This expression can be reinterpreted to express the probability of t given n events. This leads to a probability density function (PDF), which after normalization[2] is

$$f_n(t) = \frac{m^{n-1}(t)}{(n-1)!} \lambda(t) e^{-m(t)}, \tag{10}$$

$$\text{or } f_n(u) = \frac{u^{n-1}}{(n-1)!} e^{-u}, \tag{11}$$

where $u := m(t)$ and in the second line, the density was transformed using the integral substitution rule eliminating the $\lambda(t)$.

The second step reveals an interesting property of the inhomogeneous Poisson, namely that it can be transformed into a homogeneous Poisson process with a time scale $u = m(t)$. The distribution function $f_n(u)$ is that of an Erlang distribution, which is a special case of the Gamma distribution, whose shape parameter is a positive integer. Additionally, in the special case of the time-scaled inhomogeneous Poisson process, the rate parameter is 1.

The Poisson property of the photon arrival process can be used to study the influence of the statistical nature of arrival times on the timing resolution of the measurement. Most interesting in this context is the dependence of the measurement threshold – i.e. the number of the photon, which triggers the timing stamp digitization – on the resolution. For the scintillation, the time-dependent rate of arriving photons is $\lambda(t) = \frac{N}{\tau} e^{-t/\tau}$, where N is the total number of photons and τ is the decay time constant of the scintillator. Then, $m(t) = N(1 - e^{-t/\tau})$ and the scaled time is $t(u) = m^{-1}(u) = -\tau \ln\left(1 - \frac{u}{N}\right)$, where u is a linear time axis for the standard homogeneous process.

The arrival time distributions for the first photons are plotted in figure 4. It can be seen that it is a necessity to trigger on the first photon to obtain the best possible timing resolution for a given N and τ. Each subsequent photon has a broader arrival time distribution, which is quantified by its larger standard deviation. Furthermore, the timing resolution for the n-th photon is better if there is a larger number of total photons. For a timing resolution of better than 100 ps given $N = 1000$ photons, one has to trigger on the fifth photon or earlier.

2 $\int_0^\infty P_{m(t)}(n-1)dt = \int_0^\infty \frac{m^{n-1}(t)}{(n-1)!} e^{-m(t)} dt = \int_0^\infty \frac{u^{n-1}}{(n-1)!} e^{-u} \frac{du}{du/dt} = \frac{1}{\lambda(t)}$,
where it was used that $\frac{du}{dt} = \lambda(t)$ and $\lambda(t)$ is a constant when integrating over u.

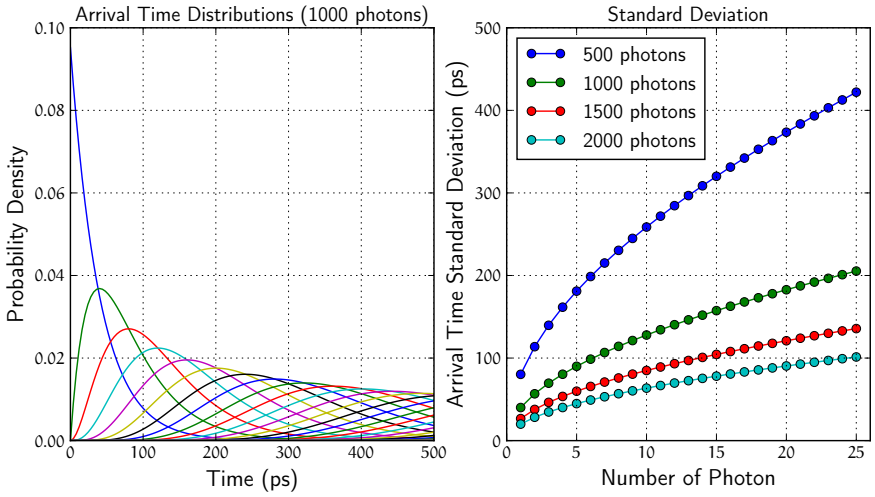

Figure 4: Photon arrival time distribution for $\tau = 40\,\mathrm{ns}$. On the left, the arrival time distributions for the first photons are plotted for a total number of $N = 1000$ photons. The left-most blue curve corresponds to the first photon while the peaks of the distributions correspond to the other photon in increasing order from left to right. The right plot shows the standard deviations of the arrival time distributions as a function of the photon number for different total number of photons N.

2.2.5 *Gamma Detection Probability*

In PET, two gammas are to be detected. The probability of detecting one is equal to the probability of absorbing a gamma

$$P(\text{gamma absorbed}) = 1 - e^{-x/x_0}, \tag{12}$$

where x is the path length and x_0 is the attenuation length. The probability of detecting two gammas is P^2 because both have to be absorbed. The probabilities are plotted in figure 5 for a 511 keV gamma in LSO, for which $x_0 = 1.13\,\mathrm{cm}$ was the taken from figure 2.

From the plot, the influence of the crystal length on the detection probability can be seen: There is an almost linear region up to $2\,\mathrm{cm}$. Using longer crystals in this region has a direct linear impact on the sensitivity while it is rather inefficient to increase the crystal length beyond $3\,\mathrm{cm}$.

2.2.6 *Silicon Photo Multiplier*

The optical scintillation (and Cherenkov) photons are detected using photo detectors. Common choices have been photo multiplier tubes (PMTs) and SiPMs, although the latter has become more popular in the recent past because of their small size, much lower operating voltage, magnetic field compatibility, higher photon detection

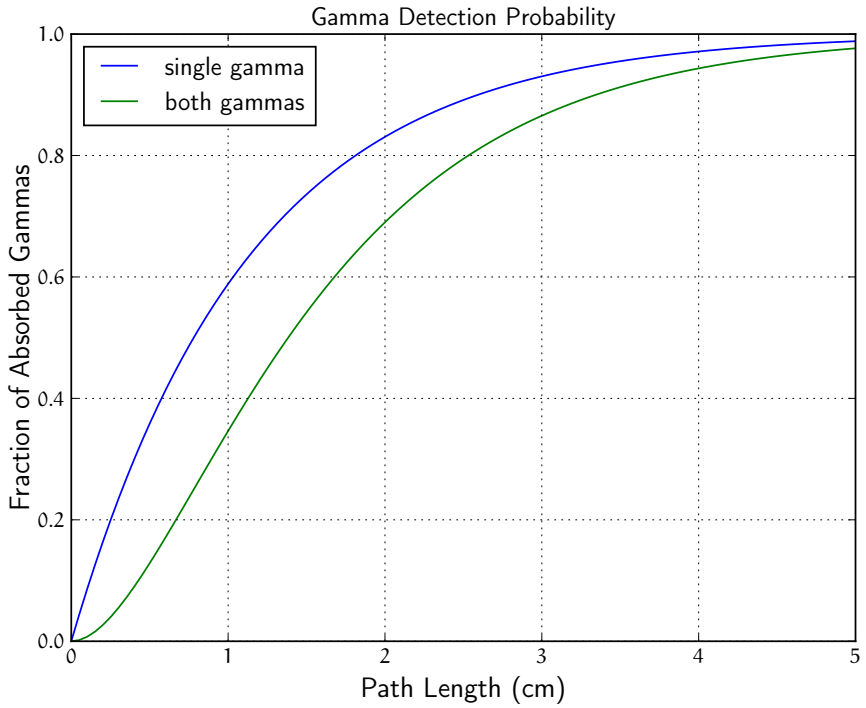

Figure 5: The fraction of gammas and gamma pairs absorbed in LSO is shown. For two gammas, the probability of absorbing one gamma is squared.

efficiency (PDE), mechanical robustness, and insensitivity to light exposure. Therefore and since the SAFIR and BPET detectors are based on SiPMs, I focus on those in this subsection, whose content is based on [19]. The technology of a SiPM was first described in [20, 21] according to [22]. SiPM are also known under different names, e.g. multi pixel photon counter (MPPC) or single photon avalanche diode (SPAD) array, which will become clear in the next paragraphs.

2.2.6.1 *Introduction*

To understand the principle of an SiPM, it is useful to comprehend the functionality of an avalanche photo diode (APD). If a photo diode (technically a pn-junction) is connected to a bias voltage in reverse polarity, a strong electric field builds up in the depletion layer. Incident photons will generate electron-hole pairs with a certain quantum efficiency (QE) through the inner photoelectric effect. The generated carriers begin to drift in opposite directions in the electric field. If the electric field is large enough, the electrons and holes will gain sufficient energy to create secondary electron-hole pairs via ionization. The process will lead to a cascade ("avalanche"), which causes the initial electron-hole pair to be multiplied depending on the applied external bias voltage. This multiplication factor is typically ≈ 50 [23].

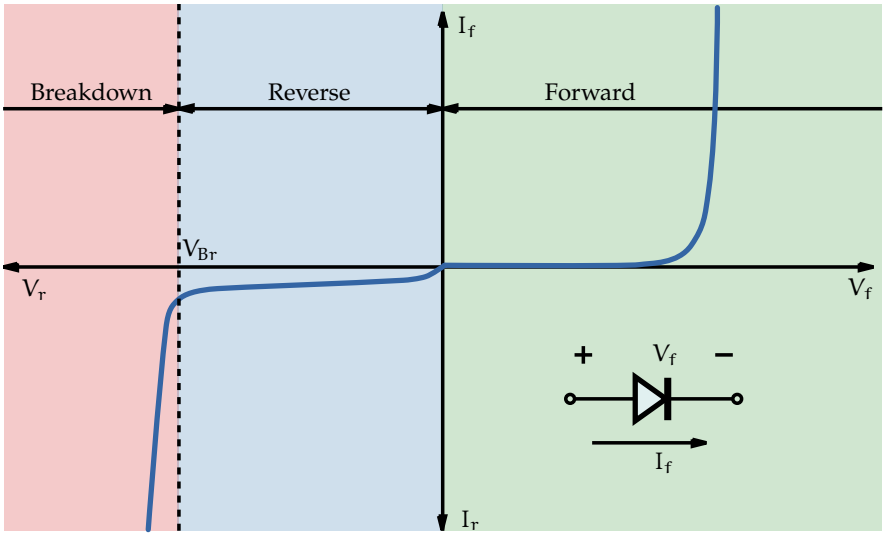

Figure 6: $I - V$ diagram for a general diode. The forward voltage and current are labeled V_f and I_f while the reverse voltage and current are labeled V_r and I_r. The breakdown voltage is the reverse voltage beyond which the magnitude of the current increases exponentially. The corresponding region is the breakdown region, in which SiPMs are operated. Modified from original by H1voltage on Wikimedia Commons released under the CC BY-SA 3.0 license (http://creativecommons.org/licenses/by-sa/3.0).

An APD can be operated in Geiger mode by applying a reverse bias voltage V_{bias} above the breakdown voltage V_{Br}. The breakdown voltage is the voltage, above which the leakage current increases exponentially with the applied reverse voltage, see figure 6. This means that whenever light is incident on the APD, a device specific output pulse is generated, whose charge is independent on the incoming light intensity. This Geiger discharge of the APD has to be stopped in a controlled manner to be able to measure another incoming photon. To achieve this, a quenching resistor (passive quenching, analog SiPM) or a transistor (active quenching, digital SiPM) is used. The following discussion focuses on analog SiPMs.

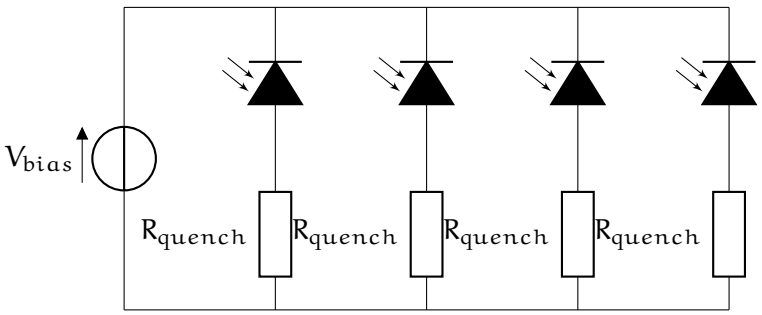

Figure 7: Principle of a parallel circuit of Geiger-mode APDs with quenching resistors.

SIPM	NO. PIXELS	C_P (fF)	GAIN (10^6)
Hamamatsu S13360-3050CS	3600	94	1.76
Ketek PM3350TS-SB0	3600	228	4.27
AdvanSiD ASD-NUV3S-P	5520	90	1.67
SensL MicroFJ-30035-TSV	5676	176	3.30

Table 1: Capacitances and gains for several SiPMs according to the data sheet. The gain can be calculated from these values. The gain has been calculated for $V_{Ov} = 3\,V$.

A parallel circuit of four APDs connected in such a manner is shown in figure 7. The resistor R_{quench} causes the voltage applied to the APD to drop as the Geiger discharge current flows through the resistor. The resulting pulse shape has a fast leading edge resulting from the breakdown and a slower trailing edge originating from the recharge of the capacitance C_{diode} of the diode. The resulting RC circuit of R_{quench} and C_{diode} yields the time constant of the trailing edge.

An analog SiPM is an array of several hundreds or thousands of APD micro-cells (or pixels), each operating in Geiger mode and connected in parallel. This is indicated with four diodes in figure 7. If the cell size is sufficiently small, it is probable that only one scintillation photon hits a cell during a scintillation event. The combined output current of the many parallel APDs is the sum of a number of Geiger discharges, which is proportional to the number of incoming photons.

The overall PDE of a SiPM is proportional to the QE, the geometric fill factor of the device with pixels (active area), and the probability of an avalanche to occur.

2.2.6.2 *Gain*

The gain of a SiPM $M = \frac{Q}{e}$ is the charge Q per avalanche in one pixel divided by the elementary charge. The charge Q is given by the capacitance of each pixel C_P and the overvoltage $V_{Ov} = V_{bias} - V_{Br}$ to be $Q = C_P V_{Ov}$. Values for the gain for different manufacturers are given in table 1. All SiPM in the comparison have a sensitive area of $3 \times 3\,mm^2$, but not necessarily the same pixel size. The effect of the different pixel capacitance on the gain as a function of the overvoltage is plotted in figure 8. A higher capacitance leads to a steeper increase of the gain with higher overvoltage.

2.2.6.3 *Dark Count Rate*

While in the ideal SiPM, the electron-hole pair would only be generated upon the arrival of an incident photon, in a real SiPM there is

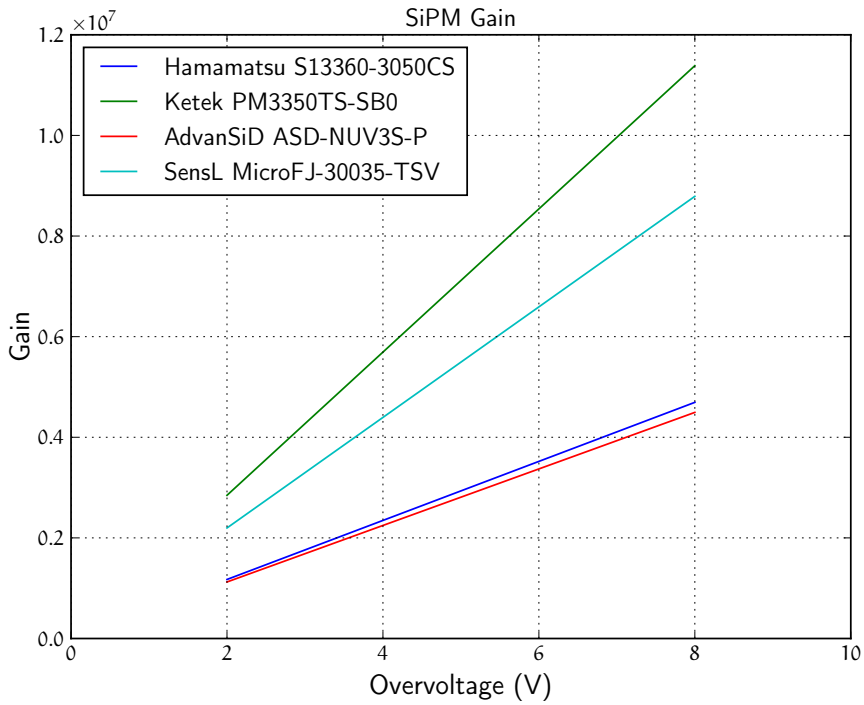

Figure 8: Change of SiPM gain with overvoltage for different manufacturers, i.e. different pixel capacitances.

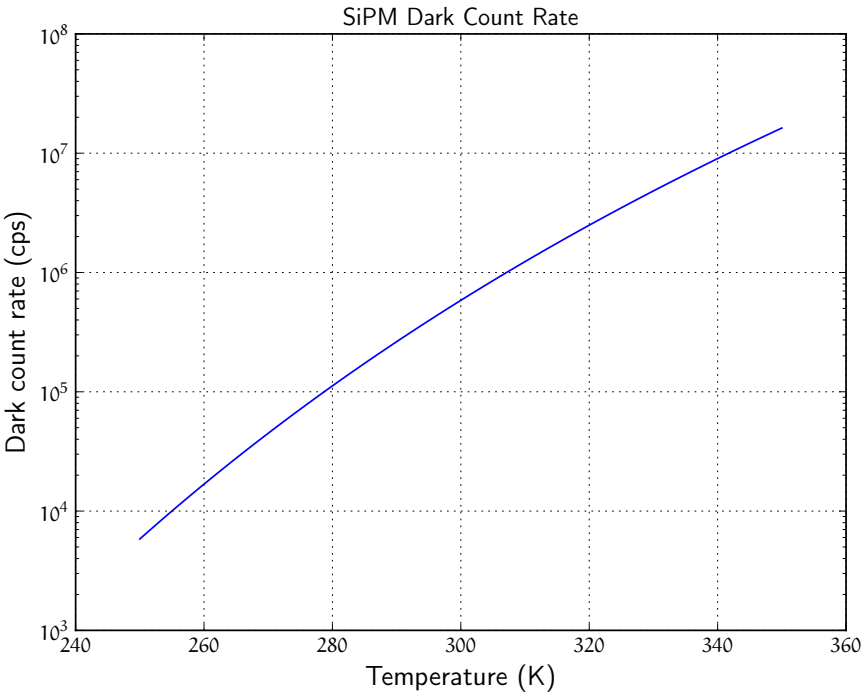

Figure 9: Change of SiPM dark count rate with temperature for silicon with a band gap energy of $E_g = 1.12\,eV$. The rate has been normalized to match the typical rate of the Hamamatsu S13360-3050CS at 298 K and $V_{Ov} = 3\,V$.

SIPM	P_{CT}
Hamamatsu S13360-3050CS	0.03
Ketek PM3350TS-SB0	0.11
AdvanSiD ASD-NUV3S-P	n.a.
SensL MicroFJ-30035-TSV	0.10

Table 2: Crosstalk probabilities for different SiPMs. The probabilities are given for an overvoltage $V_{Ov} = 3\,V$. If the value for this overvoltage was not available from the data sheet, it has been linearly interpolated from the values given. For the AdvanSiD sensor, the crosstalk probability is not given in the data sheet.

a finite probability of thermally creating an electron-hole pair. The output signal of such a thermally created electron-hole pair is indistinguishable from a photon induced signal and is called a dark count. A SiPM at temperature T with band gap energy of E_g will have a dark count rate

$$R_{dark} \propto T^{3/2} \exp\left(-\frac{E_g}{2k_B T}\right), \tag{13}$$

where k_B is the Boltzmann constant. The function is plotted in figure 9. Note that the vertical axis is scaled such that the absolute value of the dark count rate is matched to a specific device.

Although the rate of dark counts is of the order of 10^5 counts per second at room temperature, they are very short. The dark count can influence the timing of the detection when it appears shortly before an actual event. If the expected rate of events is sufficiently low, this is negligible. If that is not the case, the dark count rate can be reduced by cooling the SiPMs to lower temperatures (figure 9).

2.2.6.4 *Crosstalk Probability and Afterpulses*

Even when only a single pixel is fired by an incoming photon (or a dark count), there are cases where pulses equivalent to more than one photon are observed. Depending on the energy of the avalanche electrons, several secondary optical photons are generated, which can travel to neighboring pixels and cause an avalanche there. This happens with a certain probability P_{CT}. The crosstalk probability P_{CT} is not dependent on temperature, but on the overvoltage because a higher overvoltage will cause more secondary optical photons to be generated. Some manufacturers, e.g. Hamamatsu, have introduced trenches between the pixels to reduce the crosstalk probability to a few per cent. Typical values for crosstalk probabilities of different SiPMs are given in table 2.

Some of the carriers generated in the avalanche process can be trapped in lattice defects. When they are released after a certain time, they cause signals indistinguishable from single photon signals. These pulses are called afterpulses.

2.3 SINGLES AND COINCIDENCES

The output pulses of the SiPMs have to be digitized for further processing. Some exemplary output pulse waveforms are shown in figure 10. They were measured with a ^{22}Na source and an Agile LYSO crystal coupled to a Hamamatsu S12572-050C SiPM. The waveforms were digitized using a custom amplifier connected to a Lecroy oscilloscope. SiPM waveforms can be parametrized using the formula

$$f(t) = A \cdot \left(1 - e^{-(t-t_0)/\tau_1}\right) \cdot e^{-(t-t_0)/\tau_2}, \tag{14}$$

where τ_1, τ_2 are time constants, t_0 is an offset to compensate for the time walk, and A is the pulse amplitude. Due to the limited readout bandwidth, only the necessary information should be saved. In PET, two informations about the pulse are relevant: the time and the energy. While the first is needed to find detected gammas in coincidence, the second allows for the selection of events within a certain energy window, e.g. to distuinguish scattered gammas from gammas with energies on the photo-peak. More details on how to measure these two quantities are given in section 4.1.3. The detection of a gamma is called a single event or single. Time, energy, and channel number are recoreded for further processing in the system.

All singles, potentially after passing an energy window requirement, are used to form coincidences. Several techniques and policies exist to define a coincidence. Common among those is the opening of a coincidence window of a defined length triggered by an event. The set of all singles falling into the same coincidence window is called a coincidence event or simply coincidence. Two strategies exist on how to open the coincidence window on the singles, which are sorted according to their times: In the first (single-window sorter), a window can only be opened after the previous window is closed. The other strategy (multi-window sorter) opens a window with every incoming single regardless of whether another window is still open. A found coincidence might have more than two singles. To allow further processing towards image reconstruction, the set of these coincidences has to be reduced to coincidences, which only contain two singles. A short study on how different policies to do so influence the PET scanner's sensitivity is included in 3.4. Once the coincidences have been reduced using a suitable policy, reconstruction algorithms can be employed to obtain an image of the original tracer distribution within the organism.

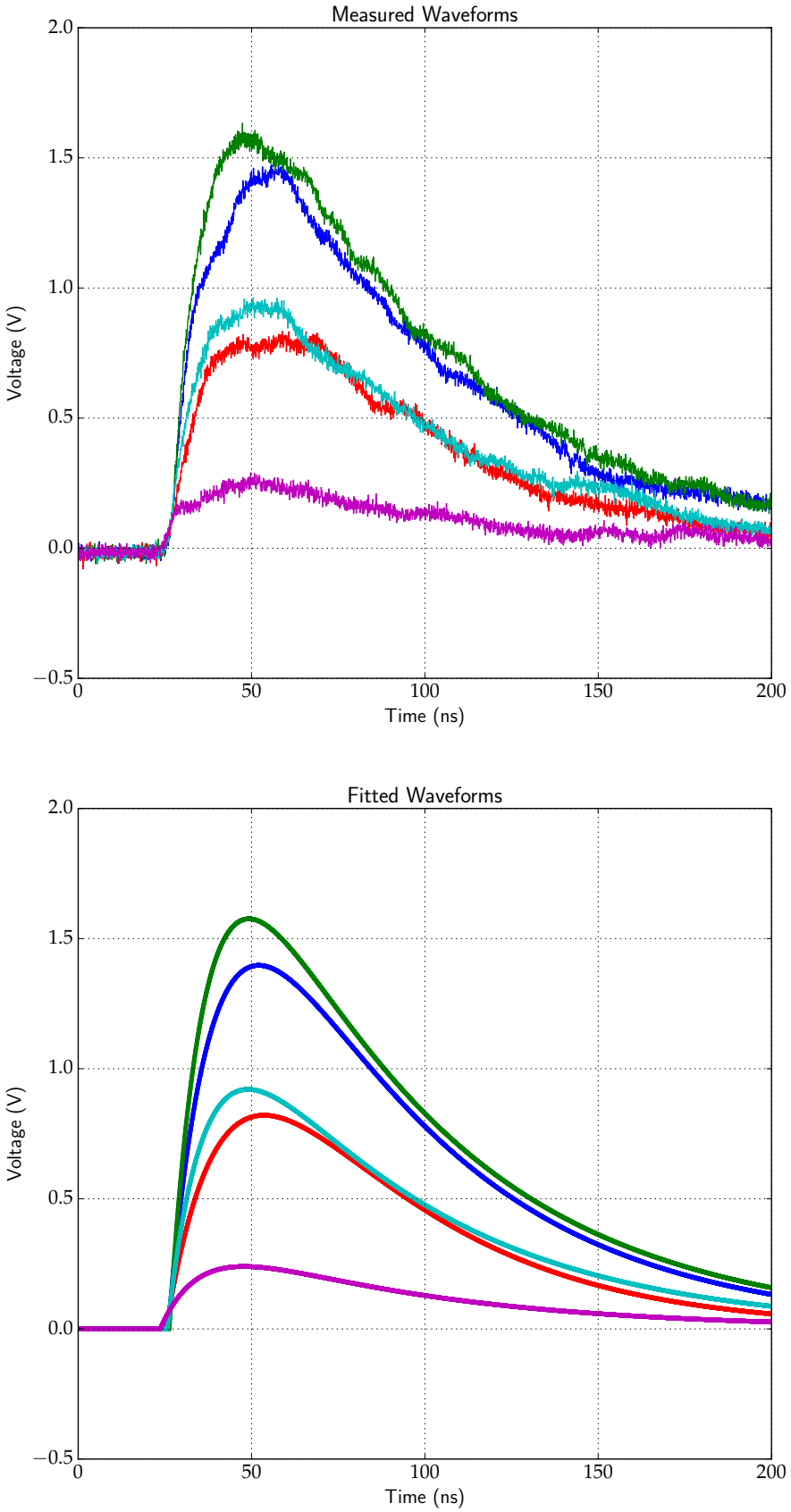

Figure 10: A selection of exemplary waveforms. In the top view, the waveforms as they were measured are shown while in the bottom view, the fitted functions are shown. Different colors represent different pulse heights, which correspond to different measured energies.

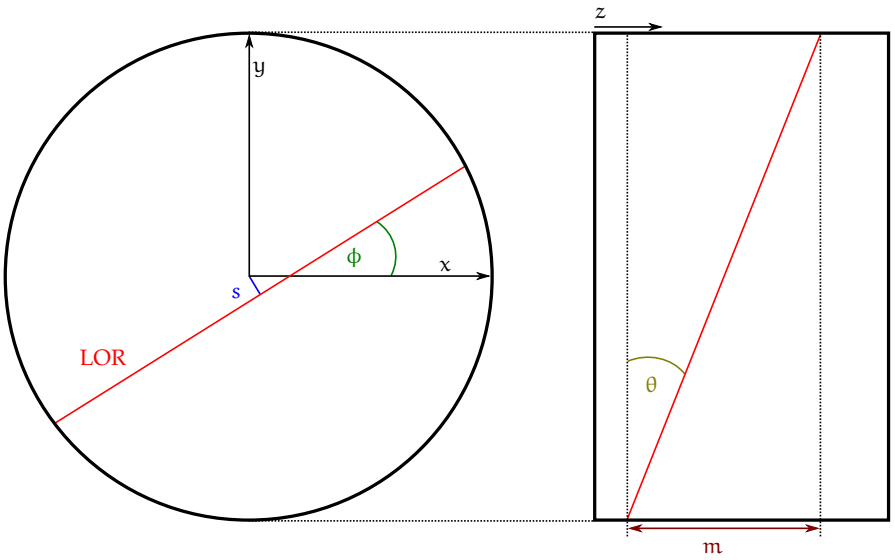

Figure 11: The four coordinate axes s, ϕ, m, θ of the sinogram space are shown in the transaxial plane (left) and a plane containing the z axis (right).

2.4 LIST-MODE AND SINOGRAM REPRESENTATION

The coincidence data is commonly represented in two ways: list-mode and as sinograms. The first is a continuous stream of coincidence events, each identifying two detection elements that have recorded a gamma. The advantage is that the time order of coincidences is preserved, which might be used in the reconstruction. However, the size of the data file scales linearly with the number of events and can become very large for high rates and long acquisitions times.

In a sinogram representation of the coincidence data, every LOR is parametrized as shown in figure 11. The first two coordinates are determined from the LOR's projection on the plane perpendicular to the axial coordinate (z). In this projection, the distance to the origin s and the angle ϕ with a fixed axis, e.g. the x axis, are determined. A two-dimensional histogram with s and ϕ as axes is called a sinogram. The name comes from the fact that the coincidence data originating from a point source looks like a sine in sinogram representation.

The third coordinate m labels the axial position of a sinogram. The fourth coordinate corresponds to the angle θ of the LOR with the z axis. If $\theta \neq \frac{\pi}{2}$, the z position of the middle of the LOR is used for m. The size of a sinogram data file is always the same, no matter how many counts are included. Sinograms containing LORs which are not perpendicular to the z axis are called oblique, the others are called direct. There are algorithms to re-assign counts from oblique sinograms to direct planes, e.g. single slice re-binning (SSRB) [24] and Fourier re-binning (FORE) [25], for further analysis or to allow sim-

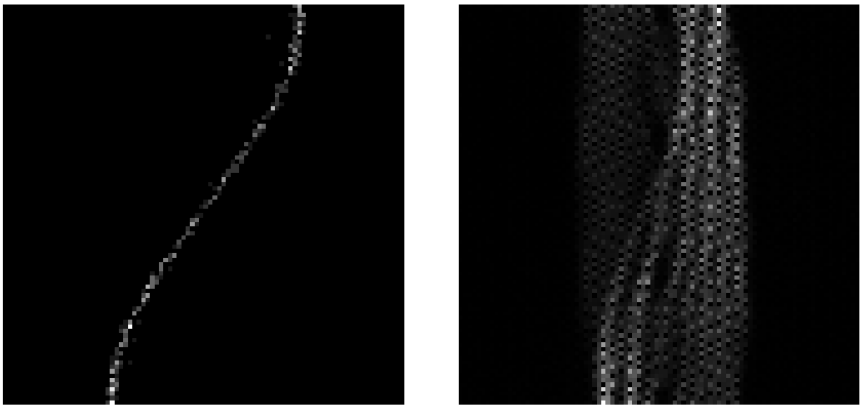

(a) Point source (b) Derenzo phantom

Figure 12: Two example sinograms are shown: a sinogram of a point source on the left and a sinogram of a Derenzo phantom on the right. SSRB was applied and the central slice taken to generate the image.

ple and fast two-dimensional algorithms to be used for tomographic image reconstruction.

Example sinograms from a point source and a Derenzo phantom [26] are shown in figure 12. SSRB was applied and the central slice selected. It can be seen that the sinogram of the Derenzo phantom is a superposition of sines.

2.5 TOMOGRAPHIC IMAGE RECONSTRUCTION

2.5.1 *Mathematical Background*

Previously, the symbol λ was used for the average rate in the generic description of the Poisson process. In the context of image reconstruction here and in later chapters, I will use it differently for the number of counts in a LOR. The measurement of coincidences on a certain LOR is a projection measurement. The number of coincidence counts y_γ on a certain LOR S is in a first order approximation proportional to the line integral of the activity distribution λ along that LOR S:

$$y_S = \int_\gamma \lambda dl. \tag{15}$$

If the space is discretized into J voxels, where the activity in the j-th voxel is given by λ_j, the integral can be expressed as a sum

$$y_i = \sum_j P_{ij}\lambda_j. \tag{16}$$

If there are I LORs, the matrix $P \in \mathbb{R}^{I \times J}$ is called the system matrix, whose elements P_{ij} express the probability of registering a count originating from the j-th voxel in the i-th LOR. Besides the geometric part P_{geom} relating the voxel vector space $\mathbb{R}^J$ to the LOR vector space $\mathbb{R}^I$, the system matrix can account for corrections. These can either be applied in voxel space, which is equivalent to multiplying a matrix $M \in \mathbb{R}^{J \times J}$ from the right with geometric part P_{geom}. Or they can be applied in LOR space, which is equivalent to multiplying a matrix $N \in \mathbb{R}^{I \times I}$ from the left with P_{geom}.

The goal of image reconstruction is to find the vector $\lambda \in \mathbb{R}^J$ given the projection measurement $y \in \mathbb{R}^I$. This is an inverse problem. In the case, where the system matrix P consists only of the geometric part, an analytic algorithm can be found, which is called filtered back projection (FBP). For a more accurate model, involving several corrections in the system matrix, iterative methods are employed – maximum likelihood expectation maximization (MLEM) in the simplest case.

2.5.2 *Filtered Back Projection*

FBP is a reconstruction technique based on the Radon transform [27]. A derivation of the FBP algorithm can be found in appendix A.1, which is like this section based on [28] with slight modification for the application to PET. It should be mentioned that the reconstruction problem is an ill-posed problem. A widely accepted definition of an ill-posed problem given by Jacques Hadamard [29] is that it is a problem which is not well-posed, i.e. one of the three conditions existence, uniqueness, and continuity of the solution with respect to the input data is not fulfilled. If the last condition is violated, small changes of the input data might have tremendous impact on the numerical result. It follows that filtering is required to obtain a stable result.

The Radon transform $\mathcal{R}$ of a function $\lambda : \mathbb{R}^2 \to \mathbb{R}$ with compact support on the unit disc $\{x \in \mathbb{R}^2 : |x| \leqslant 1\}$[3] is defined as

$$(\mathcal{R}\lambda)(s, \phi) = \int \lambda(s\omega + t\omega^{\perp}) dt \tag{17}$$

$$= \int \lambda(s\cos\phi - t\sin\phi, s\sin\phi + t\cos\phi) dt, \tag{18}$$

where $\omega := \omega(\phi) = (\cos\phi, \sin\phi)^T$ and $\omega^{\perp}(\phi) = (-\sin\phi, \cos\phi)^T$ are orthogonal unit vectors. It maps the variables s and ϕ describing the position of a line to the integral along that line, which can be interpreted as LOR.

The FBP algorithm for a unit disc, i.e. with a normalized diameter of 1, is formulated as follows:

3 All functions to be transformed represent objects with finite extent, which justifies this assumption. The boundary of the unit disc is the unit circle, whose elements (the unit vectors) are interpreted as directions.

1. Define
   - p: bandwidth of the measurement, e.g. number of directions,
   - h: sampling distance with $h \leqslant \frac{\pi}{p}$ to satisfy the Nyquist-Shannon sampling theorem [30, 31],
   - $q = \frac{1}{h} \approx \frac{p}{\pi}$,
   - $l = -q, \ldots, q$,
   - $s_l = lh$,
   - $e_\gamma(s_l)$: discretized convolution filter, e.g. Shepp-Logan filter $e_\gamma(s_l) = \frac{\gamma^2}{\pi^4} \frac{1}{1-4l^2}$.
2. For all $j = 1, \ldots, p$ calculate the convolution of the filter with the measurements
$$\Psi_{j,k} = h \sum_{l=-q}^{q} e_\gamma(s_k - s_l) \mathcal{R}\lambda(s_l, \omega_j), \; k = -q, \ldots, q. \tag{19}$$
3. For every coordinate $x \in \mathbb{R}^2$ calculate the discrete back projection
$$\tilde{\lambda}(x) = \frac{2\pi}{p} \sum_{j=1}^{p} ((1-\eta)\Psi_{j,k} + \eta\Psi_{j,k+1}), \tag{20}$$
where k, η are such that $s = \langle x, \omega_j \rangle$, $k \leqslant \frac{s}{h} < k+1$, $\eta = \frac{s}{h} - k$ is fulfilled.

This is the reconstructed tracer density $\tilde{\lambda}$. The presented algorithm is limited to two-dimensional geometries. However, three-dimensional versions have been developed, see for example [32]. The second step contains a linear interpolation between sampling points. Although FBP is still in use for certain applications, i.e. comparable spatial resolution results according to the National Electrical Manufacturers Association (NEMA) standard (cf. 3.6.2) or certain quantitative PET analyses, iterative reconstruction methods are often employed due to their superior image quality results.

2.5.3 *Iterative Algorithms – Maximum Likelihood Expectation Maximization*

Another approach to reconstruct an approximation of the original tracer distribution $\vec{\lambda}$ is based on the maximum likelihood estimation of parameters and was first proposed by Shepp and Vardi [33]. The detection process can be modelled as a Poisson process[4]. The coincidence measurement yields a vector of counts $\vec{y} = (y_1, \ldots, y_I)^T$ per

4 A modified version of this section has become part of [34].

LOR i. The reconstruction can be used to obtain an estimation of these counts $\vec{\bar{y}}(\vec{\lambda}) = (\bar{y}_1(\vec{\lambda}), \ldots, \bar{y}_I(\vec{\lambda}))^T$ from the reconstructed image.

The likelihood function of the Poisson process – namely the probability of detecting $\vec{y}$ when the reconstructed image estimates $\vec{\bar{y}}$ – can be written as

$$L(\vec{\lambda}) := p(\vec{y}|\vec{\bar{y}}) = \prod_{i=1}^{I} p(y_i|\bar{y}_i) = \prod_{i=1}^{I} e^{-\bar{y}_i} \frac{\bar{y}_i^{y_i}}{y_i!}, \tag{21}$$

$$\log L(\vec{\lambda}) = \sum_{i=1}^{I} \left[y_i \log \bar{y}_i - \bar{y}_i - \log y_i! \right], \tag{22}$$

where y_i is the actually measured number of counts in the i-th line-of-response (LOR). Finding the maximum of the likelihood function with respect to $\vec{\lambda}$

$$\frac{\partial(\log L(\vec{\lambda}))}{\partial \lambda_j} = \sum_{i=1}^{I} \left[\frac{y_i}{\bar{y}_i} - 1 \right] \frac{\partial \bar{y}_i}{\partial \lambda_j} = 0 \tag{23}$$

can be done using the expectation maximization (EM) algorithm [33] to obtain an iterative formula

$$\lambda_j^{k+1} = \frac{\lambda_j^k}{\sum_{i=1}^{I} a_{ij}} \sum_{i=1}^{I} a_{ij} \frac{y_i}{\bar{y}_i^k}, \tag{24}$$

$$\bar{y}_i^k := \sum_{j=1}^{J} a_{ij} \lambda_j^k + n_i, \tag{25}$$

where n_i is a noise term. See appendix A.2 for further details. The partial derivative $\frac{\partial \bar{y}_i}{\partial \lambda_j}$ yields the projection matrix element a_{ij} due to the linear model (16). Note that the iterative formula can be written in the form of a gradient ascent method

$$\lambda_j^{k+1} = \lambda_j^k + \frac{\lambda_j^k}{\sum_{i=1}^{I} a_{ij}} \frac{\partial(\log L)}{\partial \lambda_j}. \tag{26}$$

This algorithm can be written in another form to allow processing of the data event by event (list-mode):

$$\lambda_j^{k+1} = \frac{\lambda_j^k}{\sum_{i=1}^{I} a_{ij}} \sum_{l=1}^{L} \sum_{i=1}^{I} \delta_{i,c(l)} \frac{a_{ij}}{\bar{y}_i^k} = \frac{\lambda_j^k}{\sum_{i=1}^{I} a_{ij}} \sum_{l=1}^{L} \frac{a_{c(l),j}}{\bar{y}_{c(l)}^k}, \tag{27}$$

$c(l)$:=index of detector pair
corresponding to l-th list-mode event,

where L is the number of list-mode events and δ_{ij} is the Kronecker delta. It is worth noting that

$$\sum_{l=1}^{L} \delta_{i,c(l)} = y_i \tag{28}$$

because the Kronecker delta evaluates to 1 in exactly y_i cases and otherwise to 0.

The operation in equation (25) is called forward projection because it projects the activity distribution onto the LORs. In equation (27) it implicitly reappears in the denominator of the last term. The back projection is represented by the sum over l in (27) because by this operation, the LOR count data is mapped to the activity distribution.

FBP will be used later to evaluate the spatial resolution of the simulated data for the SAFIR and BPET geometries in 3.6.2. An extension of the MLEM algorithm is used to reconstruct a Derenzo image quality phantom [26] in 3.6.4.

2.6 THE SMALL ANIMAL FAST INSERT FOR MRI

The SAFIR project aims at the development of a high-rate capable PET insert. The image quality and in particular the signal-to-noise ratio in PET images is highly dependent on the number of registered counts, due to the Poisson nature of the underlying process. If a given number of counts were registered within a shorter time, the acquisition time frames could be shortened accordingly, thus allowing for a higher temporal resolution of tracer dynamics.

While the sensitivity of PET devices has been optimized and cannot be improved by large factors due to the available scintillators[5], photo-sensitive devices[6], and fundamental physics[7], the upper limit of injected activity has not yet been reached. If the activity in a mouse is a factor of 10 higher than common activities (50 MBq) while maintaining the detection capability for the coincidences, time frame durations can be reduced by the same factor. To achive this, SAFIR will have an excellent timing resolution of the order of a few hundred picoseconds. Using an equivalently short coincidence time window (CTW), the contribution of random coincidences to the total count rate can be held low. This is unprecedented in preclinical PET. For the first time it will be possible to resolve oxygen uptake curves in the rodent brain non-invasively and spatially resolved. Thus far, this has only been measured using beta-probes, e.g. in [1].

5 For instance, a scintillating material with high light yield and excellent photo-effect cross-section is desirable for this purpose.

6 Devices with a higher light detection efficiency.

7 A smaller electron mass would increase the probability of photo effect versus Compton scattering in the scintillator.

2.7 BPET – COST-EFFECTIVE BRAIN PET

AD and other neuro-degenerative diseases are becoming more and more important in our modern aging societies.[8] Until recently, no lasting improvement or preventive treatment of AD was available. Even with such a treatment, early, i.e. pre-symptomatic, diagnosis is currently unfeasible due to the high costs in both infrastructure and operation of the only known reliable detection technique: PET [2, 3]. Current research suggests that the aggregation of neuro-toxic Abeta plaques in the human cortex are the cause of the dementia associated with AD [4]. PET tracers such as ^{11}C-Pittsburgh compound B (PiB) or ^{18}F-Florbetapir bind to Abeta molecules enabling the spatially resolved visualization of their concentration in the brain [35]. With recent promising developments towards a preventive treatment such as the human antibody Aducanumab [5], the need for a cost-effective pre-symptomatic diagnosis method has become even more urgent.

The development towards a complete prototype of a brain PET scanner for diagnosing early AD has started, which we call BPET. The targeted price of such a device (<200'000 CHF) is more than ten times smaller than for current devices, making it affordable in large quantities for hospitals. With this device, large screening centers with 10 to 20 of such machines become possible for the first time. The cumulated installation of such a number of machines has another advantage: the decaying PET tracer can be used in parallel reducing the cost per patient almost inversely proportional to the number of machines.

The goal of this order of magnitude in price reduction can be achieved exploiting the fact that Abeta accumulation is a global phenomenon in the cortex making it unnecessary to have a fine local resolution. By reducing spatial resolution and sensitivity, savings in crystal material volume, photo-sensor area, and the complexity of the readout electronics can be realized to make this cost-effective approach possible. Simulation studies of the foreseen BPET scanner will be presented and discussed in section 3.6

8 This section has in similar form appeared in Bridge proposal 20B1-1_173854 to the SNF.

Part II

THE DEVELOPMENT

3

MONTE-CARLO SIMULATION BASED DETECTOR EVALUATION

In this chapter, performance characteristics of variations of a reference geometry as well as lab test results of selected components are presented. At first, the geometric concepts of the SAFIR and BPET scanners are described. It follows an introduction to my custom developed coincidence sorting framework as well as to my contribution to the Software for Tomographic Image Reconstruction (STIR) library, which is used for the processing of the projected data, for image reconstruction, and partially for image analysis. These tools were used to obtain the subsequently presented analysis of standardized measures of sensitivity, spatial resolution, and noise equivalent count rate (NECR). In addition, the reconstruction of a Derenzo phantom to evaluate the spatial resolution in a more realistic scenario is presented.

3.1 THE SAFIR GEOMETRIC CONCEPT

The proposed SAFIR scanner is designed to have radially oriented crystals arranged on a cylindrical shell, which is a widely used geometry concept for PET devices. To allow referring to a well-defined and complete geometry specification, a reference design has been established, which was first described in a contribution of the author on behalf of the SAFIR collaboration in [36]. It comprises crystal matrices with 8×8 LSO-like crystals, each of dimension $2.1\,\mathrm{mm} \times 2.1\,\mathrm{mm} \times 12.0\,\mathrm{mm}$ and individually wrapped in 3M enhanced specular reflector (ESR) foil. The crystals are one-to-one coupled to Hamamatsu SiPM arrays to form a module. Twenty-four such modules are arranged to form a regular icositetragon with an apothem of $68.75\,\mathrm{mm}$. Ten such rings are axially arranged with a $0.2\,\mathrm{mm}$ gap between them to form the whole scanner with a total axial extent of $178.6\,\mathrm{mm}$.

The entire scanner is divided into three compartments: two electronic compartments at each end and a central sensor compartment. Kapton cables transmit the analog SiPM signals from the sensors in the central compartment to the electronic compartments, where they are digitized and send to the data acquisition system (DAQ) system via an optical link. The electronic compartment furthermore hosts power conversion and clock distribution circuitry. A rendering of this system is shown in figure 13. All sensors and electronics are embedded into a mechanical structure consisting of two cylindrical shells made from glass or carbon fiber and covered with copper strips for shielding. The shells are connected via flanges on either end. The inner

shell holds mounting structures for the printed circuit boards (PCBs) and the sensors.

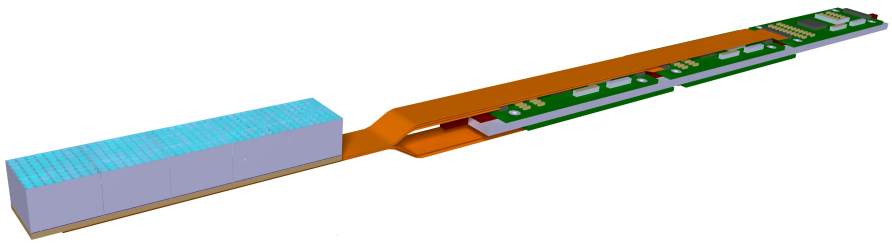

(a) One sector of the reference design with capton cables for the analog signal transmission.

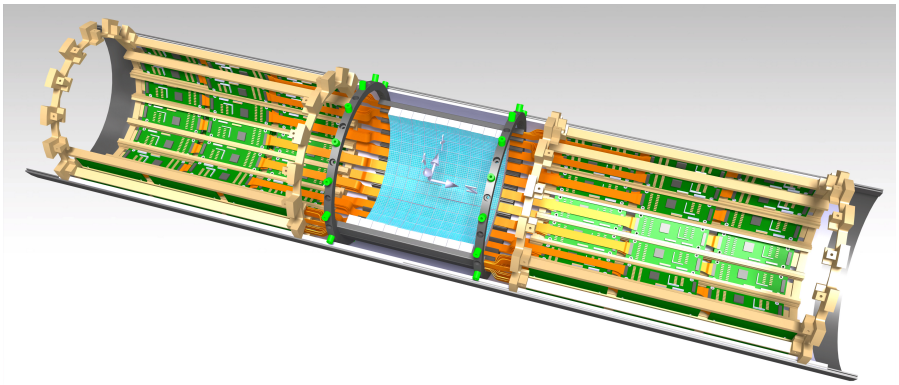

(b) Integration of a half scanner of the reference design geometry into the mechanical structure.

Figure 13: Renderings of the reference design geometry.

This reference design is used as parent design towards several designs taking into account mechanical, electronics, or other constraints. Most notably, two prototypes are developed and built. The mechanical drawings for the crystal arrangements in the prototypes are included in appendix B.1.

One of the prototype designs features the SiPM Timing Chip (STiC) [37] as front-end ASIC and is closest to the reference design geometry. Two sectors each have been combined forming in total 12 sectors for a full scanner. On each axial side of a sector, 5×2 of the previously described modules are connected to a PCB, which acts as a signal transmission line for the 640 analog signals of the individual SiPMs. It is called SAFIR analog signal (SAS) plane. Its other end is connected to the small SAFIR STiC (SST) board hosting the STiCs, which digitize the analog signals. For the prototype, only one STiC is mounted due to its current packaging size. The digital output and the control interface of the SST are connected to the SAFIR digital interface STiC (SDIS) board hosting an FPGA, power conversion, clock distribution circuitry, and

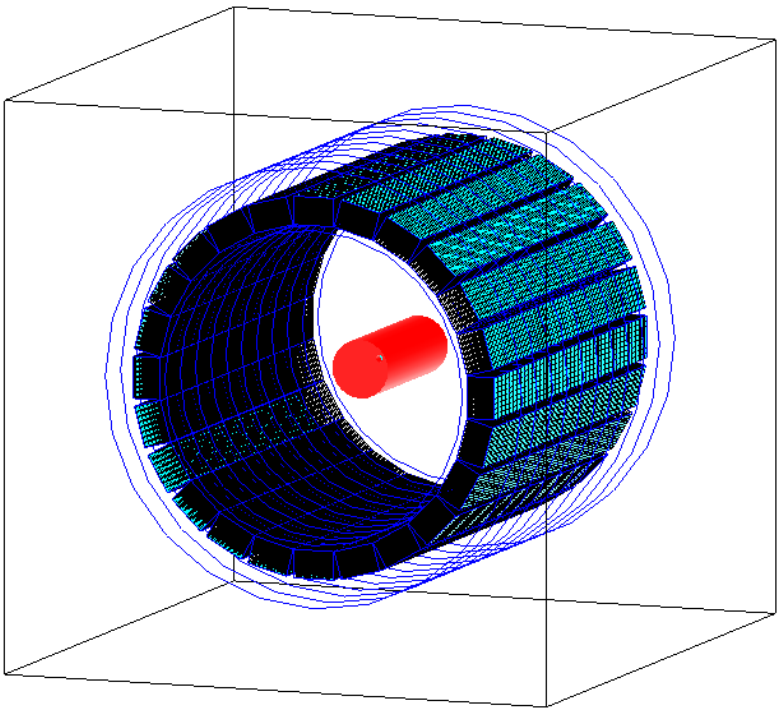

Figure 14: Output of the visualization of the Geant4 simulation of the SAFIR reference design with a NEMA mouse phantom in the center.

an optical link. It is connected to the DAQ system for power and data transmission.

The other prototype design features the SUBLIMA PET module [38], a ceramic hybrid hosting 4 PETAs [39] on one side and 12×12 SiPMs with a size of $2.25\,\mathrm{mm} \times 2.25\,\mathrm{mm}$ each on the other side (cf. also figure 47). The pitch between SiPMs is 2.5 mm. The crystals have the same front surface as the SiPMs and are by default 10 mm long. It is possible to mount longer crystals. The separator between individual crystals consists of three layers: ESR, Aluminum, ESR. The current arrangement on the module and its size constitute constraints on the integration into a geometry similar to the reference design. For the prototype, the same mechanical structure is used as for the STiC version. However, the SUBLIMA modules take the place of the SiPM modules. The purely digital signals are connected to the SAFIR digital interface PETA (SDIP) board, a longer version of the SAS providing the functionality of the SDIS. The equivalents of the SAS and the SST are not needed because the front-end ASIC is already integrated onto the SUBLIMA module. From the drawings in appendix B.1 it can be seen that there are large gaps between sectors, which can only be avoided when the numbers of sectors is increased to 14. The effect on the sensitivity of a scanner with such configurations was simulated and will be presented later in this chapter.

For both prototypes, the outer side of the SAS respectively the SDIP is connected to the SAFIR bias and temperature (SBT) board, which provides the bias voltages to the SiPMs with mV accuracy and reads out temperature sensors located close to the photo-sensors to adjust the bias voltage accordingly in order to keep the gain stable.

3.2 THE BPET GEOMETRIC CONCEPT

BPET differs from SAFIR in many ways. Not only is it targeted at scanning human brains contrary to whole mice. Furthermore its driving design principle is to be specific and cost-effective. Large cost factors in building a PET scanner are the material budgets for photo-sensors and scintillating crystals, with a ratio between them of about 1:2. Reducing the crystal volume as well as the area of the photo-sensor is thus an effective way to cut costs on a general PET scanner. This will directly translate into a reduced sensitivity and a reduced spatial resolution. For a specific use case – here the efficient early diagnosis of AD –, a lower performing device can still be sufficient with respect to that case. The accumulation of Abeta in the human cortex indicating a need for treatment is a global phenomenon in this brain region. Thus it is admissible to compromise the spatial resolution for the benefit of a reduced budget.

Figure 15 shows axial images of an Abeta negative (top row) and an Abeta positive (bottom row) patient taken with a conventional PET scanner. On the left, the original images are shown. The middle and right columns contain the same images smeared to 10 mm and 16 mm resolution, respectively. It can be seen that even the worst degradation still allows a clear distinction between the positive and the negative case. As a consequence for the BPET design, a resolution of at least or better than 10 mm full width at half maximum (FWHM) is the set goal to allow for a margin. In addition, at lower resolution, the voxel size is bigger. Increasing the edge length on all sides by a factor two results in an eight times larger volume containing equally more counts. Taking into account the possiblity of slightly longer scan times, the sensitivity can be reduced by an order of magnitude. This sets the sensitivity goal at approximately 1 cps/kBq. On the whole, this leads to a geometric concept as follows.

Using crystals of $8\,mm \times 8\,mm \times 10\,mm$ size one-to-one coupled to SiPMs with $3\,mm \times 3\,mm$ sensitive area, modules with 15×12 crystals are constucted. The pitch between crystals is 8.6 mm in both directions. Eight modules are arranged to form an octagon with an apothem of 158.57 mm. This arrangement contains 1440 crystals and has an axial coverage of 102.6 mm – just enough to cover roughly the relevant region of the human brain.

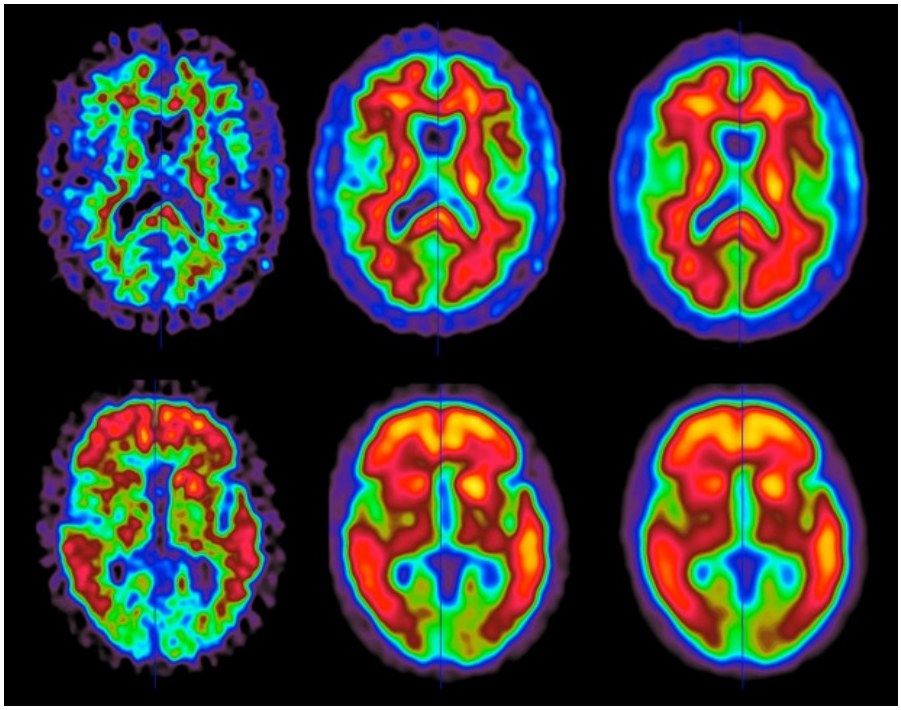

Figure 15: Axial images of two brain scans with a conventional PET scanner. The top row shows an Abeta negative patient while the bottom row shows an Abeta positive patient. The left column depicts the original scan and the middle and right columns show the same images reduced to 10 mm and 16 mm resolution, respectively. Images courtesy of Prof. A. Buck, Univerity Hospital Zurich.

3.3 SIMULATIONS

Monte Carlo (MC) simulations play an important role for studying the expected detector performance for different geometries and processing toolchains. Within the SAFIR collaboration, two simulations programs are in use: a standalone simulation application based on Geant4 [40–42] developed specifically for the needs of the collaboration as well as the Geant4 application for emission tomography (GATE) [43, 44], which can be used with macros defining the scanner geometry, the sources, and the phantoms. While the first needs C++ programming for most parameters but is faster because of its true multi-threading capability, the latter is easier to use through its macro language but does not achieve the performance of the first. Unfortunately, it is not easily possible to compare outputs of the two frameworks. Differences originating likely from the physics process model as well as the simulated digitization chain are present in the data and can not easily be resolved. Therefore, results should only be compared within the data generated within one framework.

The SAFIR reference design has been simulated with the standalone application to obtain performance measures such as NECR, sensitivity, spatial resolution, and a Derenzo phantom image, GATE was used to compare different SAFIR prototype geometries as well as estimating the BPET performance with respect to sensitivity and spatial resolution. The results are presented in section 3.6.

3.4 COINCIDENCE SORTING

In a PET measurement, the direction is determined from the fact that the two back-to-back gammas from the annihilation are measured. The line joining the two detection positions is used as the line along which the annihilation took place. The PET detector, however, measures only single events ("singles"), which have to be grouped into coincidences for further processing. A single is the sum of all energy depositions in the same crystal during an annihilation event. Consequently, an annihilation event can lead to several singles recorded in the data.

It is assumed that the singles have been sorted with respect to time. Single events have now to be assigned to groups, which are called coincidence events. The procedure is visualized in figure 16. At first, it has to be decided which singles open a coincidence window. Two common strategies exist, namely opening a window at every single after the previous window is closed (single window) or opening a window at every hit regardless of whether any windows are still open (multiple window).

It is obvious that the windows opened in a multiple window approach contain the windows that had been opened in a single window

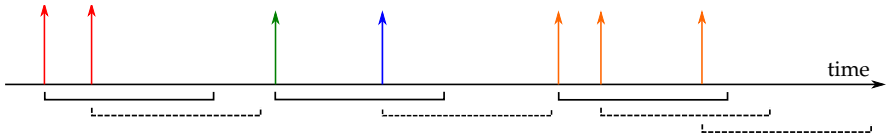

Figure 16: Sketch of the coincidence sorting process. The singles coming from the same annihilation are depicted in the same color. The coincidence window is represented by a bracket underneath the time axis. If a multiple window approach is used, the dashed brackets constitute coincidence events in addition to the solid ones. Three cases are shown: the first (red) event is a true coincidence with exactly two singles. This is often called a "golden" event. The middle case is a random event with two singles: the single events originate from different annihilations, which cannot be distinguished in real data. The last case is a triple coincidence, where one of the gammas has presumably scattered in the phantom or the crystal generating a third single hit. Note that such a triple event can also contain a random single.

sorting. The additional windows in a multiple window sorter are illustrated as dashed lines in the figure. For the following analyses, a multiple window approach is used. This is advantageous because no window opening opportunity is missed. On the other hand, care has to be taken that no coincidences are reported twice. The set of singles falling into the same coincidence window is called a coincidence event. If a coincidence event contains only singles originating from the same annihilation, it is called a true coincidence, otherwise a random coincidence.

The length of the CTW is constrained by two values: the gamma travel time difference and the coincidence resolving time (CRT). While the first stems from the fact that the point of annilation can be closer to one detector than to the other, the second part originates from the finite timing resolution of the detector. Both pose a lower limit on the length of the CTW. On the other hand, the CTW should be as short as possible to limit the contribution of random coincidences to the total count rate because the total rate of random coincidences increases with the square of the singles rate [45].

3.4.1 *Selection Procedures on Raw Coincidences*

A general coincidence event can contain between one and several singles. However, for further processing two singles have to be identified representing the LOR. This demands for an algorithm to reduce the coincidence of a given multiplicity to one with multiplicity two. Critical to the accuracy of PET is that the two selected singles originate from the first interactions of the annihilation gammas with matter. On the other hand, discarding all scattered singles significantly reduces the

system sensitivity because many singles will scatter in the crystal to a neighboring crystal. On the whole, the following should be required:

1. After the selection process, only two singles remain.
2. Singles generated by gammas scattered in the phantom should be discarded.
3. Singles scattered in the crystal should be recovered if the correct first interaction can be identified with reasonable accuracy.

In my implementation of a coincidence sorter, which is part of the analysis tool and online monitor (ATOM), three policies are implemented. The first, which is the most conservative, discards all coincidence events with a multiplicity other than two or with two singles, of which at least one is outside a to be specified energy window. The events surviving these cuts are called "golden" events. The lower boundary of the energy window is needed to reduce the fraction of events, in which one of the gammas scattered in the body or the detector. A typical energy window for preclinical PET is 350 keV to 650 keV and will be used unless otherwise stated for both SAFIR and BPET. The first condition satisfies requirement 1, while the second condition removes most scattered events, regardless of if they occured in the phantom or the crystal. This implies an expected low sensitivity. The second policy applies the energy window to all singles in a coincidence. If afterwards two singles remain, the event is used. The third policy involves a very simple algorithm to recover inter-crystal scattered events. If two singles occured in crystals separated by a configurable maximum number of crystals in either axial or tangential direction, their energies are summed and the coordinates of the first in time are taken. If the multiplicity after grouping is two, the coincidence is accepted. It will be shown later that this procedure significantly increases sensitivity for the SAFIR scanner. At the same time, the resolution might degrade because events might be assigned to the wrong crystal. It is always checked that a coincidence is not occuring twice, which is particularly important for the multiple window sorter with one of the two latter policies.

3.5 RECONSTRUCTION WITH STIR

The STIR [46] is an open source framework to perform PET image reconstruction. It contains various C++ libraries, which can be used in different reconstruction algorithms, as well as executables to use the library functions directly from the command line. In addition, various utilities are available to correct and manipulate PET projection as well as image data.

In its official distribution, STIR natively supports a variety of commercial PET scanner data formats and their corresponding geometries.

Given a custom and not yet finally defined (thus variable) geometry as in the SAFIR project, it was necessary to enable STIR of reading a custom input file format together with the scanner geometry. The author has written such an extension to STIR, which is publicly available for use with STIR [47].

The classes of this extension define a 64-bit coincidence list-mode data format as shown in listings 1 and 2. The type field labels, if the event contains the indices of a crystal pair, which has recorded a coincidence, or a time stamp. This allows the same event stream to contain both without the unnecessary overhead of a timestamp in every event. After coincidence sorting, the precision of milli-seconds is sufficient. The field isRandom in a record can be used to label random coincidences (e.g. from a delayed window coincidence sorter).

Upon construction, the reading class creates a crystal map from a coordinate text file. The map contains physical crystal coordinates for every index triple (ring, detector, layer). A layer index would be used if there was more than one crystal stacked in the radial direction. Events from the events stream are converted to LORAs2Points objects, which can be used in STIR. Currently, STIR can only handle cylindrical scanners, i.e. a structure with modules is not implemented. However, the LOR data can be resampled to a cylindrical scanner. This is visualized in figure 17. The original coincidence event detected in the two yellow crystals corresponding to the green LOR is sorted into the blue (virtual) cylindrical scanner into the bin of the sinogram corresponding to the position of the two red circles.

3.6 PERFORMANCE MEASURES

The NEMA has defined a standard for evaluating preclinical PET scanners such as the one which is subject of this thesis in the standard publication NU 4-2008 [48]. For clinical scanners such as BPET, a similar standard was released and is used accordingly [49]. Based on the measurement procedures outlined therein, a specific PET scanner

Listing 1: Definition of binary list-mode input file format for STIR: coincidence record.

```
unsigned type : 1 ; // type = 0 labels a coincidence
unsigned isRandom : 1;
unsigned reserved : 6;
unsigned layerB : 4;
unsigned layerA : 4;
unsigned detB : 16;
unsigned detA : 16;
unsigned ringB : 8;
unsigned ringA : 8;
```

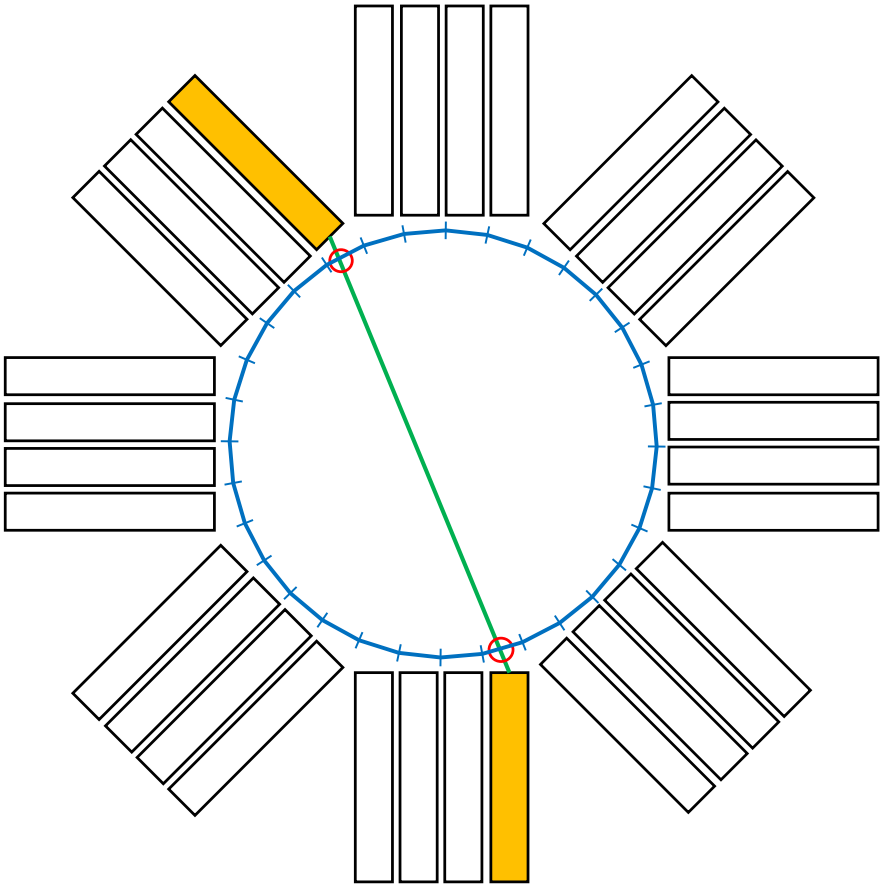

Figure 17: Depiction of a PET scanner with a coincidence event between the two yellow crystals. The actual LOR is marked in green. The cylindrical (virtual) scanner is shown in blue. This event will be sorted into the sinogram bin of the virtual scanner corresponding to the position of the red circles.

can be compared with others for similar applications. Although primarily aimed at physically existing scanners, the procedures can be adapted for application to simulated scanner data. This proves helpful for tuning the scanner design to fulfill the specific needs of the SAFIR application.

In addition to the NEMA measures, other source distributions such as the Derenzo phantom [26] are useful to study the scanner performance for applications closer to a realistic scenario. While NEMA prescribes FBP for the estimation of the spatial resolution for better comparability, the achievable resolution can be greatly enhanced by employing more advanced iterative reconstruction techniques. Although their intrinsic performance is not necessarily better than FBP, they allow a more realistic and accurate modeling of the PET detector. Using those, phantom studies deliver resolutions closer to realistic scenarios.

For the following studies, it is assumed unless otherwise noted that a bias-free random estimation method with negligible statistical variance is available. Thus the Monte Carlo information about the random character of a given coincidence can be used to distinguish between true and random coincidence events. For NECR, spatial resolution, and sensitivity, a Gaussian smearing in time and energy is applied to the singles from the simulated data. Unless otherwise stated, the standard deviations of the used Gaussian distributions for SAFIR are $\sigma_t = 120\,\mathrm{ps}$ on the singles time and $\sigma_E = 8.5\,\%$ on the energy. The singles are then sorted into coincidences using the custom coincidence sorter with a window of 400 ps length and an energy cut of 350 keV to 650 keV. For BPET, the GATE coincidence sorter is used with the standard options and no additional digitization elements and a coincidence window of 5 ns length.

3.6.1 *Noise-Equivalent Count Rate*

Every measurement is subject to statistical fluctuations and uncertainties. To quantify the stochastic nature of the underlying radioactive process in combination with the detection process, it is useful to define a measure of signal to noise (SNR) ratio. The NECR, which was first introduced in 1990 [50], is such a measure, which I will describe in the following. It is the number of true events divided by its stan-

Listing 2: Definition of binary list-mode input file format for STIR: time record.

```
unsigned type : 1; // type = 1 labels a time record
unsigned reserved : 15;
unsigned long time : 48; // in milli-seconds
```

dard deviation. This standard deviation is also the square root of the sum of signal and background.

In PET, there are three contributions to the so called prompt coincidence count rate P, which is the uncorrected rate of counts in the LORs. These coincidence can be either true, random, or scattered. The respective mean rates are called T, R, S, resulting in the formula

$$P = T + R + S \tag{29}$$

for the prompt count rate. All rates follow Poisson statistics and consequently the variance of each value is equal to its mean value. Consider the variance of the true rate T

$$\begin{aligned}(\Delta T)^2 &= (\Delta (P - R - S))^2 && (30)\\ &= (\Delta P)^2 + (\Delta R)^2 + (\Delta S)^2 && (31)\\ &= T + R + S && (32)\end{aligned}$$

where it was used that $\Delta P = \sqrt{P} = \sqrt{T + R + S}$. Furthermore, the variances of the estimation of the random and scattered coincidence rates in equation (31) are neglected because essentially variance-free methods for their estimation exist [45, 50]. Signal-to-noise is the fraction of signal events over the noise. In the case of PET, this is the ratio of the true rate to its standard deviation

$$SNR = \frac{T}{\sqrt{T + R + S}}, \tag{33}$$

whose square is defined to be the noise equivalent count rate

$$NECR = \frac{T^2}{T + R + S}. \tag{34}$$

3.6.1.1 *Measurement Procedure*

A detailed measurement procedure to determine the NECR is given in [48]. For small animal applications, there are three defined phantoms to choose from taking into account the prospective application of the PET device under test.

For SAFIR with mice being the prime animal to be scanned, a mouse-like phantom is used, which consists of a 70 mm long cylinder with 25 mm diameter made from high-density polyethylene. The source is contained within a cylindrical hole (3.2 mm diameter) parallel to the central axis and at 10 mm radial distance from the center. The central 60 mm of this hole are filled with ^{18}F. Data is acquired at different activities, such that each acquisition contains at least 500000 prompt

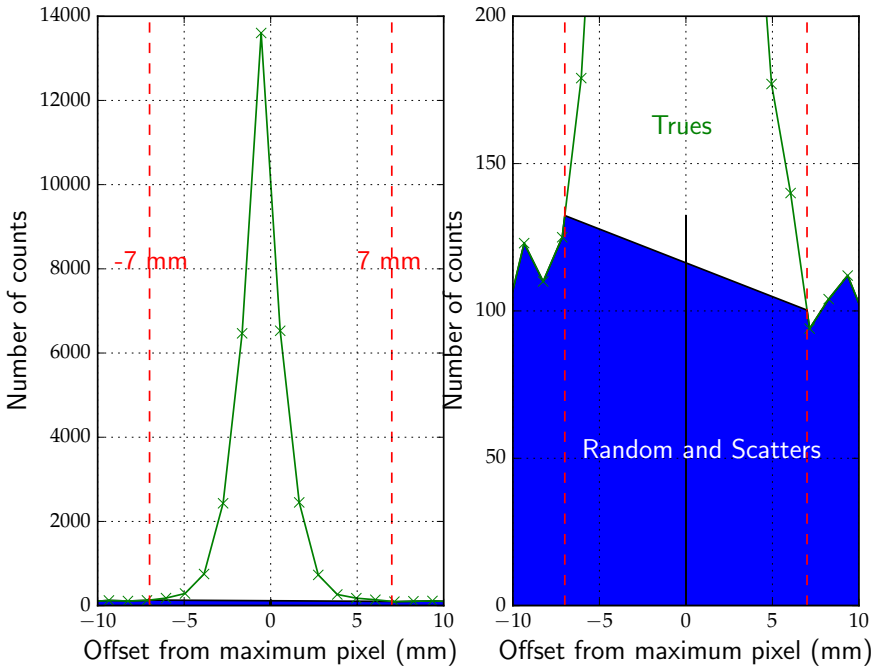

Figure 18: An exemplary NECR slice after summing all rows to find a projection profile. The left shows the complete profile while the right shows a zoomed region of the left plot. Randoms and scatters are distinguished from trues by assuming only the former outside a region of 7 mm from the maximum pixel value.

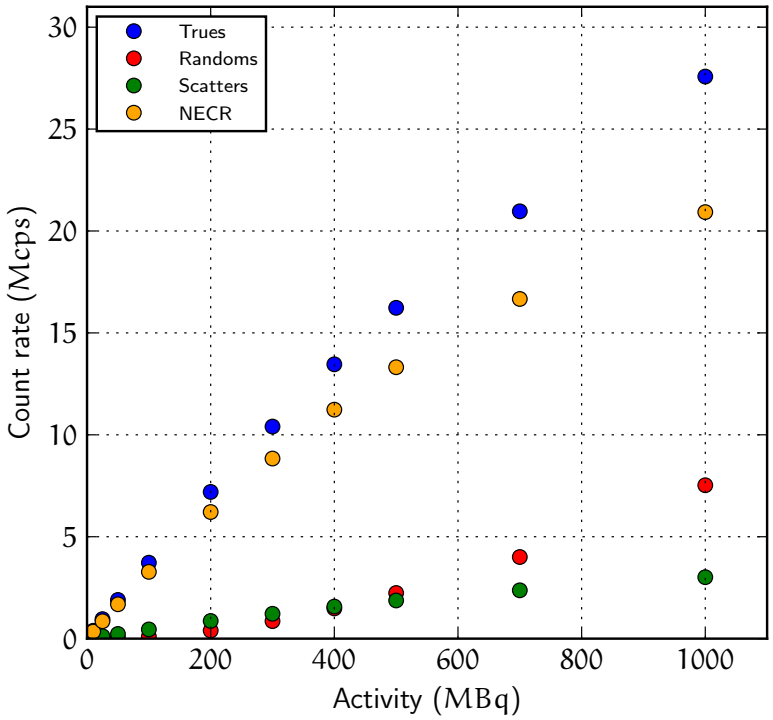

(a) Using only the golden events.

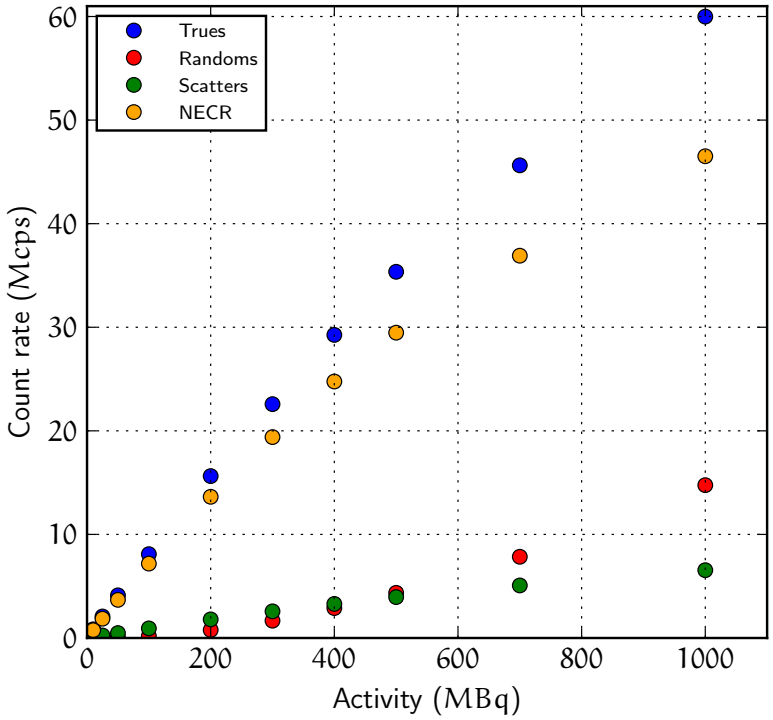

(b) With inter-crystal scattering recovery up to a maximum crystal distance of 4.

Figure 19: NEMA NECR of the SAFIR reference design with only golden events taken and with the recovery of inter-crystal scattered events.

counts. The data is sorted into sinograms and SSRB [24] is used to collapse all oblique sinograms into the direct planes.

In each direct sinogram, all pixels that are located more than 8 mm outward from the edge of the phantom are set equal to 0. For each row of the sinogram (i.e. each projection angle), the maximum pixel is found and the row shifted such, that this pixel is in the center of the row. All rows are then summed to provide a projection. An example of such a projection is shown in figure 18. All counts outside a 7 mm region around the maximum value are considered to be either random or scattered coincidences. In the central region, the values at the borders are taken and linearly interpolated. The true coincidences are found by subtracting these events from the prompt counts. The rate of random coincidences is estimated using either a delayed coincidence window, or the singles, or the MC information in the case of simulations.

3.6.1.2 *Results*

The results for the reference design without and with recovery of inter-crystal scattered events are shown in figure 19, respectively. A CRT of 400 ps and an equally long CTW was used. It can be seen that in both cases, the peak of the NECR is not reached at 500 MBq. Consequenly, the scanner is not yet dominated by random coincidences at that activity. Furthermore, the absolute magnitude of the NECR is more than doubled from 13.3 Mcps to 29.5 Mcps.

3.6.2 *Spatial Resolution*

3.6.2.1 *Measurement Procedure*

The NEMA spatial resolution of a preclinical PET scanner – SAFIR – is measured using a point-like (smaller than 0.3 mm in all directions) ^{22}Na source embedded into an acrylic cube of 1 cm edge length. A low activity is used (100 kBq for the simulations) to achieve a negligible random fraction. The source positions comprise two axial positions, in the center and at one-fourth of the axial field of view (FOV) from the center. As the biggest target animals aside from mice are rats, the size of the FOV is chosen to be 150 mm resulting in an axial position of $z = 62.5$ mm from the center. Radially, data is acquired with the source positioned at 5 mm, 10 mm, 15 mm, 25 mm, and 50 mm from the center. For a clinical scanner – BPET – the same source geometry is used and data is taken for axial source positions in the center ($z = 0$) and at a quarter of the scanner length ($z = 38.475$ mm). Radially, data is taken at 10 mm and 100 mm radial offset.

At least 100000 counts are recorded for each source position. The data is sorted into sinograms using the procedure described in 3.5. Images are reconstructed using the filtered back projection 3D with

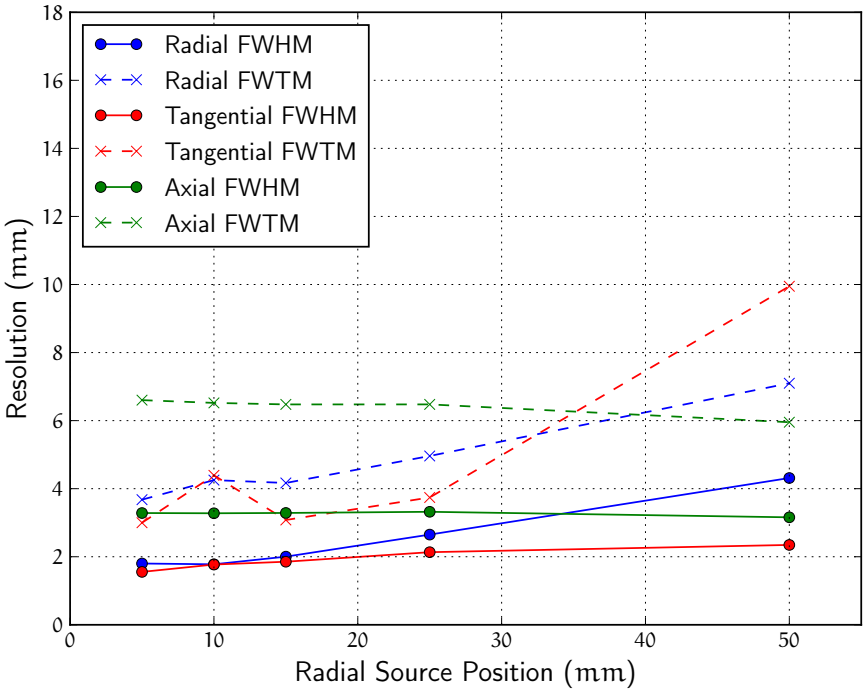

(a) Without recovery of inter-crystal scattered events.

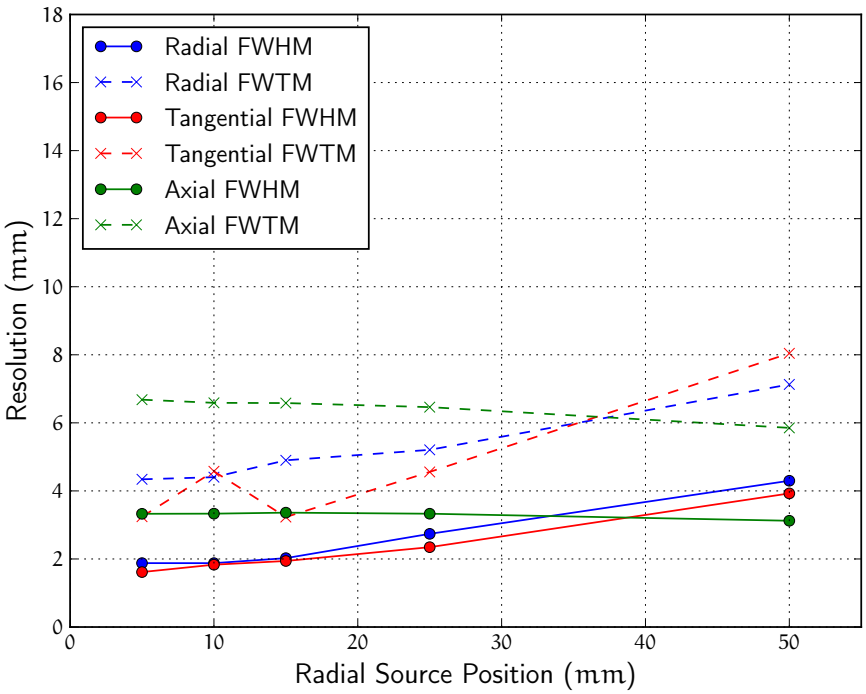

(b) With recovery of inter-crystal scattered events up to a crystal distance of ±4.

Figure 20: The results for the NEMA spatial resolution of the reference design are shown for an axial source position at the center of the FOV. Plotted are full width at half maximum (FWHM) and full width at tenth maximum (FWTM).

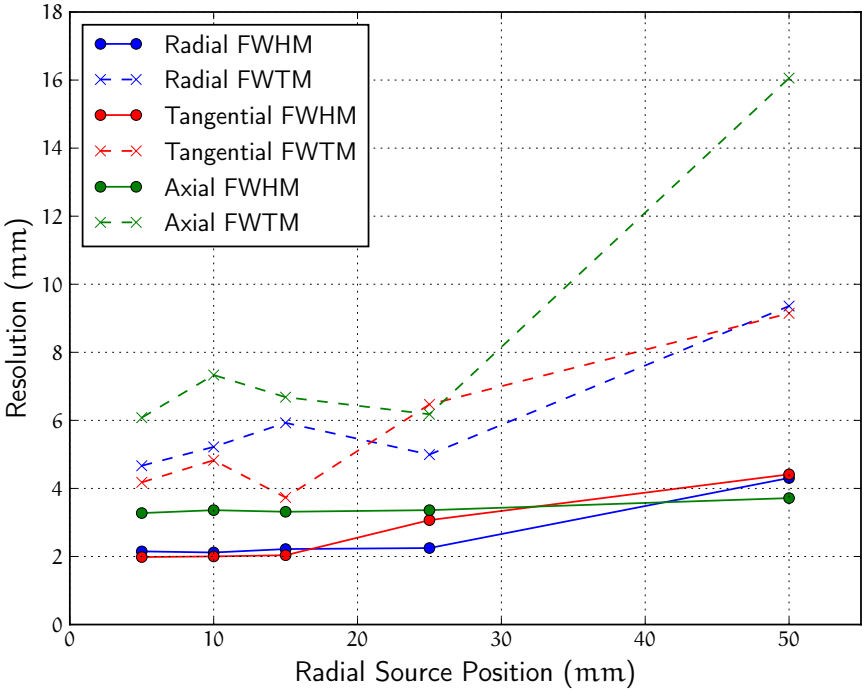

(a) Without recovery of inter-crystal scattered events.

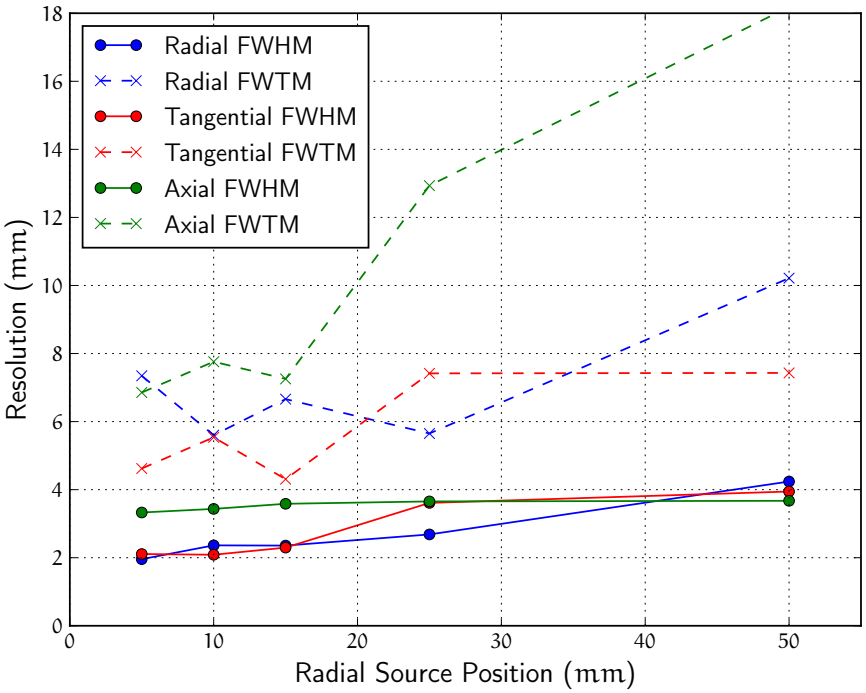

(b) With recovery of inter-crystal scattered events up to a crystal distance of ±4.

Figure 21: The results for the NEMA spatial resolution of the reference design are shown for an axial source position at one quarter of the FOV outward.

POSITION	DIRECTION	FWHM (mm)	FWTM (mm)
AA	radial	6.59	11.96
AA	tangential	7.00	12.57
AA	axial	9.63	16.62
AB	radial	6.58	11.93
AB	tangential	7.00	12.59
AB	axial	9.95	17.21
BA	radial	6.07	10.45
BA	tangential	9.90	21.04
BA	axial	10.72	19.14
BB	radial	6.52	12.35
BB	tangential	9.17	18.82
BB	axial	10.71	18.68

Table 3: The FWHM and FWTM of the spatial resolution for the BPET detector. The first letter of the position columns labels the x position (A=0 mm, B=100 mm) while the second letter indicates the z position (A=0 mm, B=38.475 mm). The direction of the profile is indicated in the second column. The voxel size is 2.15 mm × 2.15 mm × 4.3 mm.

re-projection (FBP3DRP) algorithm [32] in STIR. A utility within STIR (find_fwhm_in_image) is used to find the FWHM around the maximum pixel in three perpendicular directions.

3.6.2.2 *Results*

Spatial resolution values for SAFIR are plotted in figures 20 and 21. They are as expected: The FWHM NEMA spatial resolution at the center is of the order of the crystal size in the radial and tangential directions. While the first worsens at radially outward positions, the latter stays constant, as long as inter-crystal scattered events are not recovered. If they are recovered with even the largest considered crystal difference of ± 4, the trend in the tangential direction follows that of the radial. The axial resolution is in both cases slightly larger than 3 mm, which is due to the fact that all ring differences are used to reconstruct the point source image.

At a quarter of the FOV axial offset, the resolution is slightly worse for the FWHM but follows the same trend, except for the tangential resolution, which also worsens in the case without recovery of inter-crystal scattered events when moving radially outward. Moving the source in this direction, the FWTM is rapidly increasing and in the most extreme case is more than doubled for the axial direction. This

indicates long non-Gaussian tails due to the increased influence of oblique LORs when the source is placed radially and axially outward. On the whole, the expected spatial resolution performance of about 2 mm is met in the center of the FOV. A moderate decrease as expected is observed when moving axially or radially outward. Finally, recovering inter-crystal scatters with the simple proposed method induces a slight decrease for the tangential resolution for off-center source positions, which is still acceptable.

The results for the BPET scanner are shown in table 3. The radial resolution is always between 6 mm to 7 mm as expected for this size of crystals. The tangential resolution is slightly worse and even worse for the outer x position B. The axial resolution is around 10 mm and slightly worse for the outward positions. However, the envisioned scanner will be able to resolve the AD PET image at reduced resolution as shown in figure 15 and thus meets the requirement with respect to spatial resolution.

3.6.3 *Sensitivity*

3.6.3.1 *Definition*

The sensitivity is used to assess how many of the annihilation events are seen as coincidences in the scanner as a function of axial position. In addition, the preclinical NEMA standard [48] defines the mouse sensitivity as the average sensitivity over the axial extent of a NEMA mouse, i.e. the central 7 cm. Typical values range between 0.67 % (microPET P4) and 4.0 % (Siemens Inveon), both measured with their standard energy window (350 keV to 650 keV and 625 keV, respectively) [51]. For a clinical scanner, the sensitivity is measured in a different procedure as will be described in the following. Typical values for state-of-the-art clinical scanners range between 5.7 cps/kBq (Philips Vereos Digital, lower threshold 450 keV) and 9.7 cps/kBq (Siemens Biograph mCT, 435 kBq to 650 kBq) [8].

3.6.3.2 *Measurement Procedure*

In the following, steps only relevant for physical measurements are omitted because they are not needed for the simulation. For the SAFIR scanner, the preclinical procedure is used. The same point source with a low activity A inside an acrylic cube as for the spatial resolution is used. It is placed in the axial and transaxial center of the scanner and stepped axially outwards in both directions. In each position, a measurement is taken and 10000 true events are recorded. The time t_i it takes to record these events is recorded for each position. SSRB is applied to collapse all oblique sinograms into the direct ones. For each position, all values further than 1 cm away (axially or transaxially) from the maximum pixel are ignored and the sum N_i is calculated

TUBE	INSIDE DIAMETER (mm)	OUTSIDE DIAMETER (mm)
1	3.9	6.4
2	7.0	9.5
3	10.2	12.7
4	13.4	15.9
5	16.6	19.1

Table 4: The inside and outside diameters of the aluminum cylinders used for the clinical NEMA evaluation are stated.

for the measurement. In the simulation, no background is present such that the slice sensitivity is calculated as

$$S_i = \frac{R_i}{A}, \tag{35}$$

where $R_i = \frac{N_i}{t_i}$. The ion decay in Gate yields wrong time stamps for ^{22}Na. As a replacement, the built-in ^{18}F source is used in its place for the GATE simulations. ^{18}F is missing the direct gamma transition peak at $1.27\,MeV$ of ^{22}Na, which will cause a few additional Compton events in the photo-peak region. The differences should be minor, although visible, as a cut on the photopeak is anyhow applied. If ^{22}Na is used, a correction for its positron emission branching ratio $BR = 0.9060$ has to be applied to S_i to obtain the absolute sensitivity $S_{A,i}$. The mouse sensitivity S_{mouse} is calculated as the average over the central $7\,cm$ of the sensitivity profile.

The procedure prescribed for a clinical scanner is different from the preclinical. A $700\,mm$ long portion of a plastic tubing has to be filled with water mixed with ^{18}F of known activity. The activity has to be low enough to obtain less than 5 % randoms or less than 5 % dead time losses. To account for the attenuation due to the material surrounding the source, up to 5 cylindrical aluminum shells with a length of $700\,mm$ each and different diameters are subsequently added and a measurement is taken for each configuration. The different diameters are given in table 4. The data is processed using SSRB and the acquisition time t_j for each configuration j is chosen such as to ensure that at least 10000 counts are recorded in each slice. The rate $R_{i,j}$ for each acquisition j and slice i is determined by dividing the number of counts in that slice by the acquisition time t_j.

A count-rate correction should be applied to account for the changing activity due to the decay. For the simulation, this is omitted. The total count rate for each measurement is found as $R_j = \sum_i R_{i,j}$ for $j \in \{1, \ldots, 5\}$. The count rates R_j for each configuration are plotted against the total wall thickness between source and detector x_j and fitted with an exponential

$$R_j(x_j) = R_0 e^{-2\mu x_j}, \tag{36}$$

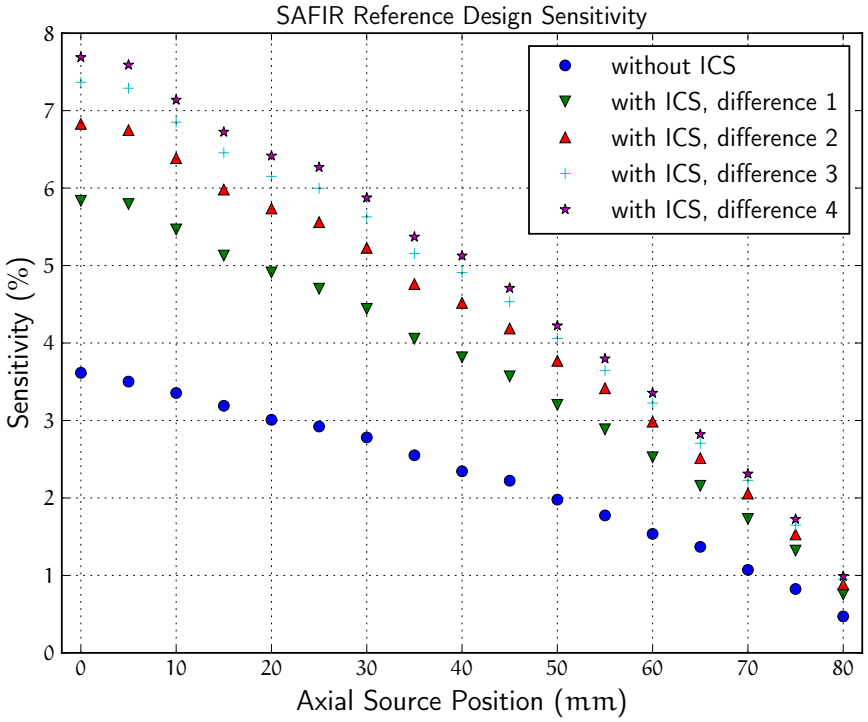

Figure 22: The results for the sensitivity of the SAFIR reference design according to NEMA is shown for the case without recovering inter-crystal scattered events and with recovering them using different maximum crystal distances. A coincidence window of 400 ps length was used and a CRT of 400 ps FWHM assumed.

where the factor of 2 is by definition of the NEMA standard. The unattenuated rate R_0 is extracted and the total sensitivity calculated as

$$S_{tot} = \frac{R_0}{A}. \tag{37}$$

The axial sensitivity profile is found by

$$S_i = \frac{R_{1,i}}{R_1} S_{tot}. \tag{38}$$

3.6.3.3 *Results*

The axial sensitivity profile for the SAFIR reference design is shown in figure 22. Three flavors of analysis were done, namely only taking the golden events (no inter-crystal scatter recovery, ICS) and recovering inter-crystal scattered events by simply summing events which are less than a maximum distance apart. The sensitivity will be the benchmarking quantity for the benefit of this procedure. Therefore, contrary to the spatial resolution evaluation, where the influence even for the biggest considered maximum crystal difference of 4 was not very large, several maximum distances (1, 2, 3, and 4) were chosen for

	PEAK	MOUSE
Golden events	3.62 %	3.08 %
Max. difference 1	5.84 %	4.99 %
Max. difference 2	6.83 %	5.84 %
Max. difference 3	7.37 %	6.29 %
Max. difference 4	7.69 %	6.56 %

Table 5: The peak and mouse sensitivities with and without the recovery of inter-crystal scattered events are reported for the SAFIR reference design.

the comparison of the sensitivities. The figures of merit, namely peak sensitivity and mouse sensitivity are summarized in table 5.

It can be seen that the sensitivity drastically improves when inter-crystal scattered events are recovered with the proposed simple algorithm. The mouse sensitivity of 6.29 % exceeds the one of the Siemens Inveon scanner by more than 50 %, when a maximum crystal difference of 3 is chosen. Choosing a higher value increases the peak and mouse sensitivities by less than 0.5 percentage points. In the following evaluation of the prototype geometries I will thus focus on this value for the crystal difference.

It is worth noting that the length of the coincidence window has a significant impact on the sensitivity. In figure 23, the impact of a larger window is shown. The curve for the shorter window is taken from figure 22, while the other is produced with the same conditions except for the longer window. This can be explained by the fact that one will cut on the tails of the distribution of the coincidences. Figure 24 shows the integral of the central section of the Gaussian as a function of the width of that section for a CRT of $\sigma = 170\,\mathrm{ps}$, corresponding to 400 ps FWHM. The increased coincidence window leads to an increase of more than 12 % of the registered events.

Figure 25 shows the results for the different prototype geometries as previously described. The STiC geometry performs best with 10.2 % peak sensitivity. Not surprisingly, the PETA geometry has a significantly lower sensitivity peaking at 5.1 % because of its shorter (10 mm) crystals and the large gaps between the modules. The peak sensitivity is partially recovered to 6.3 % when introducing two more modules or to 6.4 % using longer crystals (12 mm). However, it becomes clear that the prototype, for which the mechanical design was optimized with respect to gaps and solid angle coverage performs best.

The sensitivity results for BPET are shown in figure 26. An unattenuated rate $R_0 = 161.25\,\mathrm{cps}$ is found and yields a total system sensitivity of 1.61 cps/kBq. This is about a factor of 3.5 to 6 smaller than typical commercial system. This is expected due to the radically simplified design of BPET. However, this can be recovered in the image by us-

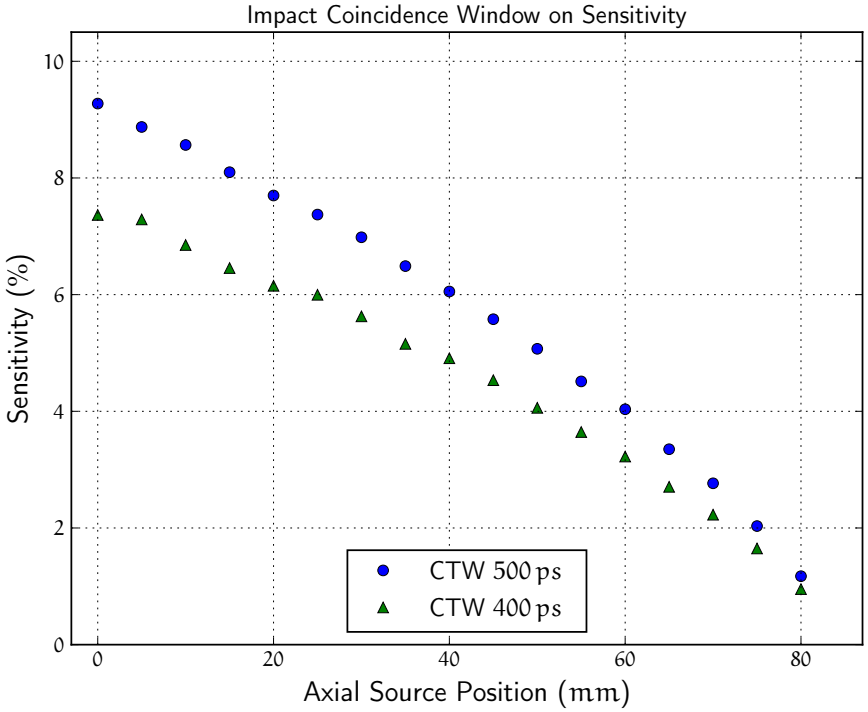

Figure 23: The impact of the coincidence window length on the sensitivity can be significant. The result is only valid for low activities, where random coincidences do not play a role.

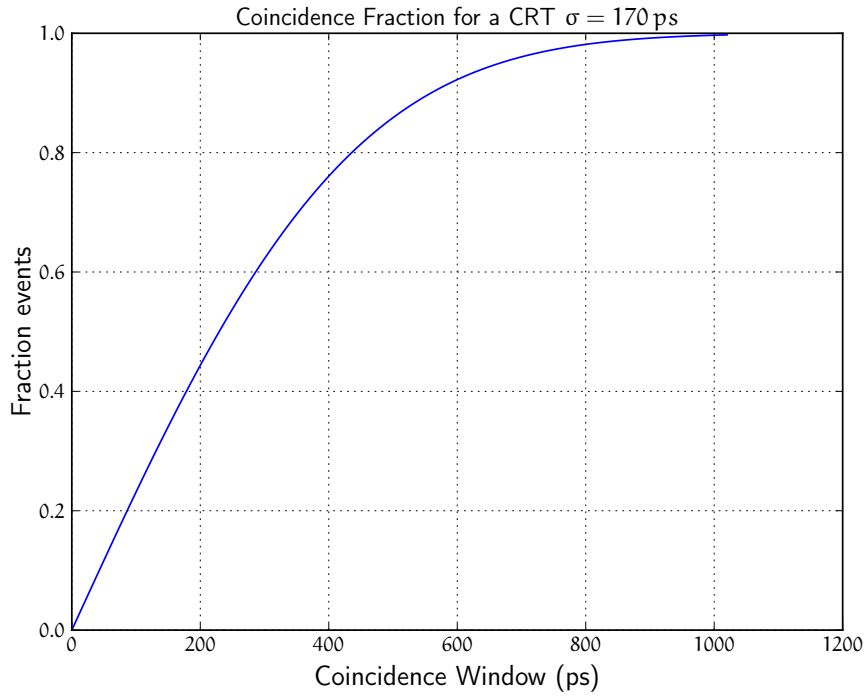

Figure 24: The fraction of coincidences within the central region of the Gaussian distribution of the time differences is shown.

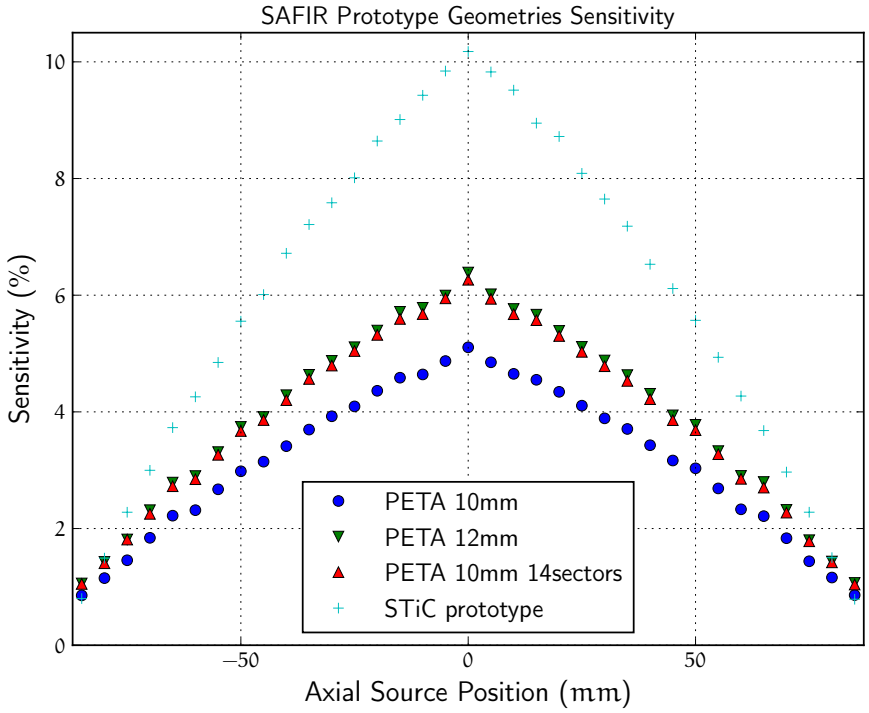

Figure 25: The results for the sensitivity of the SAFIR prototype geometries according to NEMA is shown with recovering inter-crystal scattered events using a maximum crystal distance of 3.

ing larger voxels because the activity in a given voxel scales with its volume if a locally uniform tracer distribution is assumed. In addition, longer acquisition times can be employed to record a sufficient number of counts.

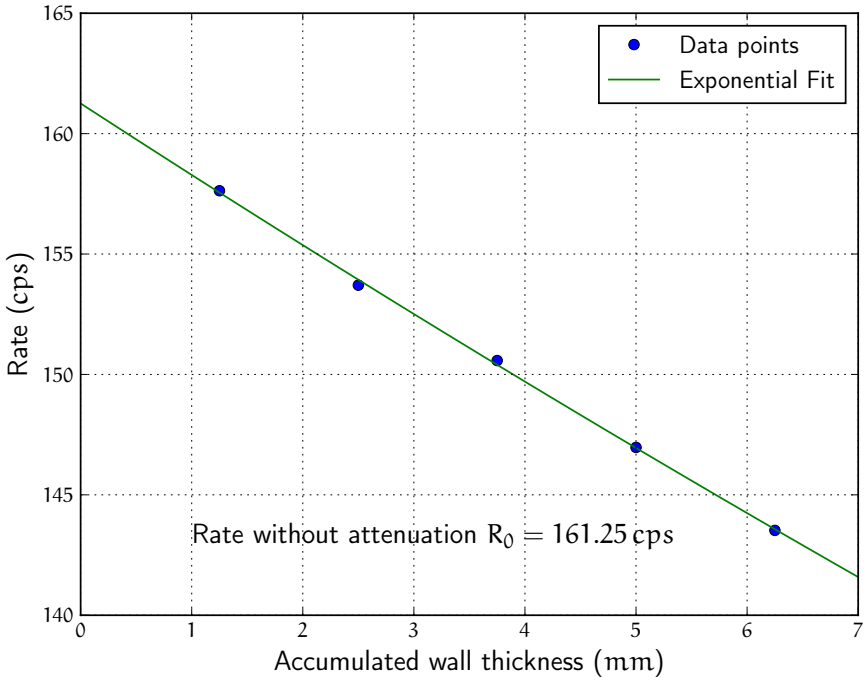

(a) The rates versus the different wall thicknesses due to the added aluminum cylinders are shown. The fit is used to extrapolate the rate without any attenuation.

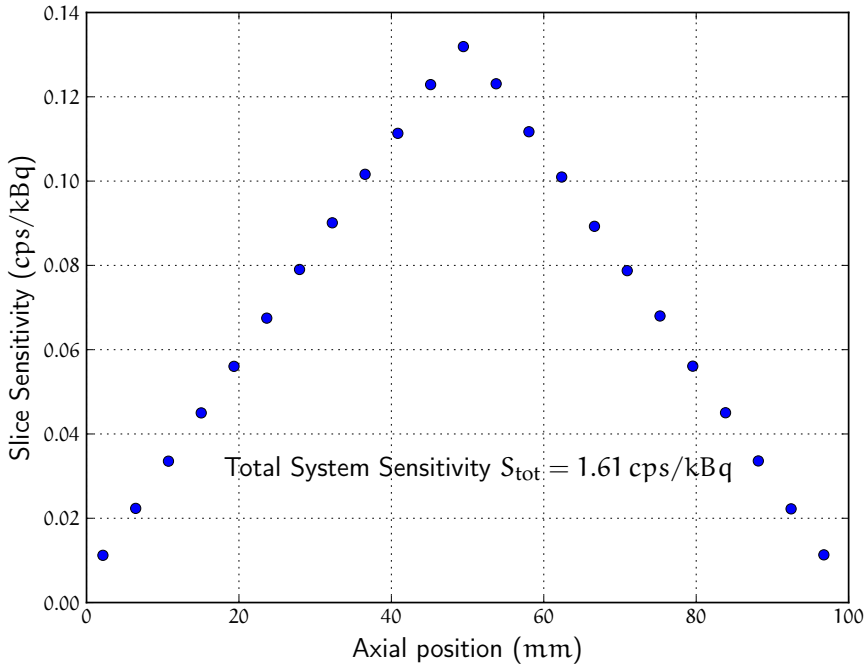

(b) The axial sensitivity profile for BPET is shown. For each position, the slice rate was used as described in the NEMA standard. The axial center of the scanner is at 50 mm.

Figure 26: BPET sensitivity rate fit and axial profile.

3.6.4 *Derenzo Phantom*

The spatial resolution measurement as defined by the NEMA standard is useful to compare different scanners. FBP is a standard algorithm that is uniquely defined. However, it will not achieve the best performance resolving small details in the images. Iterative algorithms outperform FBP in this respect. To determine how well small hot spots can be distinguished depending on their size, the Derenzo phantom [26] is a widely used phantom. It consists of small spheres of activity of different diameters arranged in triangles for each activity. The triangles are assembled to form a circle, which is embedded in a plastic phantom. Such a phantom with ball sizes 1.0 mm, 1.2 mm, 1.6 mm, 2.4 mm, 3.2 mm, and 4.0 mm (see figure 27) was simulated in the reference design geometry without background. The data was coincidence sorted with a window of 402 ps and only the golden events were selected. The length of the window was previously found to deliver the optimum NECR performance for the given CRT. The image was reconstructed using STIR and the maximum a posteriori (MAP) one step late (OSL) algorithm with a quadratic prior (penalizing the quadratic differences between neighboring voxels) and penalization factor $\beta = 5$ (a multiplicative factor to weigh the sum of the quadratic differences). More details on using EM for penalized likelihood estimation can be found in [52]. No subsets were used. Without prior, this would reduce to MLEM. The reconstructed image and profiles through all ball sizes are shown in figure 27. It is possible to distinguish ball sizes down to 1.6 mm in the profiles. Beyond that, the balls are smeared into each other showing that this geometry cannot resolve such small balls, which is expected for this crystal size.

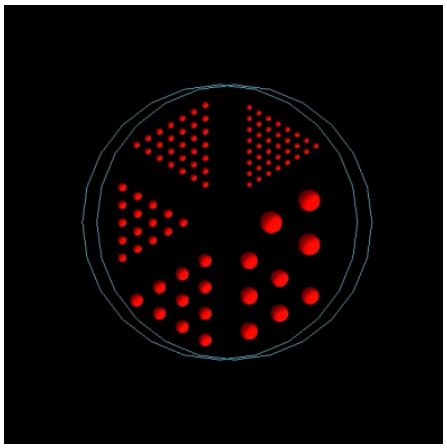

(a) Simulated Derenzo phantom arrangement with ball sizes 1.0 mm, 1.2 mm, 1.6 mm, 2.4 mm, 3.2 mm, and 4.0 mm.

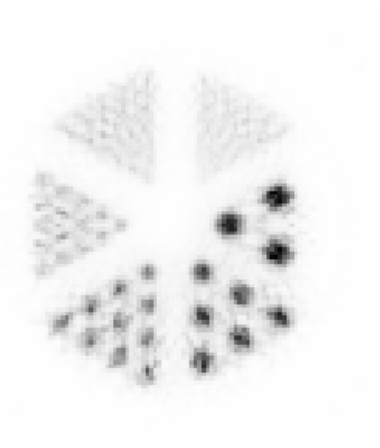

(b) Reconstructed image, MAP OSL with quadratic prior and penalization factor 5.

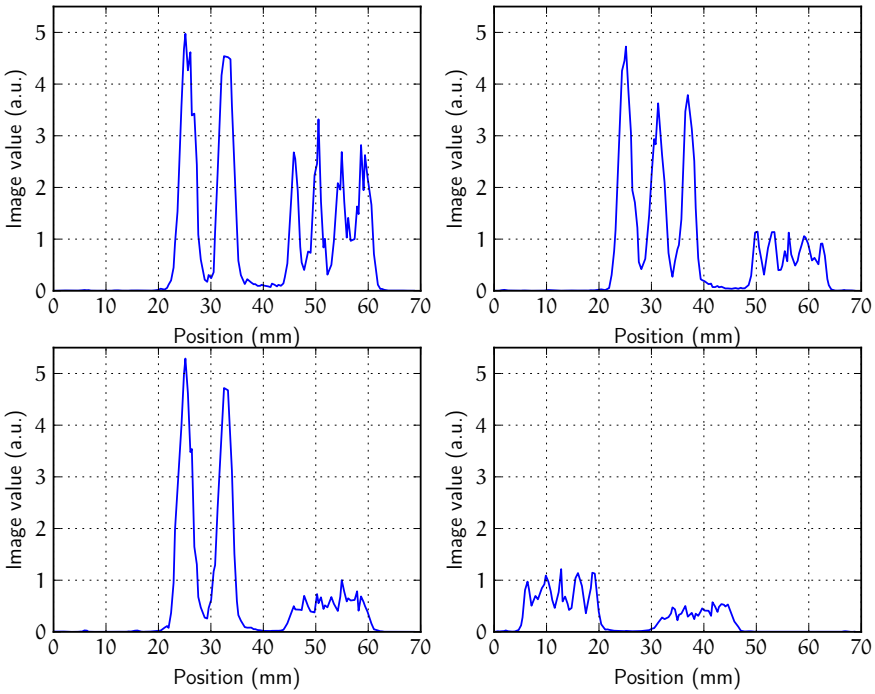

(c) Profiles through the reconstructed Derenzo balls. Top left: 4.0 mm and 2.4 mm. Top right: 3.2 mm and 1.6 mm. Bottom left: 4.0 mm and 1.2 mm. Bottom right: 1.6 mm and 1.0 mm.

Figure 27: Simulated geometry, reconstructed images, and profiles through all ball sizes in the reconstructed image of the Derenzo phantom.

4

ELECTRONICS DEVELOPMENT

This chapter contains a description of key components of the electronics design for SAFIR. BPET is not yet at this construction stage such that it will not be discussed here. Following a repetition of the SAFIR detector concept and its components in more detail, test results for optical links and power conversion components with respect to MRI compatibility are presented.

4.1 THE SAFIR DETECTOR CONCEPT

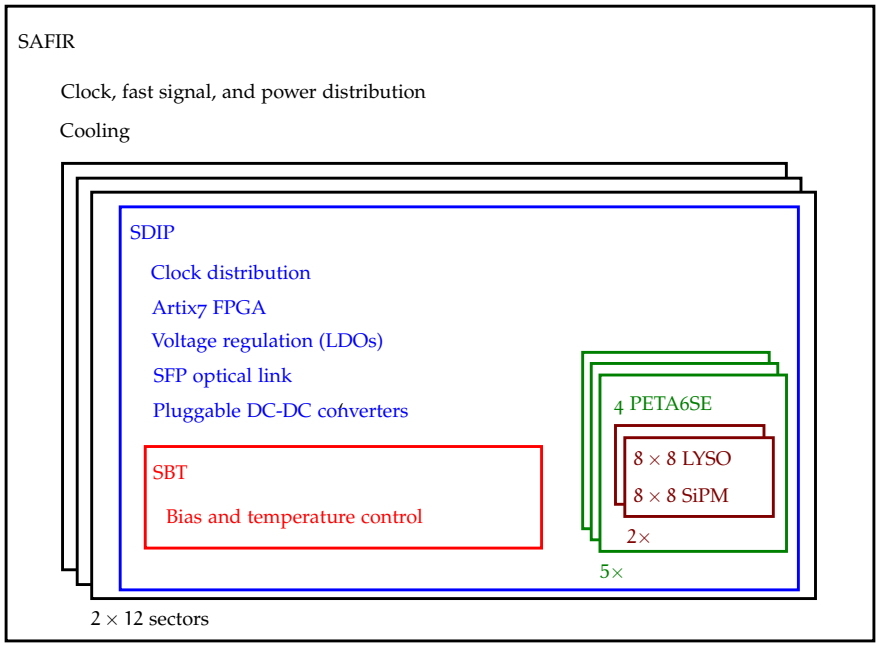

Figure 28: Block diagram of the SAFIR detector.

Developing the SAFIR detector concept uncovered many constraints, which made it challenging to find a solution for the design of the final system. Given the spatial constraints of an outer diameter of 200 mm given by the gradient coils and an inner diameter of 112 mm to fit the radio frequency (RF) coils only a little less than 4 cm radial extend is left for SAFIR. Not only does this impose severe constraints on component size and placement, in addition, only little space remains for the connection to the outside comprising power, readout, and control lines.

In figure 28, a block diagram of the SAFIR detector components is shown. The outer block incorporates the entire insert for the MRI. The

outer shell made from carbon fiber and covered with copper strips provides shielding against mutual interference between the PET and MRI systems. At either end of the shell, a flange mechanically connects the outer shell with the inner shell made from glass fiber and equally covered with copper strips for shielding. The detector is divided into two axial halves, that each consist of twelve sectors. The electronics of each sector is provided with a frequency synchronized clock and a fast reset signal from a dedicated fast signal distribution board. Furthermore, the power lines and cooling liquid from outside connections on one side of the insert are distributed to all sectors. On the same side, where the power and cooling connections are located, 24 optical fibers – one for each sector – exit the detector to be connected to the DAQ system for data output from and control input to the detector.

After first simulations of the expected singles rate per unit surface, it was clear that one-to-one coupling is the safest approach for the first prototype to not be limited by the count-rate capability of available electronics. Light-sharing to measure some depth of interaction (DOI) information will be investigated in a dedicated setup and is an option for the final detector if feasible. In the scenario of a one-to-one coupling, data from about 15000 photo-sensors has to be read out, which excludes an outside digitization due to the sheer amount of the cables needed to connect all channels individually and the limited space at the accessible end flange of the detector.

Consequently, the SAFIR not only houses the scintillator and light detection element in form of SiPMs, but incorporates as well a digitizing front-end ASIC together with a field programmable gate array (FPGA) to provide the link to the DAQ system. Including these components inside SAFIR demands for a sophisticated power supply system to power the electronics and an appropriate cooling system to cool them. The major building blocks for constructing SAFIR are described in the following subsections. Scintillator and photo-sensors were previously discussed in chapter 2. Thus, they will only be briefly discussed here.

4.1.1 *Digital Interface Board*

The interface of the detector electronics to the DAQ system is provided by a digital interface board. For the STiC and PETA systems it is called SDIS and SDIP, respectively. Its core functionality is delivered by the onboard FPGA, which controls and reads out the front-end ASICs. Data to and from the DAQ personal computer (PC) is sent and received through an optical link, which can be plugged into a small form-factor pluggable (SFP) connector. The previously described SBT is controlled through this connection as well. Furthermore, clock distribution and power conversion infrastructure for the numerous volt-

ages required by the FPGA and the front-end ASIC is integrated onto the SDIS and SDIP. I have contributed significantly to the development of the schematic of the latter. A more comprehensive description of its composition and functionality is given in B.2.1. The SDIS design has not been finalized until now. The MRI compatibility tests of several direct current (DC)-DC voltage converter modules are presented in 4.2.2.

4.1.2 *High-Speed Data Link*

Designed as a high-rate capable system, large amounts of data is expected to be measured. Consequently, the bandwidth of the data connection from the detector to the DAQ system has to be sufficient to transmit the data. An overview over the expected data rate per digital interface board and for the entire detector is given in table 6. For the calculation, I assumed a single channel hit rate of 40 kHz, which was found earlier for the full energy spectrum in simulations of the SAFIR collaboration. It does not include potentially increased rates due to optical crosstalk between channels. The PETA needs more additional bits because in the raw data words from the read-out, no channel numbers are included. For the prototype, it will be sufficient to have a Gigabit optical link, having a theoretical maximal bandwith of 125 MB s^{-1}. For the full system, the prototypes will give important hints on what rates are to be expected in the complete system. The capacity of a Gigabit Ethernet link is on the edge of sufficient bandwidth. Should it show to be insufficient, it will be upgraded to a 10 Gigabit Ethernet link. A compatibility test for a commercial SFP module in the MRI will be presented in 4.2.4.1.

ASIC	BITS PER HIT	SDIX DATA RATE	SAFIR DATA RATE
PETA 6	34+10	134 MB s^{-1}	3223 MB s^{-1}
STiC 3.1	48+4	159 MB s^{-1}	3809 MB s^{-1}
TOFPET 1	48+4	159 MB s^{-1}	3809 MB s^{-1}

Table 6: Estimated data output rate for a hit rate of 40 kHz per channel. The bits per hit include the data word plus the additional bits needed to address the ASIC or individual channels on an SDIS or SDIP, respectively. The data rate is calculated for one digital interface board SDIx and for the entire SAFIR detector.

4.1.3 *Front-End ASIC*

During the course of the SAFIR development, three ASICs were considered as suitable for the detector. At first, STiC [37, 53–55], an ASIC developed at the Kirchoff institute for physics at University of Heidel-

berg, and TOFPET [56], available from PETsys Lisbon, were considered. Later, the PETA [38, 39], a development from the institute of computer engineering at University of Heidelberg, was added to the list of candidates. All of them offer sub-nanosecond CRT combined with energy measurement capability on all channels. However, they differ in how these measurements are implemented.

4.1.3.1 *STiC*

The STiC features a digital time-to-digital converter (TDC) combined with a time over threshold (ToT) energy measurement. It is described in doctoral theses [37, 54]. The TDC was originally developed for the PETA and is implemented as phase-locked loop (PLL) with a sixteen-stage voltage controlled oscillator (VCO) designed for 625 MHz frequency and is described in [57]. Latching the state of the oscillator provides a coarse and fine timing measurement with a fine timing bin width of 50 ps [57]. The current through the input transistor can be limited such that the SiPM is discharged with a constant current resulting in an approximately rectangular pulse shape. After pre-amplification, this pulse is discriminated at the leading (time) and trailing (energy) edge and the respective times are digitized using the TDC. The time difference between these edges is recorded as ToT, which is approximately proportional to the charge of the pulse. As a consequence, the time and energy discrimination thresholds are not independent as the timing thresholds will influence the ToT measurement. Digital data is sent out via a 160 MHz low voltage differential signaling (LVDS) link with 8b/10b encoding to an FPGA. The developers have reported a CRT of less than 285 ps [37]. In a high-rate test, we found a CRT of 305 ps using a source activity and geometric configuration to generate the rate per channel as expected in the SAFIR system [58].

4.1.3.2 *TOFPET*

The time-of-flight PET (TOFPET) ASIC uses an analog timing measurement combined with a ToT energy measurement in its first version. The analog pulse from the SiPM is discriminated at its leading and trailing edge and the times for both edges are digitized using a time-to-analog converter. Triggered by the discriminator signal, a capacitor is charged with a constant current. Upon the occurance of a coarse clock tick (frequency 625 MHz), the charge is transferred to a larger capacitor, which is in turn discharged with a smaller current. The discharge time is proportional to the initial charging time, but much longer. It can be measured using the coarse clock providing a fine time measurement. The time difference between leading and trailing edge of a pulse is used as a (non-linear) energy measurement. Two LVDS links with 160 MHz bandwidth each, additional double data

rate (DDR) capability, and 8b/10b enconding are used to deliver the acquired data to an FPGA. In an equivalent setup as in the high-rate test mentioned for the STiC, we found a CRT of 405 ps [58].

4.1.3.3 *PETA*

The TDC of the PETA ASIC has already been described in the subsection on STiC. It has a fine timing bin width of 50 ps. Its energy measurement is, however, implemented as charge integrating analog to digital converter (ADC) providing a linear energy measurement. Two front-ends, one using a differential and the other a single-ended input signal, were developed, although only the single-ended version is used for SAFIR. The energy measurement is intrinsically linear and no dependence between the time and energy thresholds are present because there are two separated signal branches. PETA is organized in two identical halves, which share some digital logic. The data is read out from shift registers via one (version 5) or up to two (single-ended PETA version 6 (PETA6SE)) 160 MHz LVDS links per chip half. It is foreseen to skip channels with no data in the shift register. Up to four channel groups per half chip can be configured. All channels in a group will be read out if one of its channels triggers. The developers have measured a CRT of 205 ps FWHM [38]. The ASIC is prepared for flip-chip bonding onto a low temperature co-fired ceramics (LTCC) module. In the most recent version, PETA6SE, the solder ball pitch has been increased to 500 µm to allow for soldering it onto PCB. We have used version 5 and 6 of the PETA ASIC. Results from a high-rate test of the PETA5 on a LTCC module will be presented in section 5.2 and PETA6SE was used to evaluate photo-sensors for BPET in section 5.1.

4.1.4 *High-Voltage Supply*

SiPMs need a bias supply voltage between 25 V to 65 V depending on type and manufacturer. To provide a stable gain, the overvoltage has to be kept stable under changing load currents and temperatures. Within SAFIR, the SBT board has been developed to provide ten channels of such a bias voltage supply. As all PCBs in SAFIR, it has to be magnetic field tolerant and have very low electromagnetic interference (EMI) emissions to not disturb the MRI significantly. The SAFIR development offers mV precision and stability regardless of the load over a set range of approximately 10 V. The supply is floating such that its overall potential difference can be shifted by an external supply. The output voltage is regulated after the current limiting bias resistor, which is also part of an RC filter. The SBT features an ATmega328 microcontroller, which reads out up to ten LMT01 temperature sensors and can adjust the voltage according to the momentary temperature of the sensor to stabilize the gain. It has a serial interface to the FPGA to set the desired output voltages per channel. The

final version of the SBT was succesfully tested inside the MRI by other members of the SAFIR collaboration.

4.1.5 *Scintillator*

LYSO is the most frequently used scintillator in present PET system developments. Its high light yield combined with its fast decay time compared to other scintillators such as bismuth germanate (BGO) make it ideal for demanding timing applications such as SAFIR. As previously discussed, the number of measured photons has a direct impact on the best achievable timing resolution. Furthermore, the length of the crystal and the attenuation length determine its stopping power for the gammas. Given the spatial constraints of the SAFIR insert, a crystal length of 10 mm to 14 mm is reasonable. The size of the crystals in the tangential and axial direction determine the approximate spatial resolution. State-of-the-art preclinical PET scanners reach up to 1 mm^3 volumetric spatial resolution where most scanners are in the range of 1 mm^3 to 10 mm^3 resolution [59]. SAFIR with its 2.1 mm × 2.1 mm × 12 mm crystals falls into this range as presented in the previous chapter.

4.1.6 *Photo-Sensors*

SiPMs are the prime choice for use inside the magnetic field of the MRI scanner, where PMTs would fail due to their working principle. Hamamatsu has been used successfully and reliably as supplier in many previous detectors built in the Institute for Particle Physics. The crystal size, which reflects the desired resolution, also dictates the size of the photo-sensor, when a one-to-one coupling scheme is used like in SAFIR. Sensors of 2 mm × 2 mm active area arranged in 8 × 8 matrices are available from Hamamatsu. The matrix S13361-2050AE-08 is the baseline choice for the final SAFIR design.

4.2 DEVELOPMENT OF THE PROTOTYPES

In section 3.1, two prototype geometries were described, one featuring the STiC and the other featuring the PETA ASIC. Originally, it was planned to develop and produce the necessary components for both variants towards two working copies of a half sector, each equipped with one PETA LTCC module or two SiPM matrices of the reference geometry, respectively. All electronics and mechanics parts of those are designed such that they will perform realistically with respect to the final system whereever possible. From tests with these prototypes, necessary changes and improvements for the final system will be deduced. Thus far, the SAS, SBT, SST, and SDIP boards have been produced and partially tested. The SBT has been fully characterized

and tested in the MRI. SST was tested in a lab test setup. SAS and SDIP are produced and have received some bug fixes, but have not been fully tested yet. I will describe in the following the developments towards solutions for the optical Ethernet data transmission and DC-DC voltage conversion inside the SAFIR insert with particular focus on MRI compatibility of an optical link and DC-DC voltage converters.

4.2.1 *Mechanics*

The mechanical structure of the SAFIR scanner needs to fulfill three main purposes: to provide support for all components, to provide shielding from the RF pulses of the MRI, and to provide cooling to the electronic components. An introduction to shielding effectiveness can be found in [60]. Glass and carbon fiber composite materials as well as copper shielding have been identified as main materials for the outer and inner shell. Stability is provided by the fiber composite material. Among the two options, carbon fiber has the additional advantage of providing some RF shielding while being transparent to low frequency signals like from the MRI gradient system. Additional shielding is accomplished by applying thin strips of copper tape to the composite material. The geometry is chosen such that no large conducting surfaces exist, which could host eddy currents induced by the switching of the MRI. Refinement of the shell construction and shielding are ongoing in the SAFIR collaboration. A first version of the inner and outer shell as well as the connecting flanges at either side of the cylindrical shells were produced from glass fiber and equipped with overlapping but DC isolated copper strips. This model will be referred to as prototype cylinder later when presenting MRI compatibility test measurements.

4.2.2 *Power Distribution*

One main challenge of a highly integrated detector such as SAFIR is the distribution of sufficient power to the electronic components of the detector. The bulk consumption is due to the analog part of the read-out ASIC, in case of the PETA up to 2.6 A at 1.8 V per module, closely followed by the FPGA, in case of the Artix7 roughly 2.5 A at 1 V for the internal supply. In addition, several more supplies are needed for the SDIP. Given the mechanical constraints at the flange, it is not feasible to individually supply these voltages from the outside.

Instead, a power distribution system featuring four intermediate rails was developed using the Texas Instruments Webench (`http://webench.ti.com`) tool. This tool allows entering the required output voltages and ripple properties and suggests a solution optimized with respect to efficiency, footprint, and cost.

For the prototype boards, the mechanical constraints are not as binding as in the final system because not all sectors will be occupied with electronics. Therefore, a solution has been chosen, where the final adjustment will be done by low dropout (LDO) voltage regulators on the digital interface board, SDIP or SDIS, respectively. The intermediate rail voltages are generated from 12 V to 16 V by custom magnetic field tolerant DC-DC buck converters on piggy-back boards. This limits the current flowing through the power cables from the outside because less current is needed for the same power at a higher voltage,

$$P = U \cdot I, \tag{39}$$

where P is the power, U is the voltage, and I is the current. For the prototype setup, the intermediate rail voltages could be supplied externally if needed.

The advantage of LDOs is their stable output voltage and that no inductor is needed for the operation while the advantage of DC-DC buck converters is their high efficiency, which can be higher than 90%.

4.2.2.1 *DC-DC buck converters*

The basic schematic of a synchronous buck converter is shown in figure 29. A non-synchronous buck converter would feature a diode instead of switch SW_2. A description of the working principle can be found in [61] and the most important insights are presented in the following. In a buck converter, the input voltage V_{in} is always higher than the output voltage V_{out}. Two switches SW_1 and SW_2 which are typically operated at several hundred kHz up to several MHz are used to achieve the voltage conversion.

Let the state where SW_1 is closed and SW_2 is open be called the on-state and the state where SW_1 is open and SW_2 is closed the off-state. Let the duration of the on- and off-states be t_{on} and t_{off}, respectively. The period of the switching is $T := t_{on} + t_{off}$ and the duty cycle $d = \frac{t_{on}}{T}$.

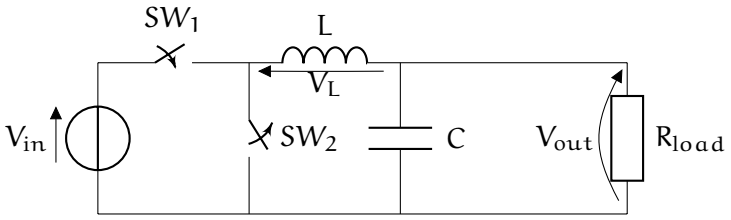

Figure 29: Synchronous buck converter.

At $t = 0$ an on-state begins. Assuming the ideal schematic of figure 29, the voltage across the inductor with inductance L is

$$V_L = V_{in} - V_{out} = L\frac{dI_L}{dt}, \tag{40}$$

resulting in a current change of

$$\Delta I_{L,on} = \int_0^{Td} \frac{V_{in} - V_{out}}{L} dt = \frac{V_{in} - V_{out}}{L} Td. \tag{41}$$

During the off-state, the voltage across the inductor is $V_L = -V_{out}$, resulting in a current change of

$$\Delta I_{L,off} = -\int_{Td}^{T} \frac{V_{out}}{L} dt = -\frac{V_{out}}{L}(1-d)T. \tag{42}$$

Demanding equality that the sum of current changes vanishes yields

$$d = \frac{V_{out}}{V_{in}}. \tag{43}$$

The duty cycle can thus be used to set the output voltage.

4.2.2.2 *Low-Dropout Regulators*

The principle of LDOs is outlined in Appendix A of [62]. A simplified schematic is shown in figure 30. The input is connected via a transistor with the output. Using a voltage divider R_1, R_2, the output voltage is compared to a reference voltage V_{ref} using an operational amplifier, which controls the gate of the transistor. The choice of the voltage divider given by the resistors R_1, R_2 determines the output voltage

$$V_{out} = \left(1 + \frac{R_2}{R_1}\right) V_{ref}, \tag{44}$$

which can be adjusted with these two resistors. Neglecting the quiescent current needed to drive the interal circuitry of the LDO, the current I is the same on the input and output side of the transistor, whereas the voltage is different. This leads to a power dissipation of $P = (V_{in} - V_{out}) \cdot I$.

While LDOs provide a very stable and noise-free output voltage, the heat dissipation is a drawback, which has to be minimized in a confined system such as SAFIR.

4.2.2.3 *Mixed Powering Scheme for SAFIR*

The prototypes contain already all electronics components needed for the final system. Among those are parts which require very accurate voltages with a low noise level. The analog part of the front-end ASICs

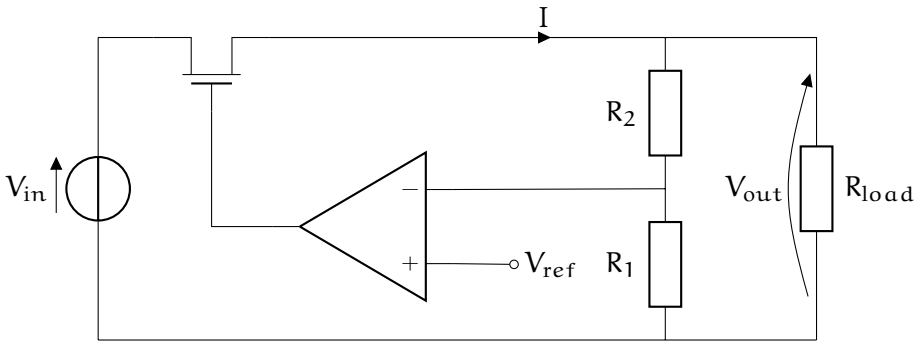

Figure 30: LDO regulator.

fall into this category as well as the supply voltages of the FPGA, which are as low as 1 V with a required precision of ±5 %. It was thus decided to use a two-step voltage regulation system (figure 31): The externally applied 12 V to 16 V are converted to four intermediate rail voltages – 4.1 V, 3.2 V, 2.4 V, and 1.8 V – using high efficiency DC-DC buck converters. All final voltages for the components are made from the intermediate rails using LDOs. Additionally, the intermediate voltages can be applied directly to the prototype SDIP in case of problems with the buck converters. This ensures a reliable voltage regulation for all sensitive components and reduces the risk of system failures resulting from incorrect external voltages.

4.2.3 *Clock Generation and Distribution*

The front-end ASICs need a very precise reference clock for their coarse counters. In addition, the FPGA needs a reference clock for its logic as well as for its Gigabit transceivers. The following describes the clock generation and distribution framework as realized on the prototype SDIP. The latter does not have to be synchronized to any other clock as Ethernet is an asynchronous protocol. The reference clock for the Gigabit transceiver of the FPGA is thus generated independently of all other clocks by a very precise Silicon Labs 531BC125M000DG crystal oscillator with 125 MHz frequency, sub-nanosecond phase jitter, and ±20 ppm total stability [63].

A block diagram of the clock distribution is shown in figure 32. The coarse counter reference clock and the FPGA logic clock are derived from the same oscillator. It is an Abracon ASG-D-X-A-622.08 crystal oscillator with 622.08 MHz nominal frequency. The three clock outputs without any division for the LTCC modules are generated by cascading two Analog Devices AD9513 clock distribution integrated circuits (ICs). The IC was used by the PETA designers on their board and thus chosen for the first iteration of the SDIP. One output is configured to divide the frequency by a factor of 9, 6, 4, or 2 corresponding

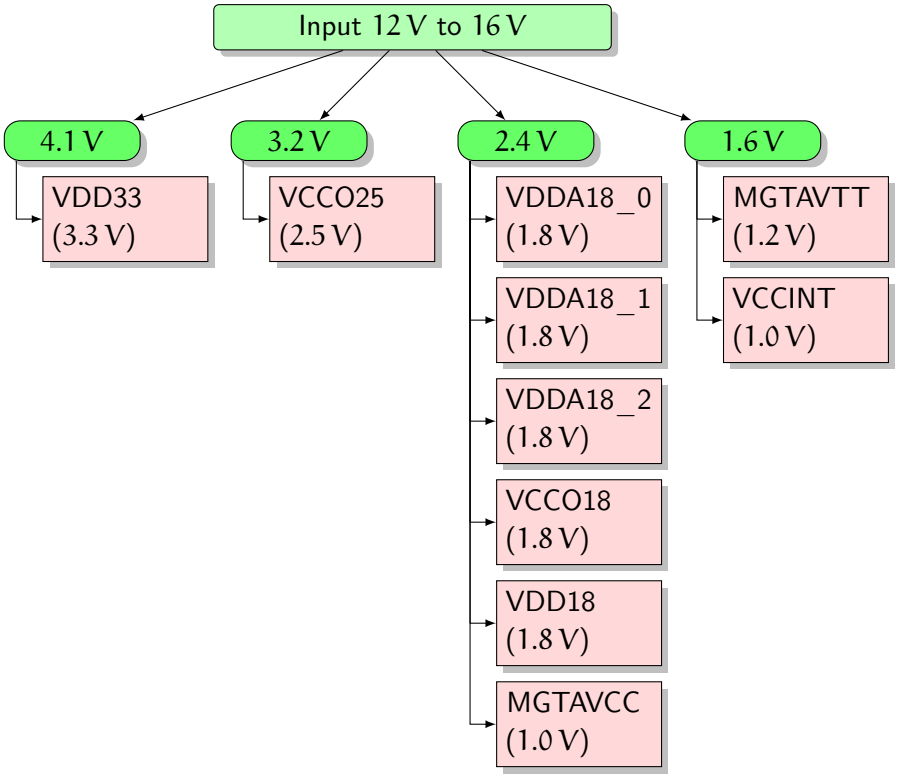

Figure 31: SDIP powering scheme with intermediate rails provided by efficient DC-DC buck converters (green) and final voltages generated by LDOs in the prototype (red). Not pictured is an additional 3.3 V rail directly deduced from the input power to supply the power sequencing logic for the LDOs.

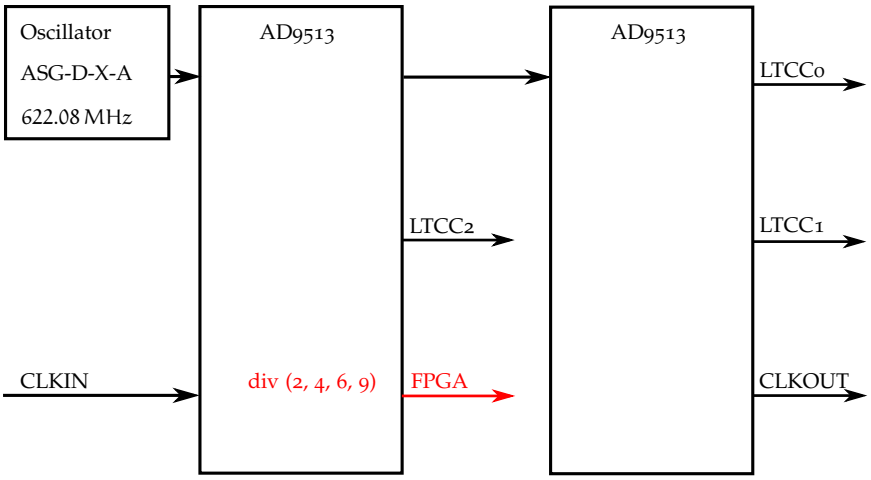

Figure 32: Clock distribution on the prototype SDIP. The AD9513 are clock fan-out and divider ICs. Except for the FPGA clock, which can be divided by a selectable integer, all outputs replicate the input frequency from the oscillator or the CLKIN connector.

to frequencies 69.12 MHz, 103.68 MHz, 155.52 MHz, or 311.04 MHz. This output is connected to a clock input of the FPGA and foreseen as its clock. In hindsight and for the future, it might be advantageous to use a more appropriate clock IC instead of cascading two. Using for example the Silicon Labs Si5345 [64] clock multiplier and jitter attenuator with ten outputs, one reference oscillator of 125 MHz would suffice to provide reference signals to the Gigabit transceivers, the FPGA, and the PETA ASICs using appropriate clock multiplication factors.

In the future, the Gigabit transceivers' recovered RX clock could be used in combination with Si5345 to obtain a frequency synchronized clock signal of 125 MHz throughout the SAFIR detector. The IC can be used as a jitter attenuator, allowing to use a high-jitter clock driving a low-jitter requiring circuit. The problem of time synchronization remains, but might be solved by fast reset signal distribution networks. The IC is designed for use in Synchronous Ethernet networks, which solve a similar synchronization problem. The other frequencies can be synthesized from the 125 MHz.

4.2.4 *MRI Compatibility Tests*

4.2.4.1 *Optical Link*

As previously mentioned, sending the data out of the scanner with sufficient bandwidth is of prime importance to SAFIR. As an additional complication, the data link has to work inside the MRI. While a solution in form of a module developed by conseil européen pour la recherche nucléaire (CERN) exists (the Versatile Link [65, 66]), it is very expensive, not readily available, and not completely compliant with the SFP specifications electronically and mechanically. Therefore, I selected the commercial SFP module Avago AFBR-57R5APZ [67] for testing inside the MRI.

The setup is shown in figure 33. A PCB was designed containing an SFP cage to host the module. Transmit and receive lines are shorted such that all received data will be looped back. The module is powered via a screw terminal followed by a linear regulator, whose output is LC-filtered for the receive and transmit power lines separately using air core inductors. The module is hosted on a plastic holder which fits the bore of the Bruker BioSpec 70/30 USR MRI scanner. On the inside, space is left for the RF coil. The module on the holder is placed in a realistic position for the electronics of SAFIR.

The module is connected with an OM-3 fiber to another module of the same kind placed outside the MRI room in a Spartan SP-605 evaluation kit. While MRI sequences were run, pseudo random binary sequences (PRBSs)-7 were transmitted at 2.5 $\mathrm{Gbit\,s^{-1}}$ using the Xilinx integrated bit error rate test (IBERT) core. The received sequences after

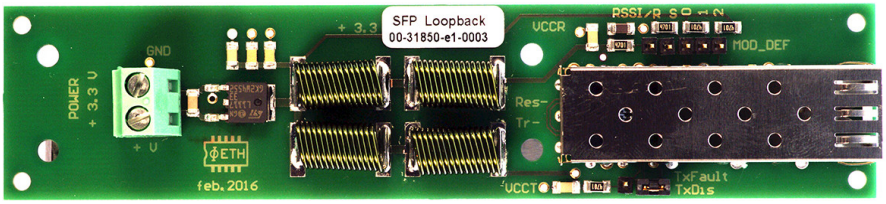

(a) Loopback PCB with power input, LDO, LC filter network, and SFP cage (from left to right).

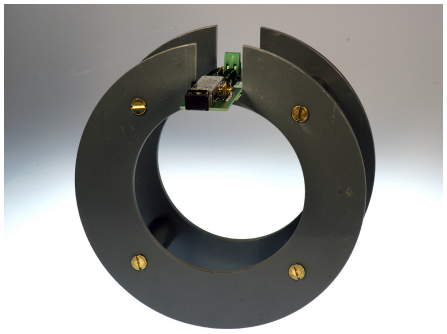

(b) Loopback PCB on holder to fit in MRI bore.

(c) PCB holder inserted in MRI bore with power cable (red and black) and optical fiber (purple) running out.

Figure 33: Setup to test MRI compatibility of SFP module.

loopback are checked for bit errors. Table 7 contains the results of this test: no bit errors where found in over an hour corresponding to a bit error ratio (BER) of $9.779 \cdot 10^{-14}$ or less. Repeating the same measurement for shorter duration but a twice as long fiber with a patch connector showed no errors as well.

SETUP	TIME (min)	RX BER	RX BIT COUNT
10 m fiber	64	$9.779 \cdot 10^{-14}$	$1.023 \cdot 10^{13}$
20 m fiber	8	$7.914 \cdot 10^{-13}$	$1.264 \cdot 10^{12}$

Table 7: Results of the IBERT with the SFP module placed inside the MRI. For the 20 m setup, two fibers were connected with a patch connector.

For the measurement of the disturbance of the MRI, a procedure has been developed by the SAFIR collaboration. After shimming, the Bruker quality assurance signal-to-noise (QA SNR) sequence as well as an echo-planar imaging (EPI) drift measurement are performed[1]. For both, a cylindrical MRI phantom filled with an acqueous solution is used. For the QA SNR, the signal in a defined region within the phantom is compared to the standard deviation of the background outside the phantom region. The value is normalized to the volume of the selected regions. The EPI drift measurement is a series of EPI measurements over a longer time, e.g. 20 min. Without changing the phantom, the drift of the signal is monitored over time. No significant change should be observed in an undisturbed system. Both, EPI drift and QA SNR are repeated in a system without additional parts for the baseline values.

SETUP	SNR (mm^{-3})
With module	3726
Without module	3787

Table 8: QA SNR results for the SFP module. Values are shown with and without the module inside the MRI.

The results for the QA SNR with the Avago SFP module are shown in table 8. Inserting the module does not significantly reduce the SNR ratio of the MRI measurement. The EPI drift measurement result is plotted in figure 34. Again, no significant drift can be observed, the change compared to the first 10 s is of the order of permille.

In conclusion, the Avago link works inside the MRI without introducing bit errors. In addition, it does not significantly disturb the MRI measurement. This makes it a good candidate for the data connection of the SAFIR prototypes.

1 The MRI measurements were done by Dr. Geoffrey Warnock and Afroditi Eleftheriou in all cases discussed in this thesis.

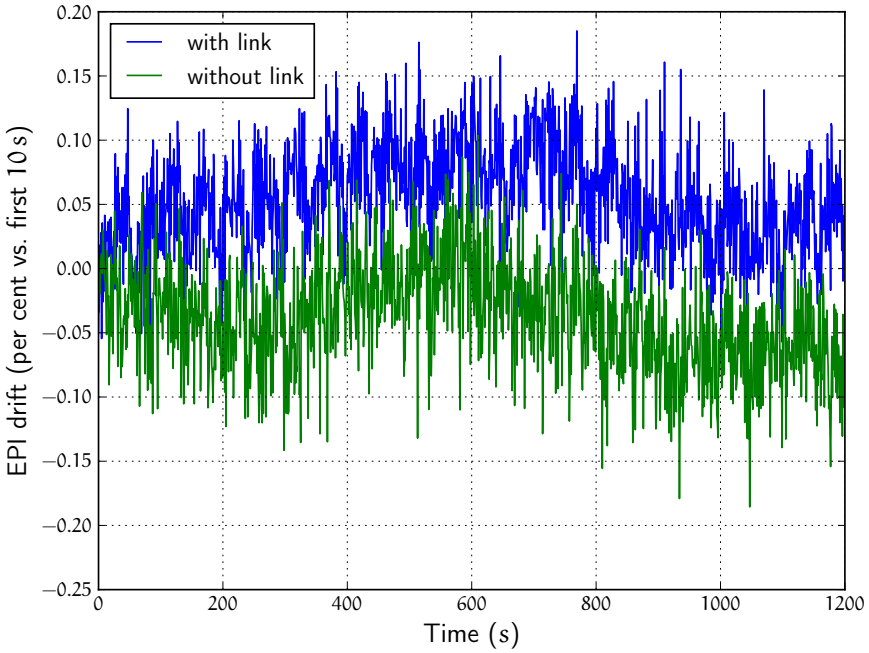

Figure 34: EPI drift measurement for the Avago AFBR-57R5APZ SFP module.

4.2.4.2 *DC-DC Converters*

Not many problems with respect to MRI compatibility are expected from the LDOs. However, the switching DC-DC buck converters can cause significant EMI due to their switching of high currents, especially when used in a sensitive environment as the MRI system. Therefore, several buck converter modules have been tested inside the MRI scanner. Among the devices tested are converters available from CERN, a development from Yale university, and two custom designs featuring commercial controller ASICs (Texas Instruments TPS62130 and TPS 40305). Using a custom design has the advantage that the form factor can be adjusted to the needs of the spatial constraints within the SAFIR detector. The CERN and the custom converters, which will be discussed in the following are pictured in figure 35.

The output of the device under test (DUT) was connected to a Maynuo M9712 electronic load to sink specified currents. For the test in the MRI, the module was mounted either on the same ring structure as the optical link or into a prototype cylinder with copper strips as shielding and inserted into the bore. If necessary, the converter was cooled with cold air from a vortex tube. While operating the converter, several repetitions of the QA SNR sequence were run.

The MRI does not cause problems for any of the converters. They work according to their specifications. On the other hand, the results of the QA SNR measurement are shown in table 9 for the CERN and the TPS62130 based custom module. No such tests were performed with the TPS40305 based module as it showed large noise emissions

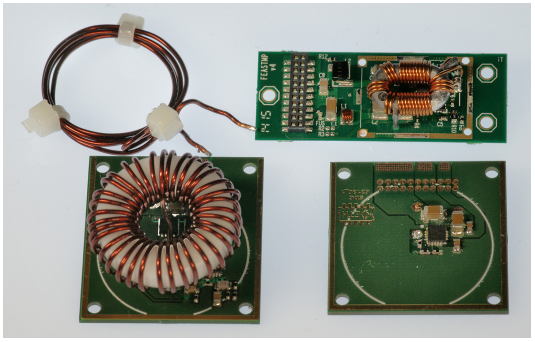

(a) CERN FEASTMP_CLP (top) and custom (bottom) buck converter modules. Top left shows a different kind of custom wound inductor. Top right shows a FEASTMP_CLP module without shielding cover. Bottom left shows a module based on the TPS40305 IC with a toroid inductor. Bottom right pictures a TPS62130 based module without an inductor.

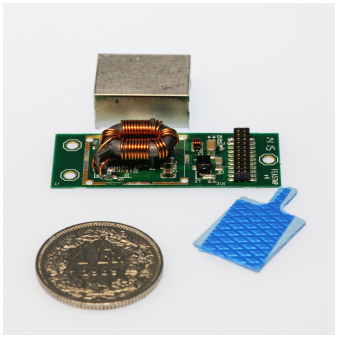

(b) CERN FEASTMP_CLP with shielding cover and heat conductive pad.

Figure 35: CERN FEASTMP_CLP and custom buck converter modules.

SETUP	SNR (mm^{-3})
FEASTMP_CLP	
3 A load current in cylinder	3863 ± 40
No converter	3787 ± 33
TPS62130 (custom)	
2 A load current in cylinder	124 ± 9
No converter	3896 ± 54

Table 9: QA SNR results for the FEASTMP_CLP buck converter module. Values are shown with and without the module inside the MRI.

already in the lab tests. While the CERN module shows no significant degradation of the MRI image quality, the custom module causes a dramatic reduction in MRI SNR. This is reflected in the corresponding MRI images in figure 36. The cylinder is almost not visible anymore in the degraded image. As a consequence, layout improvements of the converter are ongoing and shieding options are evaluated. The CERN module was also tested in an EPI drift measurement (figure 37). No significant drift could be observed. This proves the principal possibility of operating a working and non-interfering buck converter inside an MRI scanner. The custom layout will be improved in the future to deliver similar performance and compatibility.

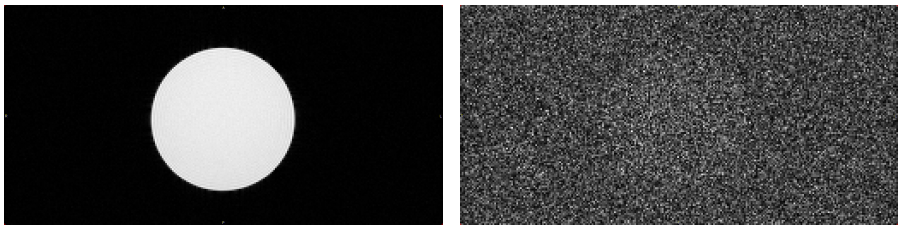

(a) No module.

(b) TPS62130 module with 2 A load current.

Figure 36: MRI images with and without TPS62130 based module.

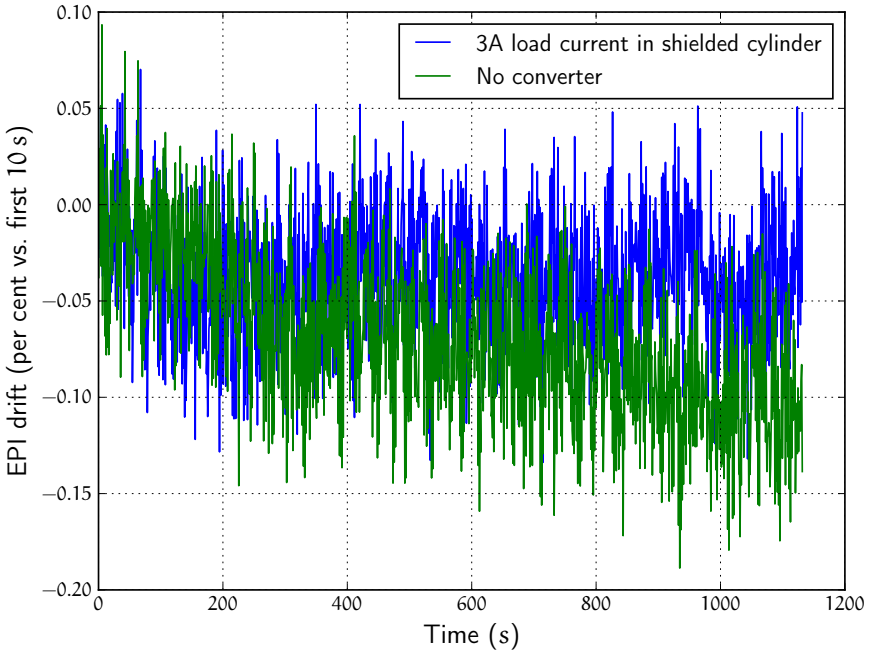

Figure 37: EPI drift measurement for the CERN FEASTMP_CLP buck converter module.

5 LAB TESTS OF PHOTO-SENSORS AND THE PETA

In this chapter, selected lab test results are shown: a direct comparison of photo-sensor timing performance for the BPET geometry and results from a high-rate test with the PETA ASIC.

5.1 PHOTO-SENSORS FOR BPET

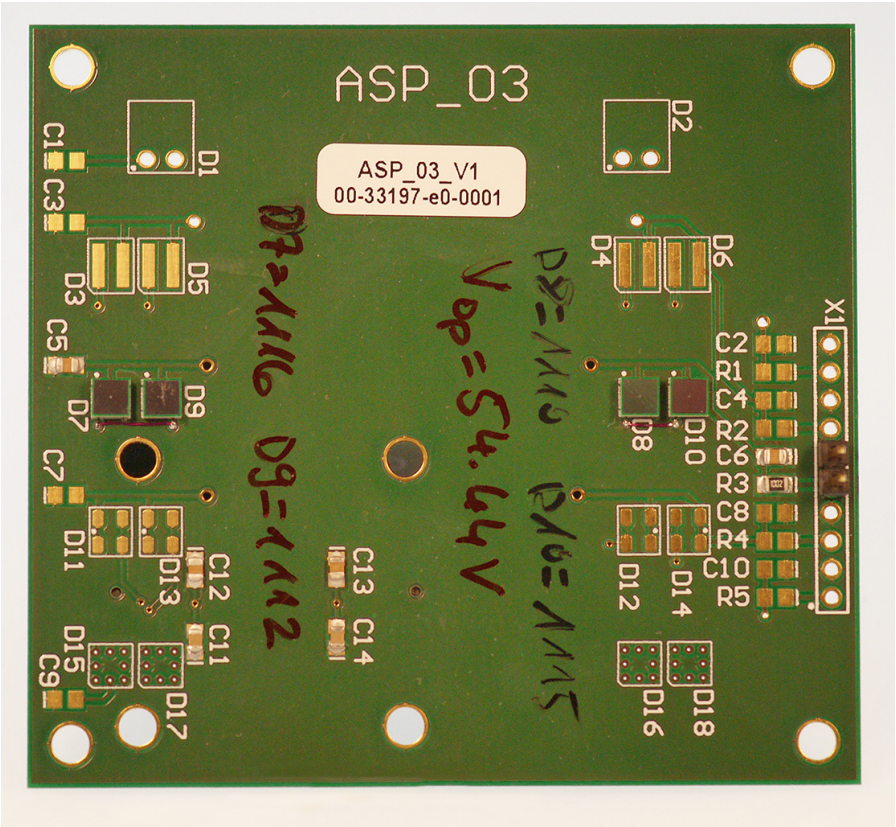

Figure 38: The photo-sensor test board with the parallel Hamamatsu sensors mounted in positions D7-D10 is shown. For each type of SiPM, a different PCB is assembled. The bias voltage is provided by means of the pin header (X1) on the right and filtered using a serial resistor (R3) and capacitances (C5, C6). The labels for the resistor and the capacitors differ for each diode type.

BPET's design incorporates a drastic reduction of sensor surface compared to covering a complete face of the crystal. In order to test if this still allows for sufficient CRT and compare the SiPMs of several manufacturers, a test setup was used comprising a 3D printed crystal and source holder and a PCB hosting a pair of sensors of each man-

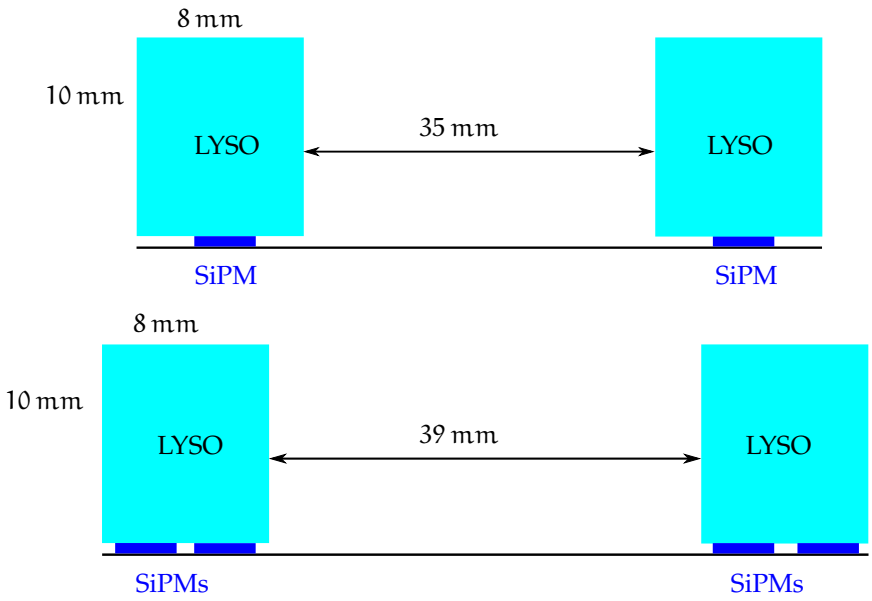

Figure 39: Sketch of crystal and photo-sensor arrangement for the test of the BPET sensors. On the top, the dimensions are shown if only a single sensor is used per side. On the bottom, the arrangement for two sensors electrically in parallel on either side is shown.

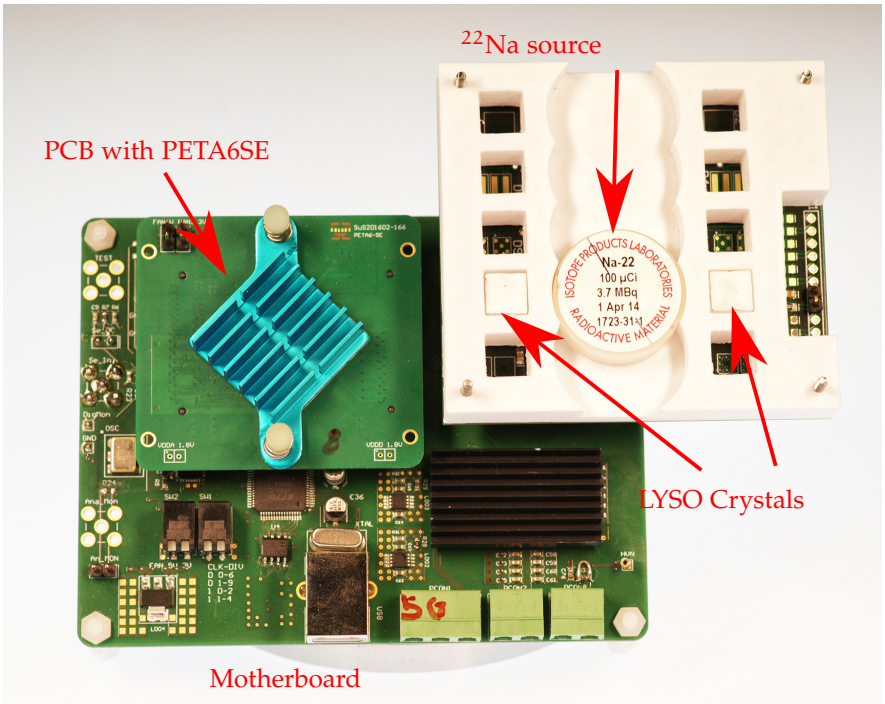

Figure 40: Picture of the complete test setup for the SiPM comparison for BPET. On the left, the PETA board with the blue cooling block covering the ASIC can be seen. It is hosted by the motherboard in the background providing power, the connections to the SiPMs, and the USB interface to the PC. At the top right, the photo-sensor test board with the white crystal and source holder are seen.

ufacturer. SiPMs from Hamamatsu (S13360-3050VE), Ketek (PM3350-EB-A0), AdvanSiD (ASD-NUV3S-P), and SensL (MicroFJ-30035-TSV) were chosen to be tested. Some of their properties are listed in tables 1 and 2 in chapter 2. Each type is currently available and has an active area of $3\,\mathrm{mm} \times 3\,\mathrm{mm}$.

On each side of the designated source position, one or two SiPMs can be mounted allowing to double the sensitive area. When two sensors are mounted on each side in parallel, the improvement of the timing resolution when using a bigger sensor can be studied. The photo-sensor test board (cf. figure 38) is connected to a PETA6SE test setup[1]. The test setup features a mezzanine board with one PETA6SE ASIC mounted onto a motherboard with an FPGA and a universal serial bus (USB) interface. Another connector on the motherboard is used to connect SiPMs to the input pins of the PETA6SE, in this case the photo-sensor test board for BPET. A 3D-printed crystal holder hosts one LYSO crystal on each side with a given distance as shown in figure 39. The crystal distance is not equal to the BPET design. This has, however, no influence on the result of the CRT measurement, where the ratio of crystal to photo-sensor surface is relevant. A picture of the setup including a radioactive source is shown in figure 40. The bias voltage is provided through pin connectors on the right-hand side of the picture and filtered using two $10\,\mathrm{nF}$ capacitors and a $10\,\mathrm{k\Omega}$ serial resistor.

In other measurements for the SAFIR project, Christian Ritzer has measured a CRT of better than $\sigma = 100\,\mathrm{ps}$ on the overall channel average. The setup comprised two Hamamatsu matrices and two LYSO crystal matrices with the dimensions of the SAFIR reference design. They were placed a few centimeter apart with the long sides of the individual crystals facing each other and with a $^{22}\mathrm{Na}$ source in between. The result means that the measurements with the BPET geometry will only depend on the crystal and SiPM size and not be limited by the electronics.

The crystals are painted with a chalk pen and placed on the photo-sensors without any additional coupling substance. A $^{22}\mathrm{Na}$ source is used to emit positrons which annihilate yielding two back-to-back gammas. They interact in the crystals, whose scinitillation light is registered by the SiPMs. The analog pulses are digitized using the PETA6SE generating data, which is recorded using an adapted version of the DAQ software written for the SAFIR project. Data for different overvoltages and different timing thresholds are taken. For each overvoltage, the gain of the ADC of the PETA is changed to ensure that the full $^{22}\mathrm{Na}$ spectrum is included in the measurement without ADC saturation. An example energy spectrum with the photo-peak, Compton edge, and the direct gamma transition peak visible is shown in figure 41. The data is read into a custom analysis framework, which is also part of

1 The test setup was kindly provided by Prof. Peter Fischer and Dr. Ilaria Sacco from the institute of Computer Engineering at University of Heidelberg.

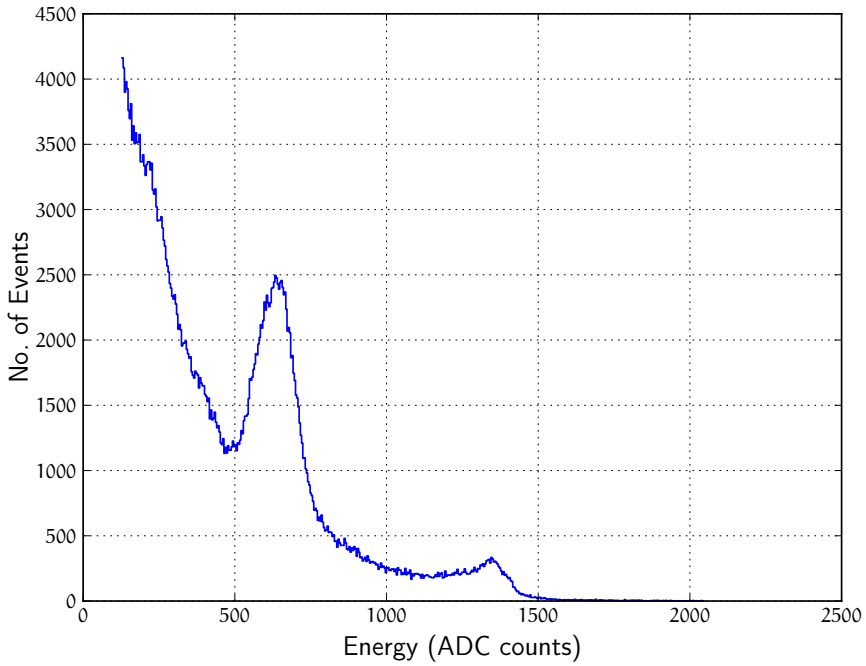

Figure 41: The energy spectrum with a Hamamatsu SiPM at 5 V overvoltage in the BPET setup. Visible are the direct gamma transition at 1275 keV (small peak at $\approx$ 1350 counts) and the photo-peak (large peak) with its Compton edge to its left. Towards the left, the background comprising Compton events and noise increases until cut-off.

SIPM	CRT (ps σ) $V_{ov} = 3\,V$	$V_{ov} = 6\,V$
Hamamatsu S13360-3050CS	547 ± 26	373 ± 10
Ketek PM3350TS-SB0	570 ± 13	–
AdvanSiD ASD-NUV3S-P	434 ± 6	389 ± 7
SensL MicroFJ-30035-TSV	516 ± 8	427 ± 4
2× Hamamatsu S13360-3050CS	652 ± 8	362 ± 2

Table 10: CRT performance of the different SiPMs types for different overvoltages and the lowest used timing threshold.

ATOM. The photopeak of each channel is fitted by a Gaussian and only events falling within $\pm 1\sigma$ of it will be used to find coincidences. An energy calibration to an absolute scale in eV was not performed such that this cannot be directly translated into Système international d'unités (SI) units. The time difference of the coincidences are histogrammed and a Gaussian is fitted to the distribution. The results are shown in figures 42, 43, 44, and 45. The same measurement with twice the photosensitive area using two Hamamatsu sensors per crystal is shown in figure 46.

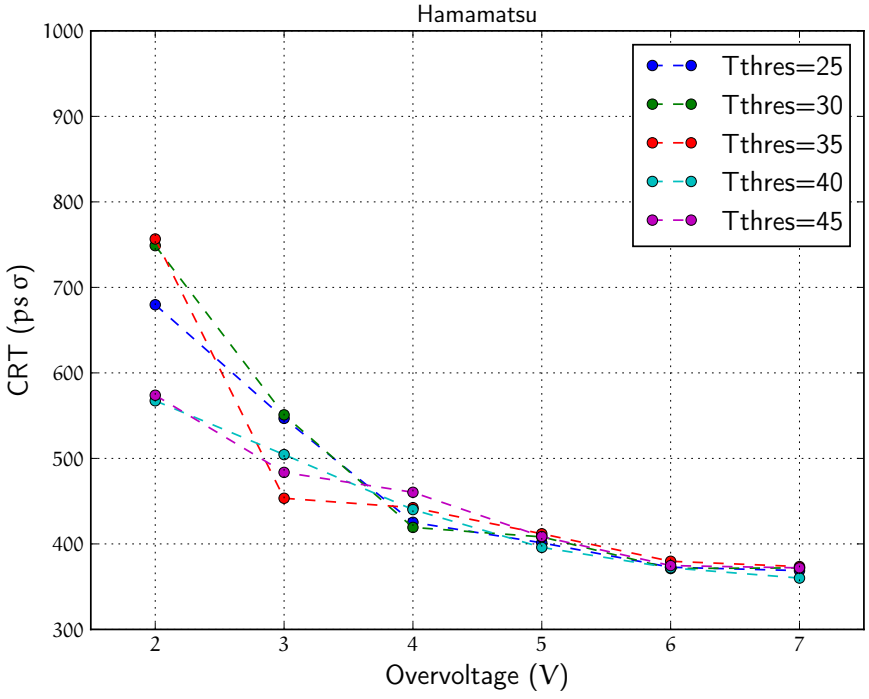

Figure 42: The CRT of a pair of Hamamatsu sensors in a setup with the BPET geometry as a function of the overvoltage and the timing threshold.

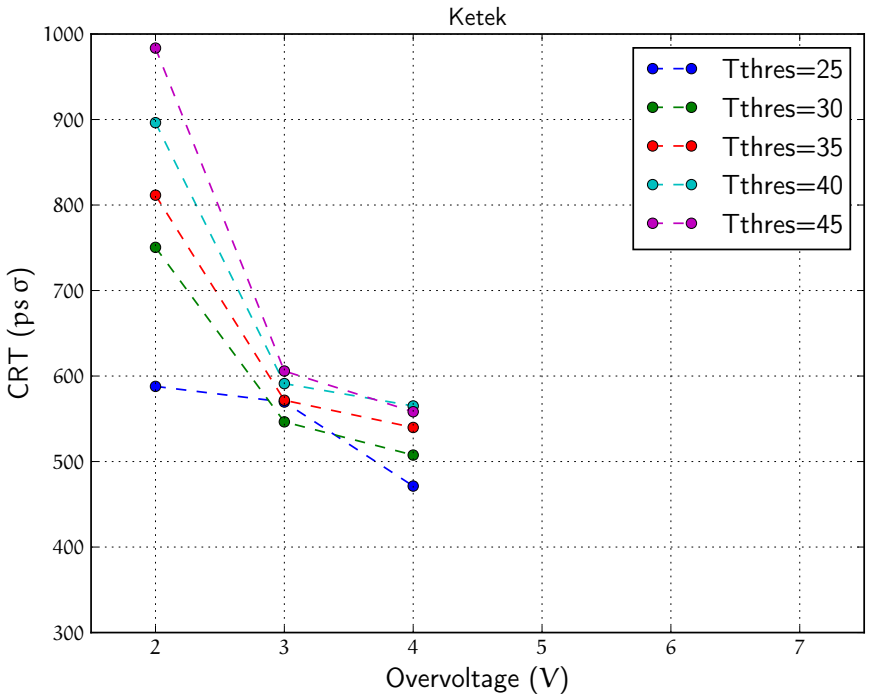

Figure 43: The CRT of a pair of Ketek sensors in a setup with the BPET geometry as a function of the overvoltage and the timing threshold. Higher overvoltages were not possible because the used Keithley bias power supply reached the current limit of 105 µA.

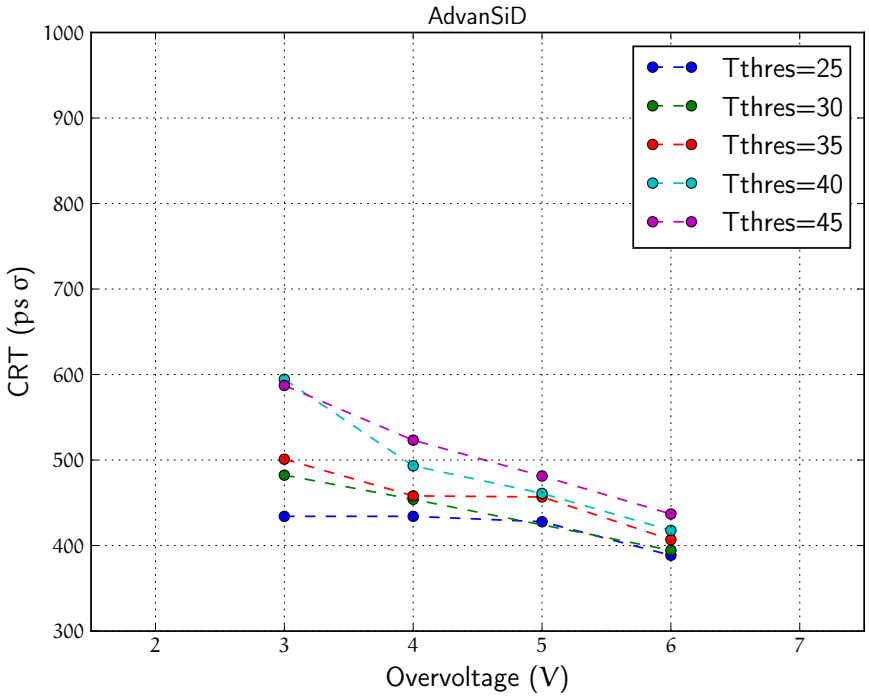

Figure 44: The CRT of a pair of AdvanSiD sensors in a setup with the BPET geometry as a function of the overvoltage and the timing threshold.

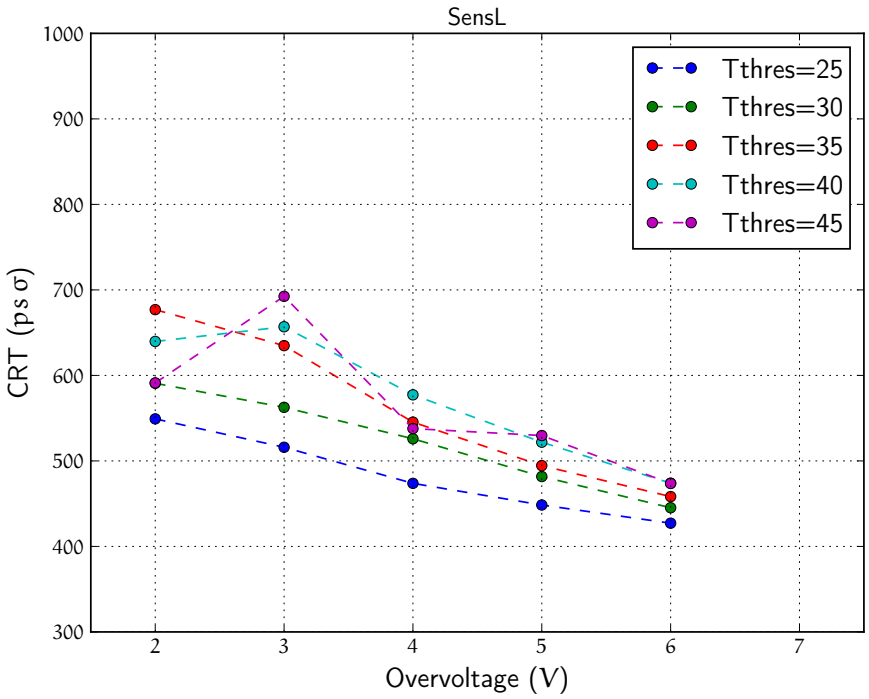

Figure 45: The CRT of a pair of SensL sensors in a setup with the BPET geometry as a function of the overvoltage and the timing threshold.

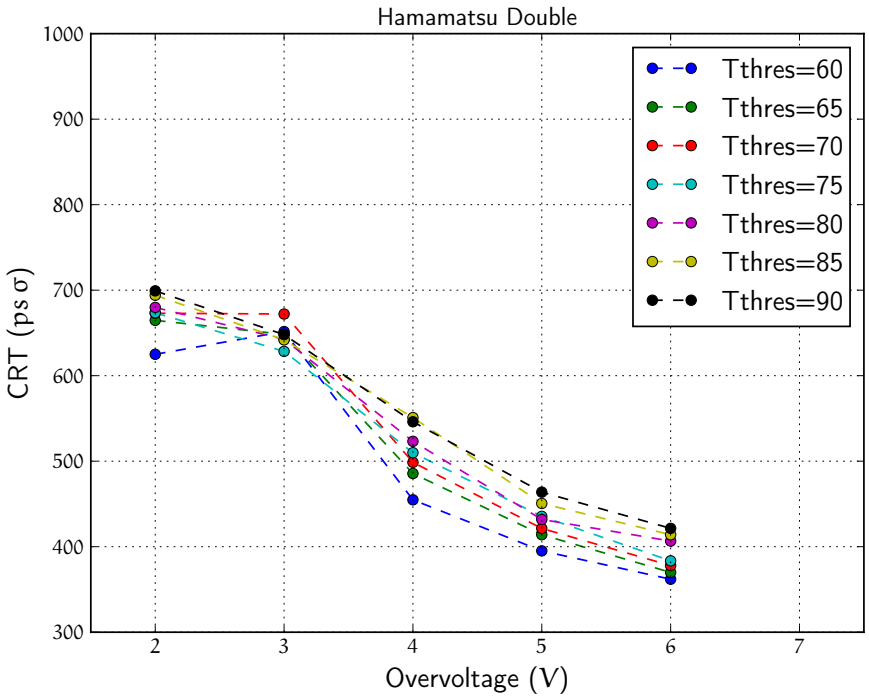

Figure 46: The CRT of a pair of Hamamatsu sensors in a setup with the BPET geometry as a function of the overvoltage and the timing threshold. The sensitive area is doubled in comparison to figure 42 by connecting two SiPMs in parallel.

An overview of the CRT values for overvoltages of 3 V and 6 V with the lowest timing threshold can be found in table 10. The sensors all show similar performance in the sense that none exceeds the performance of another by integer factors. However, subtle differences can be observed: The Ketek sensor showed a significantly higher bias current at the same overvoltage. This can be explained with the much higher gain for the same overvoltage (cf. figure 8). As a consequence, no measurement could be taken with $V_{Ov} > 4\,V$ with the available power supply. All results are stated in σ as opposed to FWHM unless otherwise stated. The best performance is achieved by the Hamamatsu sensors. Not only is their best value below 400 ps for all timing thresholds, but the spread with respect to the threshold is the smallest, in particular at high overvoltages. Other than Hamamatsu, the limit of 400 ps is only reached by AdvanSiD for high overvoltages. The performance of the Ketek sensor is about 50 ps worse than Hamamatsu at the same achievable overvoltage. The same is true for SensL. It is worth noting that all sensors would allow for a coincidence window around 4 ns, which includes $\pm 3\sigma$ of the CRT Gaussian distribution if an overvoltage of larger than 3 V is used. Doubling the sensor active area, i.e. using two Hamamatsu sensors per crystal instead of one also doubles the noise level. This is evident in the higher timing threshold values, which had to be chosen to avoid being dominated by noise events. The timing performance is not significantly improved compared to the single Hamamatsu setup. However, the spread of values with respect to the threshold is much larger for high overvoltage. Interestingly, the sensors offering a higher gain per overvoltage (Ketek followed by SensL) perform worse at the same overvoltage than AdvanSiD or Hamamatsu. This may be caused by the proportionally larger terminal capacitance for Ketek (820 pF) and SensL (1000 pF) compared to AdvanSiD (496.8 pF) and Hamamatsu (320 pF). Finally, this can explain the higher sensitivity to the timing threshold for the double Hamamatsu setup: the terminal capacitance is doubled increasing the noise level accordingly. The best achievable timing resolution is recovered due to the improved photon statistics, but a higher sensitivity of the CRT to the chosen timing threshold is involuntarily introduced at the same time. In other words, the gain in measured optical photons helps to reach the previous CRT as with one sensor. However unlike before, the CRT shows a dependency on the timing threshold.

In conclusion, the Hamamatsu sensor offers the best timing performance for the envisioned application in BPET, closely followed by AdvanSiD. The other manufacturers offer sensors, which are slightly worse, but within the same order of magnitude for this particular setup.

5.2 HIGH-RATE MEASUREMENTS WITH PETA

As previously described, the aim of the SAFIR project is to develop a high-rate capable small animal PET insert. In order to test potential read-out ASIC candidates for suitability, they were tested using a high activity source at University Hospital Zurich. In the following subsection, the first high-rate test of the PETA ASIC, which took place in summer 2015, is presented[2].

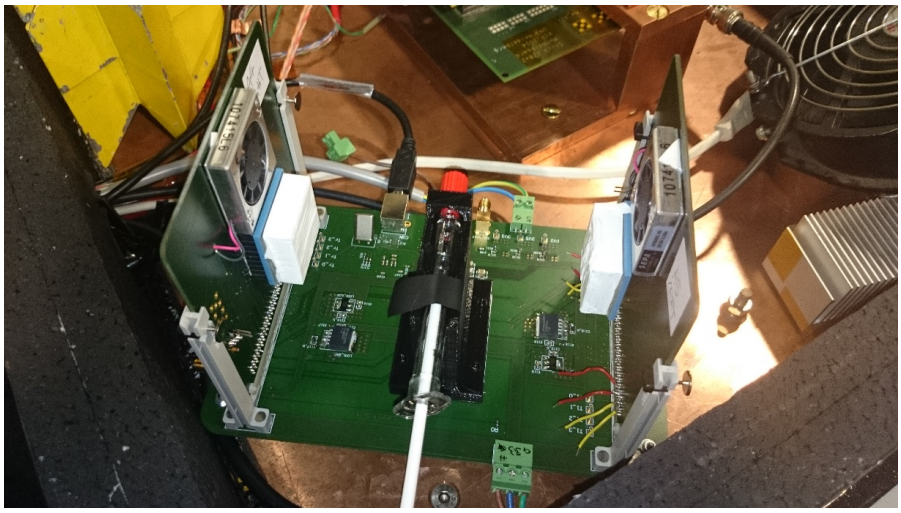

(a) Measurement setup with two LTCC modules mounted face-to-face on carrier boards. The syringe containing ^{18}F-FDG as source is mounted on a holder between them.

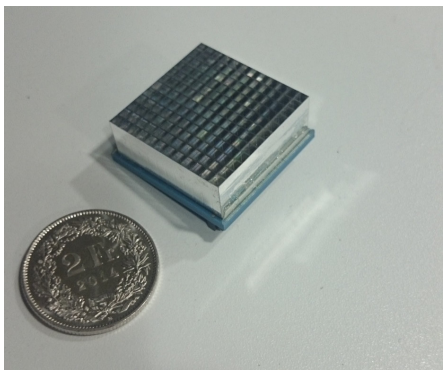

(b) Front side of LTCC module with crystals wrapped in reflective foil.

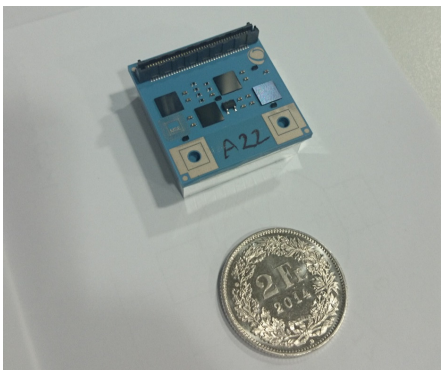

(c) Back side of LTCC module with four PETA ASICs and connection holes for water cooling (not used).

Figure 47: Pictures from the setup of the PETA high-rate test.

The setup for the test was brought from Mannheim and is shown in figure 47. PETA LTCC modules are mounted face-to-face for a coincidence measurement. They each host four PETA4 ASICs on one side and

2 The measurements were done in Zurich together with Prof. Peter Fischer and Dr. Ilaria Sacco, University of Heidelberg, Institute of Computer Engineering, Mannheim, Germany, whom I would like to thank explictly for providing the complete setup, their support, and the raw data.

12×12 Fondazione Bruno Kessler (FBK) SiPMs of $2.25\,\mathrm{mm} \times 2.25\,\mathrm{mm}$ size as well as 12×12 LYSO crystals of $2.25\,\mathrm{mm} \times 2.25\,\mathrm{mm} \times 10\,\mathrm{mm}$ size on the other side. The specifications of the SiPMs are the same as for the commercial AdvanSiD RGB sensors. Individual crystals are separated by three layers of reflective foil (ESR, aluminum, ESR) to ensure minimal optical cross-talk and resulting in a crystal pitch of 2.5 mm. The modules foresee a water cooling connection, which is however not used in this test. Mounted on the carrier board, the face-to-face distance is 11 cm. Using this distance and the crystal front face area, the effective SAFIR-equivalent activity for the PETA setup A_{PETA} is calculated from the SAFIR target activity $A_{\mathrm{SAFIR}} = 500\,\mathrm{MBq}$ to be

$$A_{\mathrm{PETA}} = A_{\mathrm{SAFIR}} \cdot \frac{(2.1\,\mathrm{mm})^2}{(2.25\,\mathrm{mm})^2} \cdot \frac{(55\,\mathrm{mm})^2}{(68.75\,\mathrm{mm})^2} \cdot \frac{1 - e^{-12/11.3}}{1 - e^{-10/11.3}} = 311\,\mathrm{MBq}, \tag{45}$$

which results in the same single channel rate in this setup as A_{SAFIR} would in the SAFIR reference design. A syringe filled with ^{18}F-FDG is placed between the modules and acts as a source of positrons, which annihilate to yield pairs of back-to-back gammas, which are recorded using the modules.

Only the data of one PETA per LTCC is recorded to not be limited by the USB connection bandwidth used for the readout of the setup. Furthermore, the data transmission was stopped when the FPGA first in first out (FIFO) buffer was almost full to ensure having continuous time slices of data.

The data were analyzed using ATOM with a dedicated event reader input class. A fit to the photo-peak was applied to the energy spectrum to select only events from within $\pm 1\sigma$ of the peak. In lack of an absolute calibration, this value is not converted to SI units. After sorting the hits into coincidences, the resulting distribution was fitted with a Gaussian to obtain the CRT and its errors from the fit parameters. No further corrections were applied to correct time-walk or fine counter bin width inequalities

An exemplary spectrum is shown in figure 48. The photo-peak is easily identified as well as the Compton edge and continuum. Towards the left-hand side, low energy noise hits occur, which are cut off by an energy threshold. The CRT of channel 56 with all other relevant channels on the other side is shown in figure 49 for a run with low activity. The values for all pairs which have more than 100 counts in the run with 438 MBq actual activity are shown in figure 50. Almost all values are better than 300 ps FWHM with the best pairs being slightly above 200 ps.

The highest activity obtained during the measurement campaign was 438 MBq, which is equivalent to a channel rate resulting from 705 MBq in the SAFIR reference design. The values are spread around

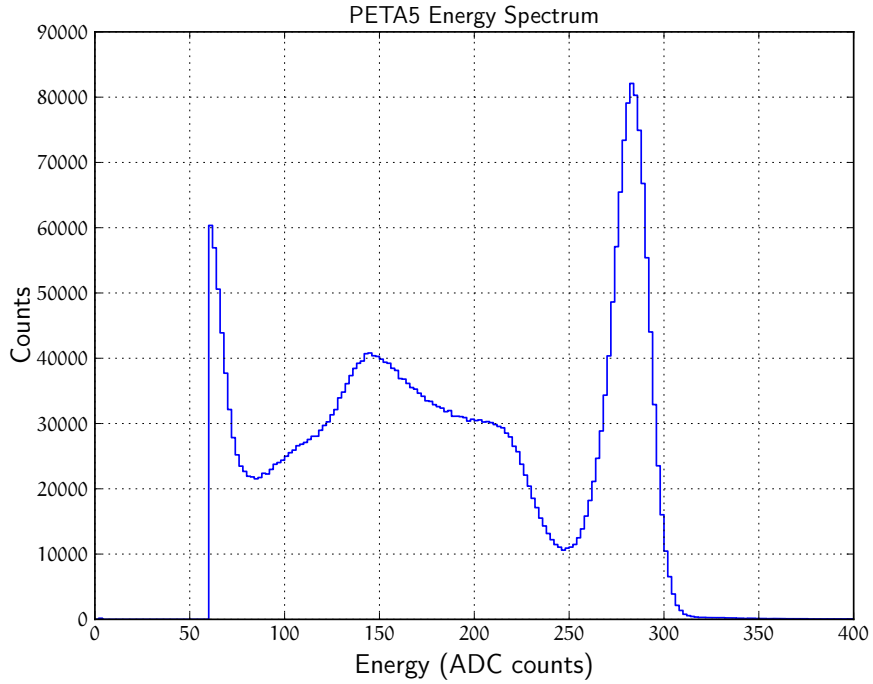

Figure 48: A full energy spectrum of one channel taken with the LTCC module during the high-rate test at a run with low activity on the second day. The photo-peak and the Compton edge can be identified and no other peaks are present except for low energy noise at the left edge as expected for the ^{18}F tracer.

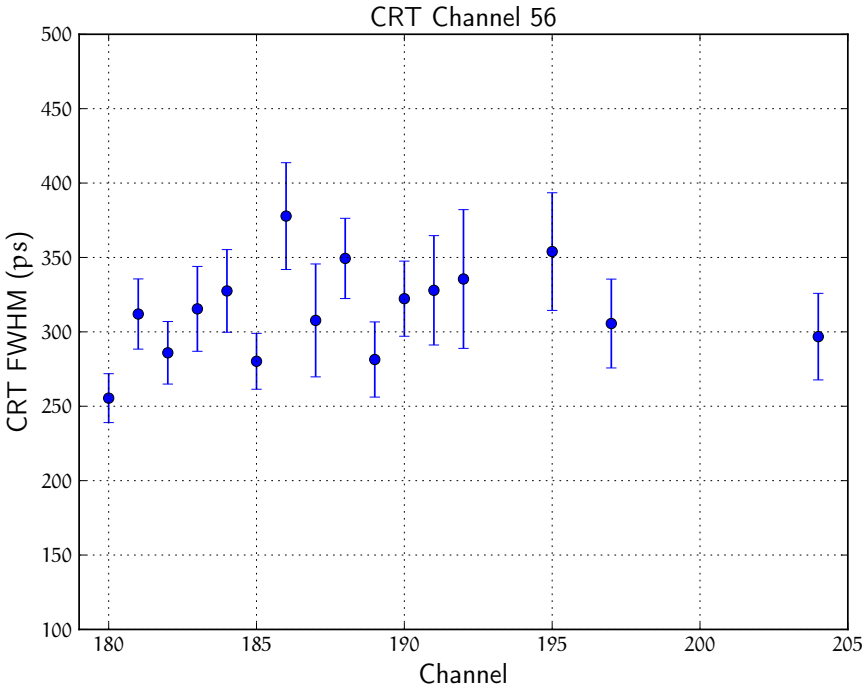

Figure 49: CRT of one channel with all other possible channels at 438 MBq activity. Shown are the fitted σ value as point and the fit error as bars.

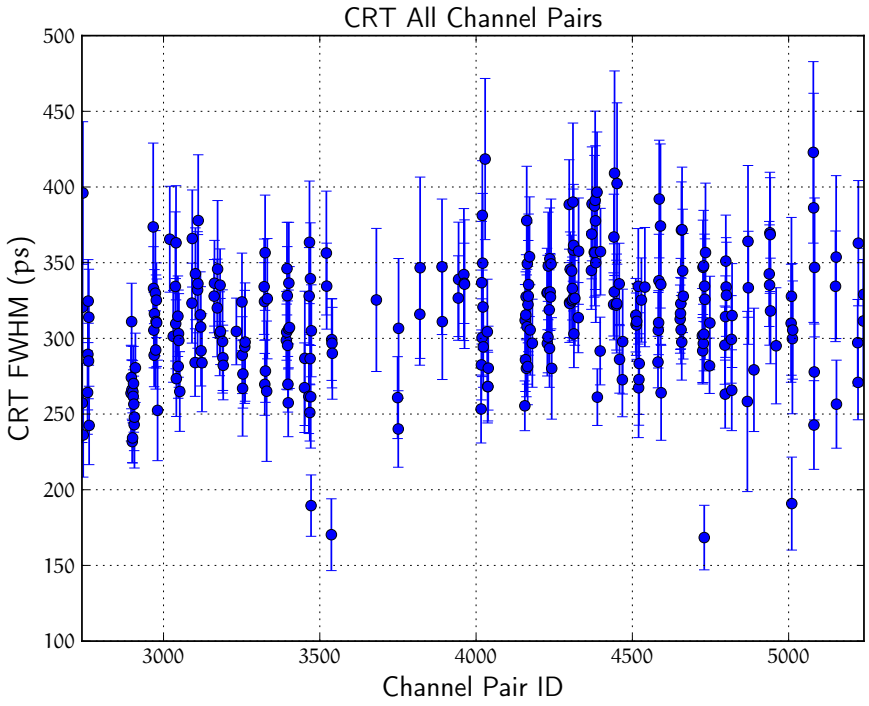

Figure 50: Shown are all CRT values including all pairs having at least 100 coincidence events at 438 MBq activity.

300 ps FWHM in a band between 200 ps and 400 ps. The effect of the activity on the CRT is summarized in figure 51.

No significant effect is found in the relevant activity region up to 500 MBq, corresponding to a single channel rate in a SAFIR scanner exposed to 805 MBq. All values are around 300 ps FWHM with a very faint increase towards higher activities.

In figure 52 the measured mean channel rate is plotted against the activity. The time differences of hits originating from a Poisson process are distributed following an exponential distribution, whose parameter in the exponent is proportional to the mean rate. This fact can be used to measure the rate even when time slices are missing as long as the time structure is preserved within the available slices. The rates in the figure were extracted from the data by fitting an exponential to the time differences of subsequent hits. As described, this is to avoid counting problems when losing parts of the data due to DAQ bandwidth limitations. The points indicate the mean of all channels and the error bars their standard deviation around that mean. Without losses, the relationship should be linear, which is the case for the first points. At the SAFIR equivalent activity, approximately 10 % of the data is lost due to dead time. The fit results indicate an effective dead time of 13.3 µs. Newer versions of the PETA reduce this loss by introducing another buffer to further de-randomize arrival times of the hits. In addition, they have a readout mode, where channels without hit only need one bit in the data stream compared to the full set

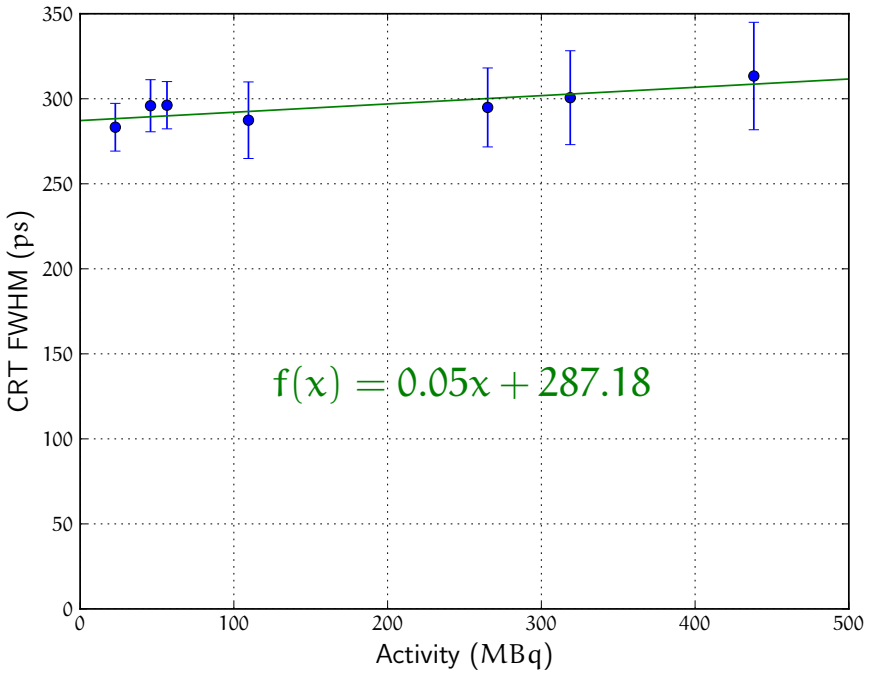

Figure 51: The CRT (mean value as points and the standard deviation between channel pairs as error bars) are shown as a function of activity. A linear fit is applied to the values.

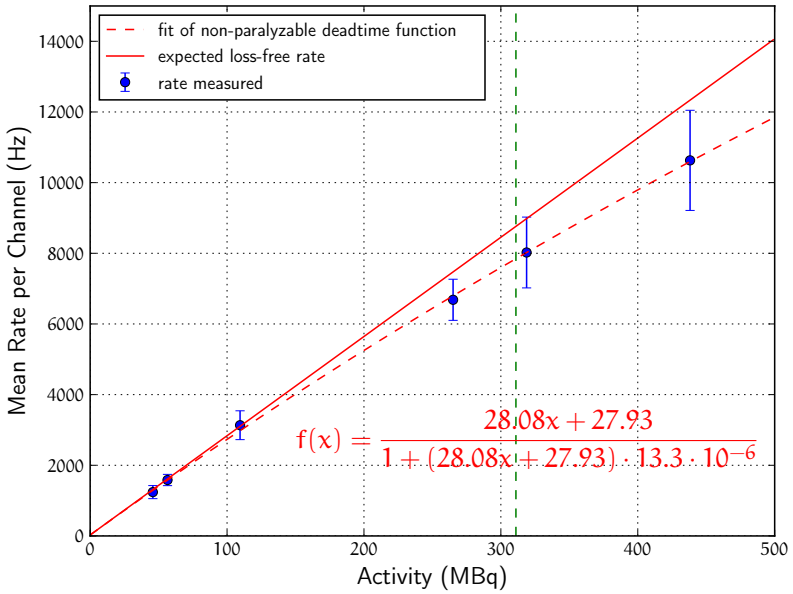

Figure 52: Measured mean channel rate as a function of activity. An extrapolating red line is added to the first three measured points to show the difference to the measurement. The fit of a dead-time model is plotted as dashed red line. Fit parameters and functions are given as red text. The SAFIR-equivalent activity is indicated by the dashed green line.

of bits read out for all channels at the moment. With PETA4, only one subsequent hit can be recorded in each channel before the previous has been read out. Combined with the random arrival time of the hits, these Poisson losses occur much earlier than anticipated from the average channel rate and duration of the pulses.

To conclude, the PETA ASIC shows good timing performance but also some dead time losses at the SAFIR-equivalent activity. This is improved in future versions of the ASIC promising much lower loss at the same activity. The timing performance is sufficient for the SAFIR goal of a CTW of a few hundred picoseconds length.

Part III

THE END

6 SUMMARY AND OUTLOOK

The SAFIR and BPET projects aim at very specific niches of PET technology. While SAFIR promises to deliver unprecedented temporal resolution in the preclinical sector, BPET will be the most cost-effective and application specific clinical PET scanner for imaging the human brain. Attached to these goals are very different demands to the system design. SAFIR requires an excellent CRT to limit the number of random coincidences. At the same time, the electronics have to deal with a very high rate of hits per channel. All components inside the MRI scanner have to work in a strong 7 T magnetic field and have to have very low EMI emission to not degrade the MRI performance. BPET, on the other hand, is designed to operate with a limited number of photons reaching the photo-sensor. To reduce the cost further, short crystals of $8\,\mathrm{mm} \times 8\,\mathrm{mm} \times 10\,\mathrm{mm}$ size are used.

The high count rate capability of SAFIR is reflected in the simulated NECR curve, which has not reached its peak at the target activity of 500 MBq. The absolute value of the NECR is as high as 29.5 Mcps at that activity, which is unprecedented in preclinical PET. Furthermore, this allows very short acquisition time frames to enable a temporal resolution of the order of a few seconds. The spatial resolution of the SAFIR reference design is estimated to be slightly better than 2 mm FWHM in the center. It degrades to roughly 4 mm in the radial direction when moving the source radially outward to 50 mm offset. When intercrystal scattered events are recovered, this is also true for the tangential direction. In all cases, the axial resolution is constant being slightly worse than 3 mm FWHM due to the full set of ring differences used for the reconstruction. The sensitivity of the reference design with a very short coincidence window of 400 ps and the recovery of intercrystal scattered events reaches 7.69 % at the peak and is 6.56 % averaged over the standardized NEMA mouse. The sensitivity value can be further increased using a longer coincidence window. Comparing different prototype geometries, the one closest to the reference design performs the best overall with respect to sensitivity. The peak value exceeds 10 %, which is more than the reference design. It has to be noted that the values can only be compared to limited extend because a different simulation framework and a different source isotope were used. A Derenzo phantom simulation shows that balls diameters as small as 1.6 mm can be resolved when there is no background using iterative algorithms.

For BPET, GATE simulations have shown a system sensitivity of 1.61 cps/kBq. The spatial resolution is as good as 6.07 mm FWHM in

the position ($x = 100\,mm, z = 0\,mm$). In the worst case, the resolution is around 10 mm FWHM, still satisfying the design goal.

A high-rate test with the PETA ASIC has shown promising results with respect to CRT and data loss at high rates. Using the previous version of the ASIC without derandomization of hits and a limited read-out rate, only around 10 % of the data was lost at the target activity. This will be improved in the current version of the ASIC. The CRT averages at 300 ps FWHM with a very faint and negligible rate dependence. This might also be improved in the current ASIC version.

Measurements with a BPET-like sensor arrangement with a limited number of photons reaching the sensor show the feasibility of such a geometry. A CRT of better than 400 ps was obtained with Hamamatsu and AdvanSiD sensors enabling a coincidence window of a few nanoseconds length. Devices from the other manufacturers Ketek and SensL are slightly worse but perform well enough to be used in the BPET scanner.

Compatibility measurements of components have shown the feasibility of using the Avago AFBR-57R5APZ SFP module inside the MRI scanner. Neither was it disturbed by the strong magnetic field nor did it significantly influence the MRI performance. The same is true for the shielded CERN FEASTMP_CLP DC-DC buck converter modules. In search for a commercially available alternative, first prototypes of custom buck converter modules were developed and tested. These module were functional inside the MRI scanner as well. However, they degraded the MRI SNR to an unacceptable level. Custom power conversion module development is an ongoing activity in the SAFIR collaboration and will be pursued further motivitated by the working examples of converters developed by Satish Dhawan of Yale university and the CERN modules.

Next steps for SAFIR are the testing of the PETA prototype featuring the SDIP board and an LTCC module, which will be done in the coming months. It will be accompanied by the refinement of the custom buck converters. Moreover, custom PCB PETA modules are developed to replace the LTCC modules. With the prototypes in hand, a cooling system is developed to extract up to 1.5 kW of power from the detector volume.

BPET will be developed into a full prototype system by the author and a collegue in the course of an ETH Pioneer Fellowship. Electronics to read out PETA ASICs will be developed, tested, and assembled using a suitable mechanical structure to have a prototype working within one year. At the same time, simulations will be refined and extended to obtain more realisitic data for the use case to further guide the development.

Part IV

APPENDIX

A

MATHEMATICAL BACKGROUND FOR IMAGE RECONSTRUCTION

A.1 FILTERED BACK PROJECTION

Analytic image reconstruction with FBP makes use of the projection-slice theorem. In this section, the most important steps towards the FBP algorithm are stated following chapter 6 of [28] with some adjustments for the application to PET. The projection-slice theorem states that the two-dimensional Fourier transform $\mathcal{F}$ of a function λ evaluated on a line with diretion ω through the origin is equivalent to the Fourier transform with respect to the first variable of the Radon transformed function λ:

$$(\mathcal{F}\lambda)(\sigma,\omega) = \frac{1}{\sqrt{2\pi}}(\mathcal{F}(\mathcal{R}\lambda))(\sigma,\omega).$$

This can be used to find an inverse to the Radon transform, which can be expressed as

$$\mathcal{R}^{-1} = \frac{1}{4\pi}\mathcal{R}^{\#}I^{1},$$

where I^1 is the Riesz potential defined by

$$\mathcal{F}(I^1 g)(\sigma,\omega) = |\sigma|\mathcal{F}g(\sigma,\omega),$$

where g is some function and $\mathcal{R}^{\#}$ is the back projection, which is the adjunct operator to $\mathcal{R}$, i.e.

$$\mathcal{R}^{\#}q(x) = \int_0^{2\pi} q\left(\langle x,\omega\rangle,\omega\right)\mathrm{d}\phi,$$

for some function $q(s,\omega)$. It is called back projection because it defines a continuation of a function on a line in $\mathcal{R}^2$ onto all of $\mathcal{R}^2$: For a fixed ω, the function $q\left(\langle x,\omega\rangle,\omega\right)$ is defined on all of $\mathcal{R}^2$ and constant on all lines perpendicular to ω. The integration over ω yields the average over all lines through the point x. It can be seen that the back projection amplifies high frequencies through the factor $|\sigma|$. This factor is sometimes referred to as ramp filter. Furthermore, these high frequencies carry a large uncertainty resulting in an extreme amplification of these uncertainties. To find a proper reconstruction algorithm, a filter is to be employed. A common choice is the Shepp-Logan filter

$$F_\gamma(\sigma) = \begin{cases} \operatorname{sinc}\frac{\sigma\pi}{2\gamma}, & \text{for } |\sigma| \leqslant \gamma \\ 0 & \text{for } |\sigma| > \gamma. \end{cases} \tag{46}$$

The convolution filter is then

$$e_\gamma(s) = \frac{1}{8\pi^2}\int_{\mathbb{R}} |\sigma| F_\gamma(\sigma) e^{is\sigma} d\sigma \tag{47}$$

$$= \frac{\gamma^2}{2\pi^3}\frac{\frac{\pi}{2} - \gamma s \sin \gamma s}{\left(\frac{\pi}{2}\right)^2 - \gamma^2 s^2}. \tag{48}$$

If the use of a filter purges the influence of high frequencies $|\xi| > p$, the Fourier transform of the resulting function will have a compact support with radius p, i.e. it will have a limited bandwidth p. Using the Nyquist-Shannon sampling theorem [30, 31], it can be concluded that only details greater than the resolution $\frac{2\pi}{p}$ are included in such functions. In other words, the sampling distance h has to fulfill the inequality

$$h \leqslant \frac{\pi}{p}.$$

Given p directions, $2q+1$ samples have to be taken to resolve the interval $[-1,1]$, where $q = \frac{1}{h} \approx \frac{p}{\pi}$. In the following, an equidistant sampling is assumed, i.e. a measurement of $(\mathcal{R}\lambda)(s_l, \omega_j)$, where

$$\omega_j = \omega(\phi_j),\ \phi_j = (j-1)\frac{\pi}{p},\ j = 1,\dots,p \tag{49}$$

$$s_l = lh,\ l = -q,\dots,q,\ h = \frac{1}{q}. \tag{50}$$

The integral of the back projection is discretized as

$$\int_0^{2\pi} h(\phi) d\phi \to \frac{2\pi}{p}\sum_{j=1}^{p} h(\phi_j).$$

With $\gamma = \frac{\pi}{h}$ the convolution filter becomes

$$e_\gamma(s_l) = \frac{\gamma^2}{\pi^4}\frac{1}{1-4l^2}.$$

The complete FBP algorithm is:

1. For all $j = 1,\dots,p$ calculate the convolution of the filter with the measurements

$$\Psi_{j,k} = h\sum_{l=-q}^{q} e_\gamma(s_k - s_l)\mathcal{R}\lambda(s_l, \omega_j),\ k = -q,\dots,q.$$

2. For every coordinate $x \in \mathbb{R}^2$ calculate the discrete back projection

$$\tilde{\lambda}(x) = \frac{2\pi}{p}\sum_{j=1}^{p}((1-\eta)\Psi_{j,k} + \eta\Psi_{j,k+1}),$$

where k, η are such that $s = \langle x, \omega_j\rangle$, $k \leqslant \frac{s}{h} < k+1$, $\eta = \frac{s}{h} - k$ is fulfilled.

A.2 MAXIMUM LIKELIHOOD AND EXPECTATION MAXIMIZATION

In section 2.5.3, the likelihood function

$$L(\vec{\lambda}) := p(\vec{y}|\vec{\bar{y}}) = \prod_{i=1}^{I} p(y_i|\bar{y}_i) = \prod_{i=1}^{I} e^{-\bar{y}_i} \frac{\bar{y}_i^{y_i}}{y_i!}, \tag{51}$$

$$\log L(\vec{\lambda}) = \sum_{i=1}^{I} \left[y_i \log \bar{y}_i - \bar{y}_i - \log y_i! \right], \tag{52}$$

and its maximizing condition

$$\frac{\partial(\log L(\vec{\lambda}))}{\partial \lambda_j} = \sum_{i=1}^{I} \left[\frac{y_i}{\bar{y}_i} - 1 \right] \frac{\partial \bar{y}_i}{\partial \lambda_j} = 0$$

were introduced, where $\vec{\lambda}$ is the unknown tracer distribution, $\vec{y}$ is the measured count rate in the LORs, $\vec{\bar{y}}$ is the count rate estimated from the tracer distribution, and I is the number of LORs. This section will explain how to arrive at an iterative algorithm to find the image maximizing the likelihood function using the EM method proposed by Dempster et al. [68] and first applied to emission tomography by [33]. Further insight can be gained from [69, 70].

The EM algorithm was designed to be used when the complete data set cannot be observed. This is the case in emission tomography, where the projection data, which are a function of the tracer distribution, are measured but a direct measurement for the original distribution is not available. To use the EM algorithm, the distribution of a complete set of data is defined. There are potentially several ways to define a complete set of data.

With the distribution of the chosen complete data set, the conditional expectation value of this distribution is calculated ("expectation step") given the current estimate of the unknown distribution. In the second ("maximization") step, the expectation value found in the expectation step is maximized.

In the case of emission tomography, a suitable choice of the complete data is the number n_{ij} of counts originating from voxel j and detected in LOR i. This is distributed according to a multivariate Poisson distribution

$$L_{comp}(\vec{z}|\vec{\lambda}) = \prod_{i=1}^{I} \prod_{j=1}^{J} \frac{(a_{ij}\lambda_j)^{n_{ij}}}{n_{ij}!} e^{-a_{ij}\lambda_j}, \tag{53}$$

$$\log L_{comp}(\vec{z}|\vec{\lambda}) = \sum_{i=1}^{I} \sum_{j=1}^{J} n_{ij} \log(a_{ij}\lambda_j) - a_{ij}\lambda_j - \log n_{ij}! \tag{54}$$

where $\vec{z}$ is the complete data vector distributed according to this Poisson distribution, and J is the number of voxels. It can easily be

seen that (54) reduces to (52) when the sum over j is evaluated with $\sum_{j=1}^{J} a_{ij}\lambda_j = \bar{y}_i$ and $\sum_{j=1}^{J} n_{ij} = y_i$.

For the expectation step, the conditional expectation value $Q(\vec{\lambda}|\vec{\lambda}^k, \vec{y})$ of this log-likelihood function, i.e. the expectation value given the current estimate $\vec{\lambda}^k$ and the measurement $\vec{y}$ is calculated. Omitting constant terms with respect to $\vec{\lambda}$, the following expression is obtained

$$Q(\vec{\lambda}|\vec{\lambda}^k) = E\left[\log L_{comp}(\vec{z}) \,\middle|\, \vec{\lambda}^k, \vec{y}\right] \tag{55}$$

$$= \sum_{i=1}^{I}\sum_{j=1}^{J} y_i \frac{a_{ij}\lambda_j^k}{\bar{y}_i^k} \log(a_{ij}\lambda_j) - a_{ij}\lambda_j \tag{56}$$

$$= \sum_{j=1}^{J}\left(\sum_{i=1}^{I} a_{ij}\frac{y_i}{\bar{y}_i^k}\right)\lambda_j^k \log\left[\left(\sum_{i=1}^{I} a_{ij}\right)\lambda_j\right] - \left(\sum_{i=1}^{I} a_{ij}\right)\lambda_j. \tag{57}$$

It was used in the second step, that the conditionally expected value of the complete data set is

$$E\left[n_{ij} \,\middle|\, \vec{\lambda}^k, \vec{y}\right] = y_i \frac{a_{ij}\lambda_j^k}{\bar{y}_i^k}. \tag{58}$$

The numerator in the fraction is the expected counts from voxel j detected in LOR i given the current estimate λ_j^k. Dividing by the expected total number of counts in that LOR and multiplying with the actually measured counts in the same LOR yields the conditionally expected value. Note that in (57) the current estimate of the tracer distribution $\vec{\lambda}^k$ as well as the unknown distribution $\vec{\lambda}$ appear. This is used in the maximization step, which maximizes this expression to obtain the optimal value of the next estimation

$$\vec{\lambda}^{k+1} = \arg\max_{\vec{\lambda}} Q(\vec{\lambda}|\vec{\lambda}^k). \tag{59}$$

In the case of PET, the maximum can be found by taking the derivative with respect to λ_j, justifying the previous omission of constant terms. This yields a single algebraic expression for the complete MLEM algorithm

$$\left.\frac{\partial Q(\vec{\lambda}|\vec{\lambda}^k)}{\partial \lambda_j}\right|_{\lambda_j=\lambda_j^{k+1}} = \left(\sum_{i=1}^{I} a_{ij}\frac{y_i}{\bar{y}_i^k}\right)\lambda_j^k \frac{1}{\lambda_j^{k+1}} - \sum_{i=1}^{I} a_{ij} \stackrel{!}{=} 0 \tag{60}$$

$$\Rightarrow \lambda_j^{k+1} = \frac{\lambda_j^k}{\sum_{i=1}^{I} a_{ij}} \sum_{i=1}^{I} a_{ij}\frac{y_i}{\bar{y}_i^k}, \tag{61}$$

which is equation (24).

B

TECHNICAL DOCUMENTS

B.1 MECHANICAL DRAWINGS

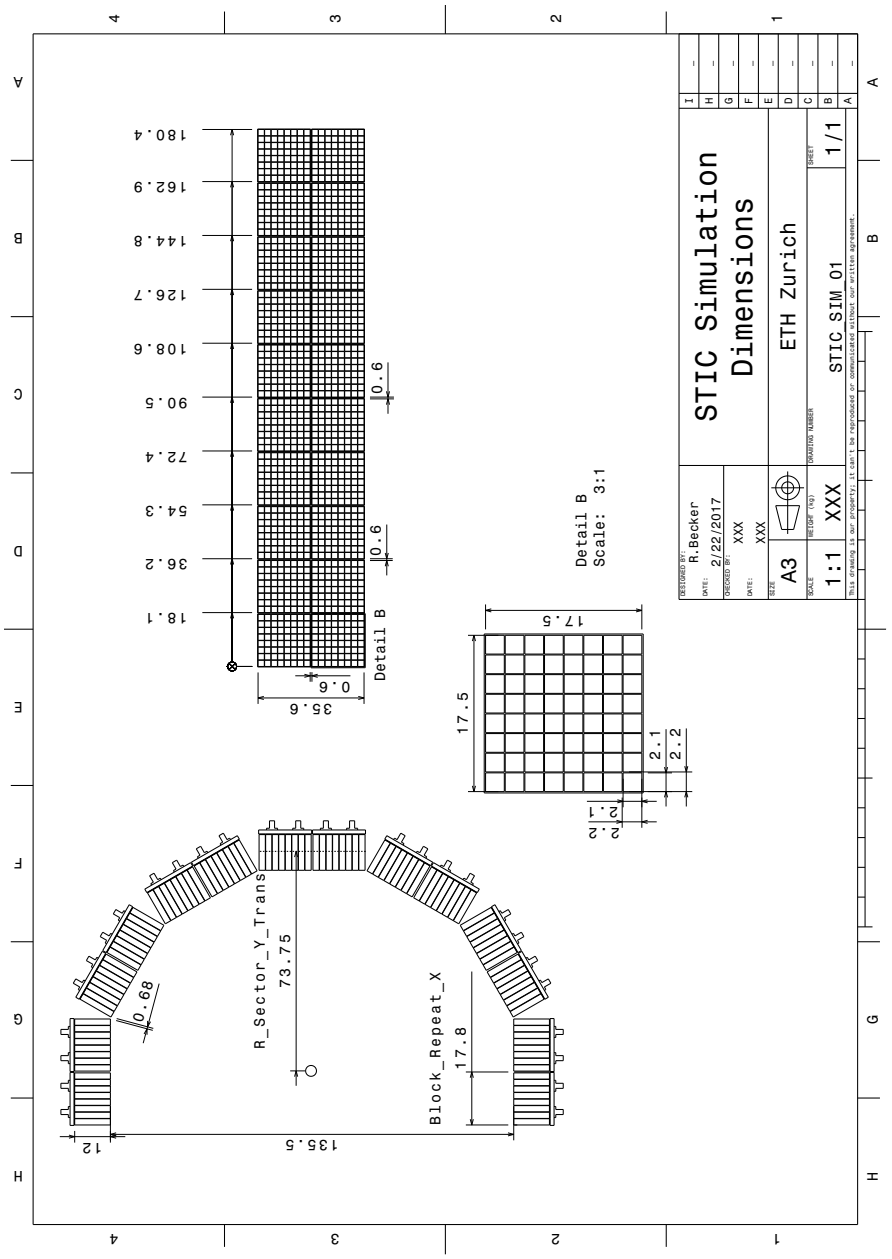

Figure 53: Dimensions for the GATE simulation for the STiC prototype.

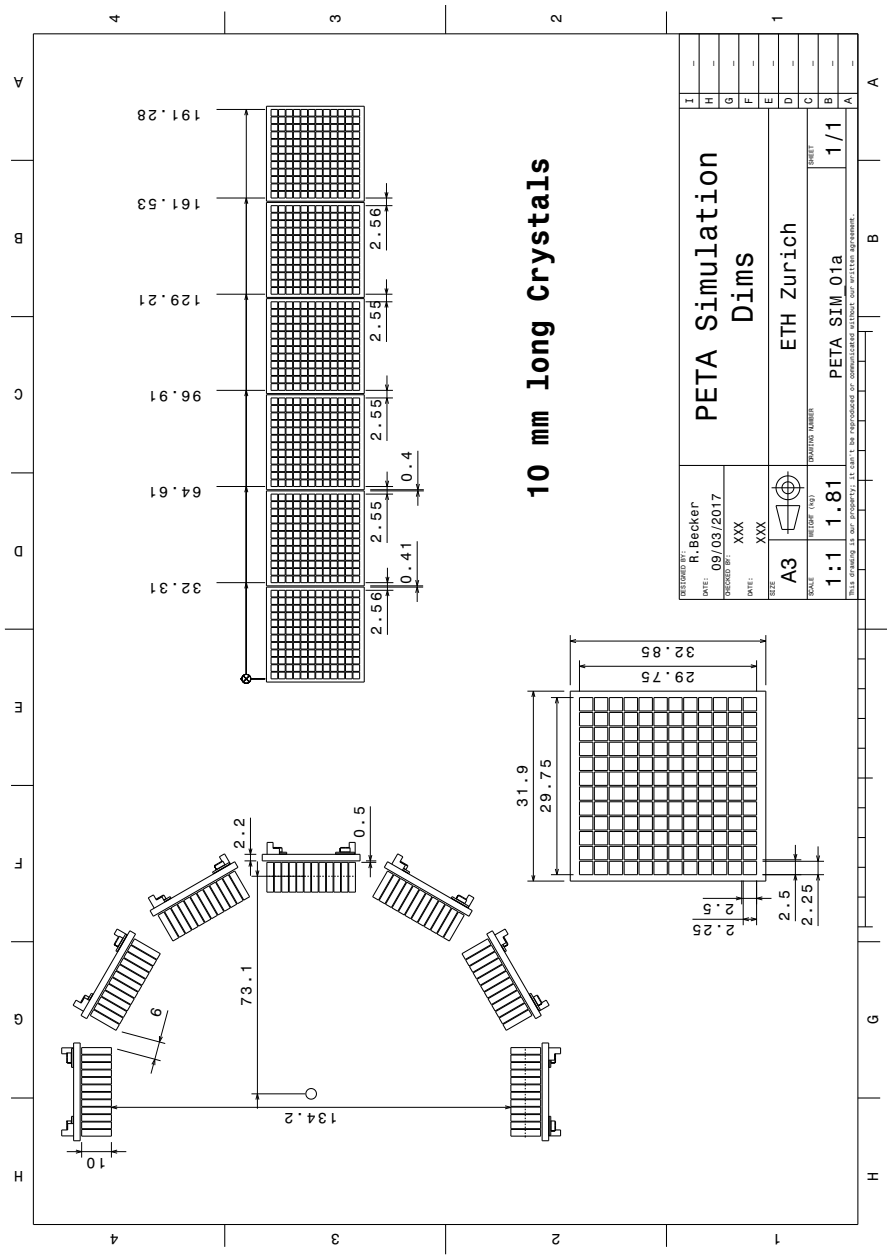

Figure 54: Dimensions for the GATE simulation of the PETA prototype with 10 mm crystal length.

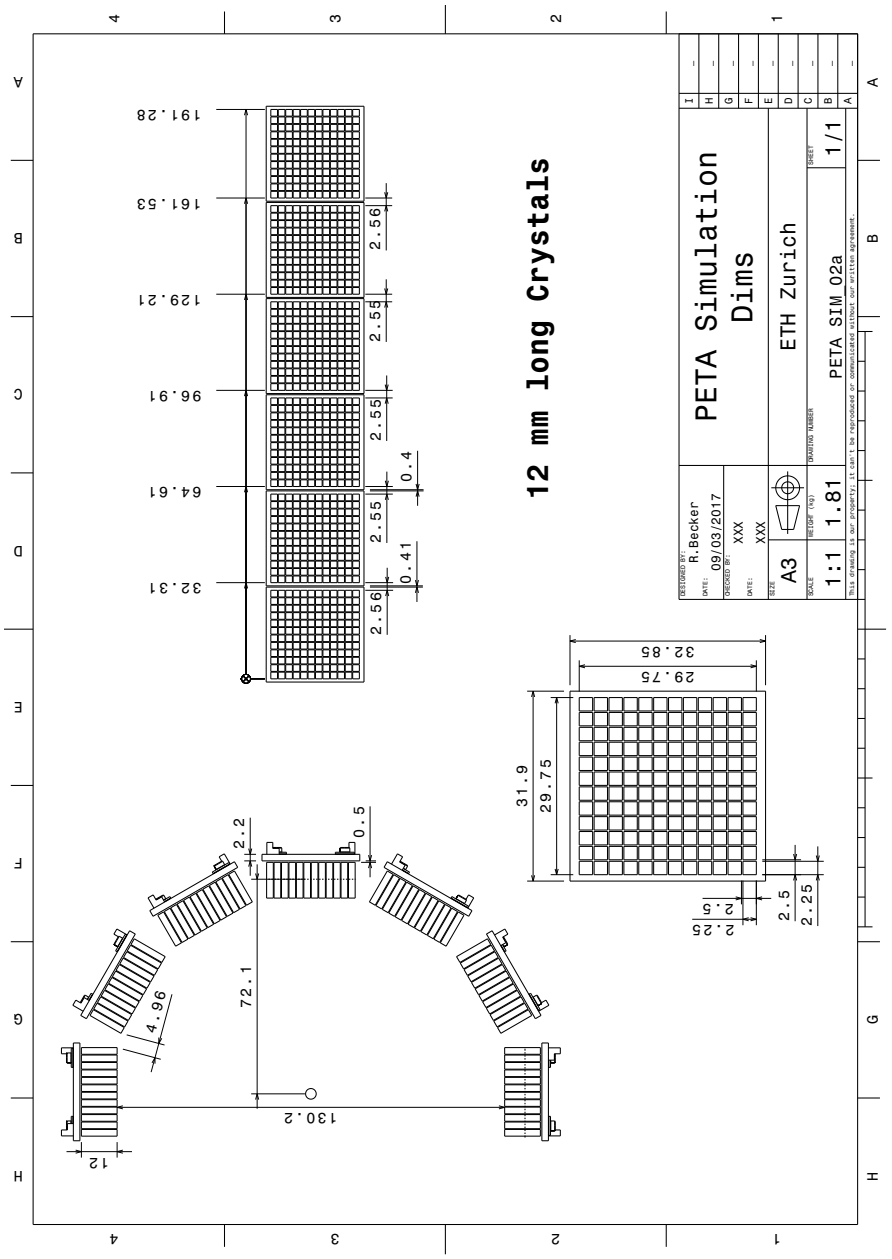

Figure 55: Dimensions for the GATE simulation of the PETA prototype with 12 mm crystal length.

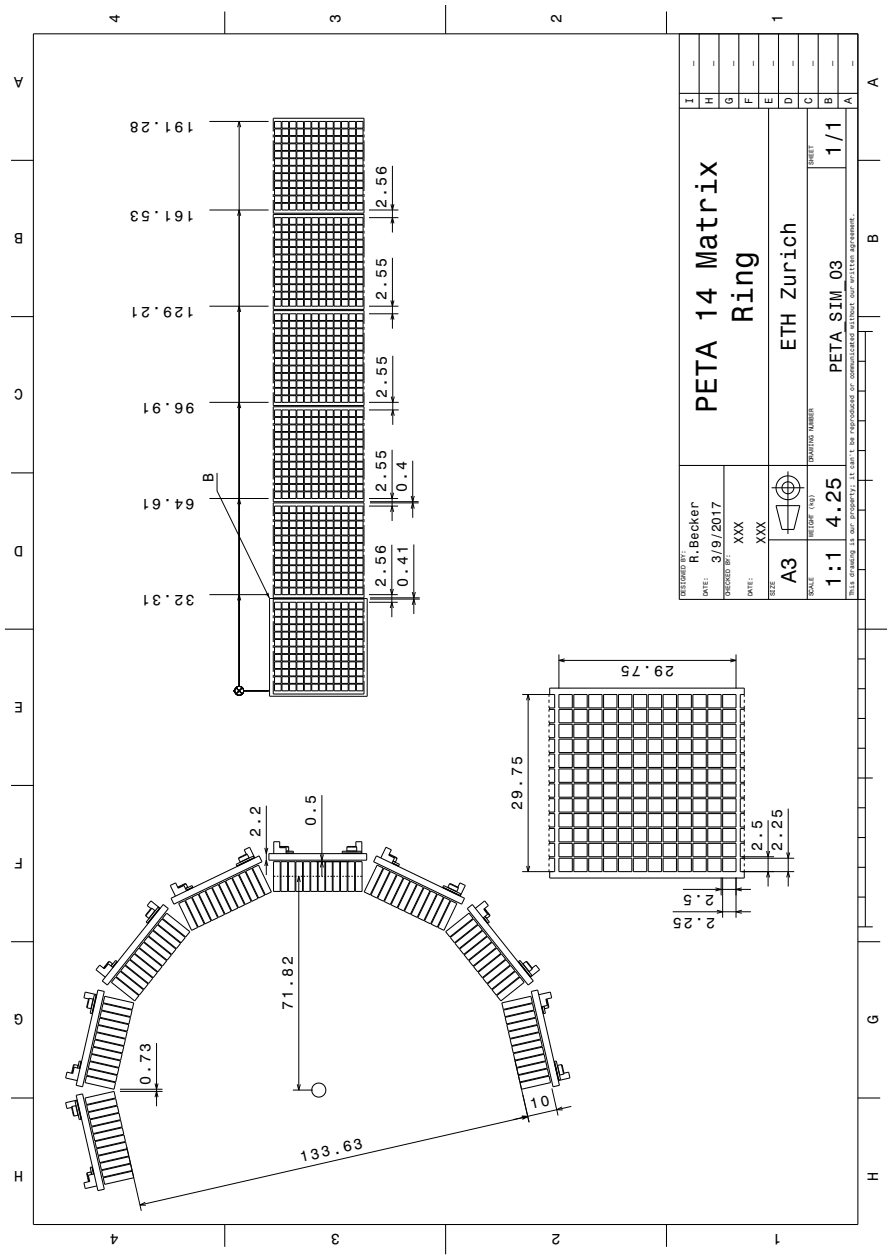

Figure 56: Dimensions for the GATE simulation of the PETA prototype with 10 mm crystal length and 14 sectors.

B.2 ELECTRONICS SCHEMATICS

B.2.1 *SDIP*

On the following pages, the schematics of the SDIP are printed, which I have developed with inspriration and advice from previous schematics for the PETA setup from Ilaria Sacco. The schematics was discussed with Ulf Röser and entered into Altium Designer by Lubomir Djambazov. The major interfaces are

1. Connections to the three PETA LTCC modules (J9_1-J9_3 on sheet 9);
2. Connections to the SBT board (WT1, WT2, WT2V, WB1, WB2 on sheet 1);
3. 12 V power input (WB5 on sheet 1);
4. Optical link SFP connector (J4_5 on sheet 4);
5. A pin header for use as debug signals (J3_1 on sheet 3) with 2.5 V logic levels;
6. Two coax U.FL connectors (J1_0, J1_1 on sheet 2) as high-speed reset input;
7. A Joint Task Action Group (JTAG) interface (sheet 6) for configuration of the FPGA and debugging;
8. Access to power the intermediate voltage rails to power them directly (B1-B4 on sheet 11) if DC-DC converters are not used.

The central functional element is the FPGA as IC1, whose connections are on sheets 2-6. Direct dependents are the three memory components: the DDR2 RAM IC01 connected to bank 16, the EEPROM IC2 (sheet 6), and the serial configuration flash IC4 (sheet 6). The complementary metal-oxide-semiconductor (CMOS) single-ended connections on a 1.8 V level to the modules are grouped on bank 14. The LVDS connections for the fast signals to the modules are realized on banks 15, 34, and 35. The serial interface to the SBT and the I2C interface to the SFP module (with level translation to 3.3 V, sheet 4) are connected to bank 15. Linear regulators as well as a power sequencing logic to ensure the correct timing for power-on and power-off are placed on sheets 7 and 8. The clocking circuitry to provide the reference clocks to the modules, the FPGA clock, and the reference clock for the gigabit transceivers is displayed on sheet 10. Sheet 11 hosts the connectors to plug DC-DC converters to provide the intermediate voltages given the 12 V input voltage.

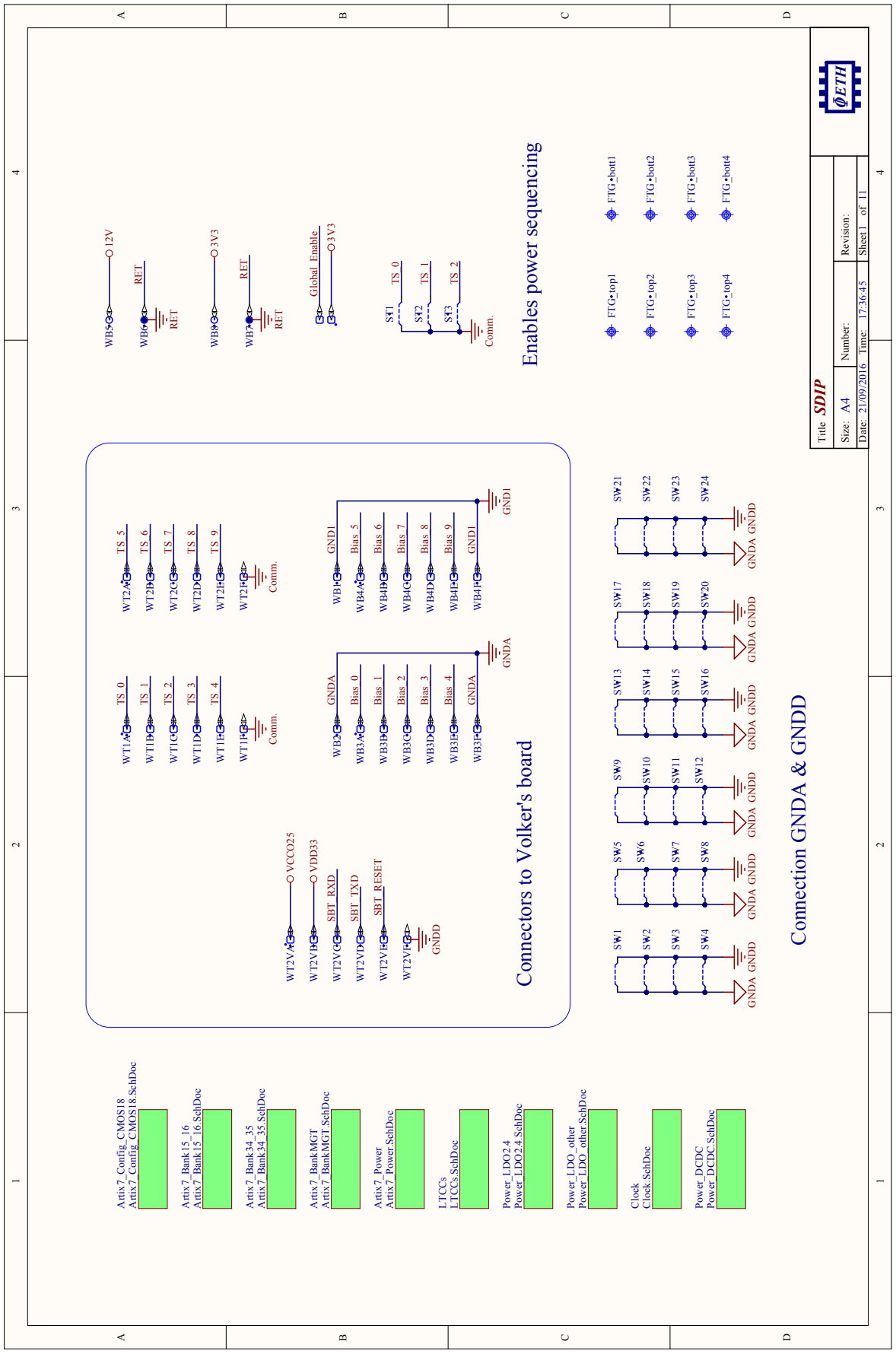
Artix7_Config_CMOS18
Artix7_Config_CMOS18.SchDoc
Artix7_Bank15_16
Artix7_Bank15_16.SchDoc
Artix7_Bank34_35
Artix7_Bank34_35.SchDoc
Artix7_BankMGT
Artix7_BankMGT.SchDoc
Artix7_Power
Artix7_Power.SchDoc
LTCCs
LTCCs.SchDoc
Power_LDO2.4
Power_LDO2.4.SchDoc
Power_LDO_other
Power_LDO_other.SchDoc
Clock
Clock.SchDoc
Power_DCDC
Power_DCDC.SchDoc
Connectors to Volker's board
Connection GNDA & GNDD
Enables power sequencing
Title SDIP
Size: A4
Number:
Revision:
Date: 21/09/2016
Time: 17:36:45
Sheet 1 of 11
ETH

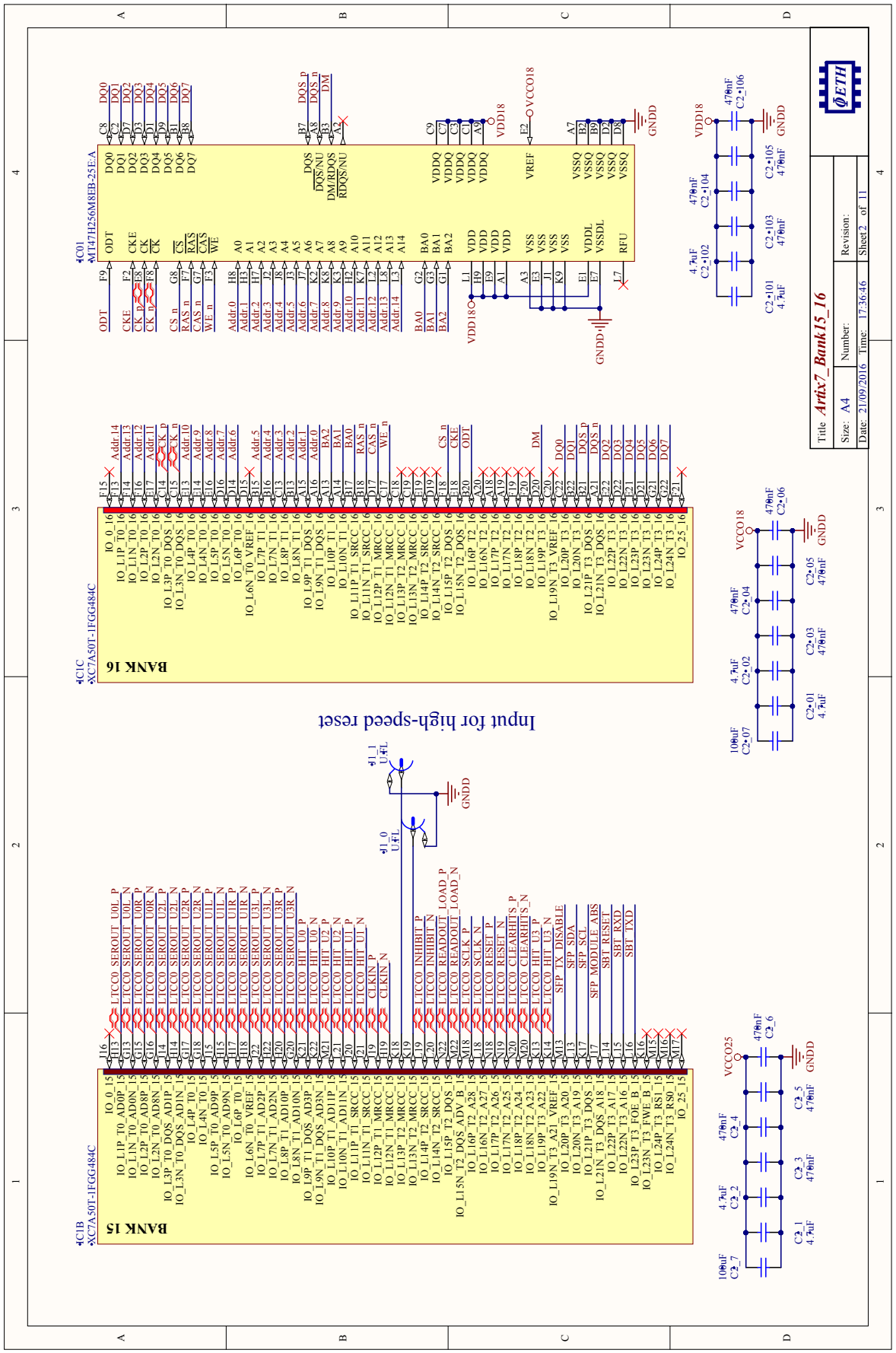
Input for high-speed reset
BANK 15
BANK 16
Title Artix7_Bank15_16
Size: A4
Number:
Revision:
Date: 21/09/2016
Time: 17:36:46
Sheet 2 of 11

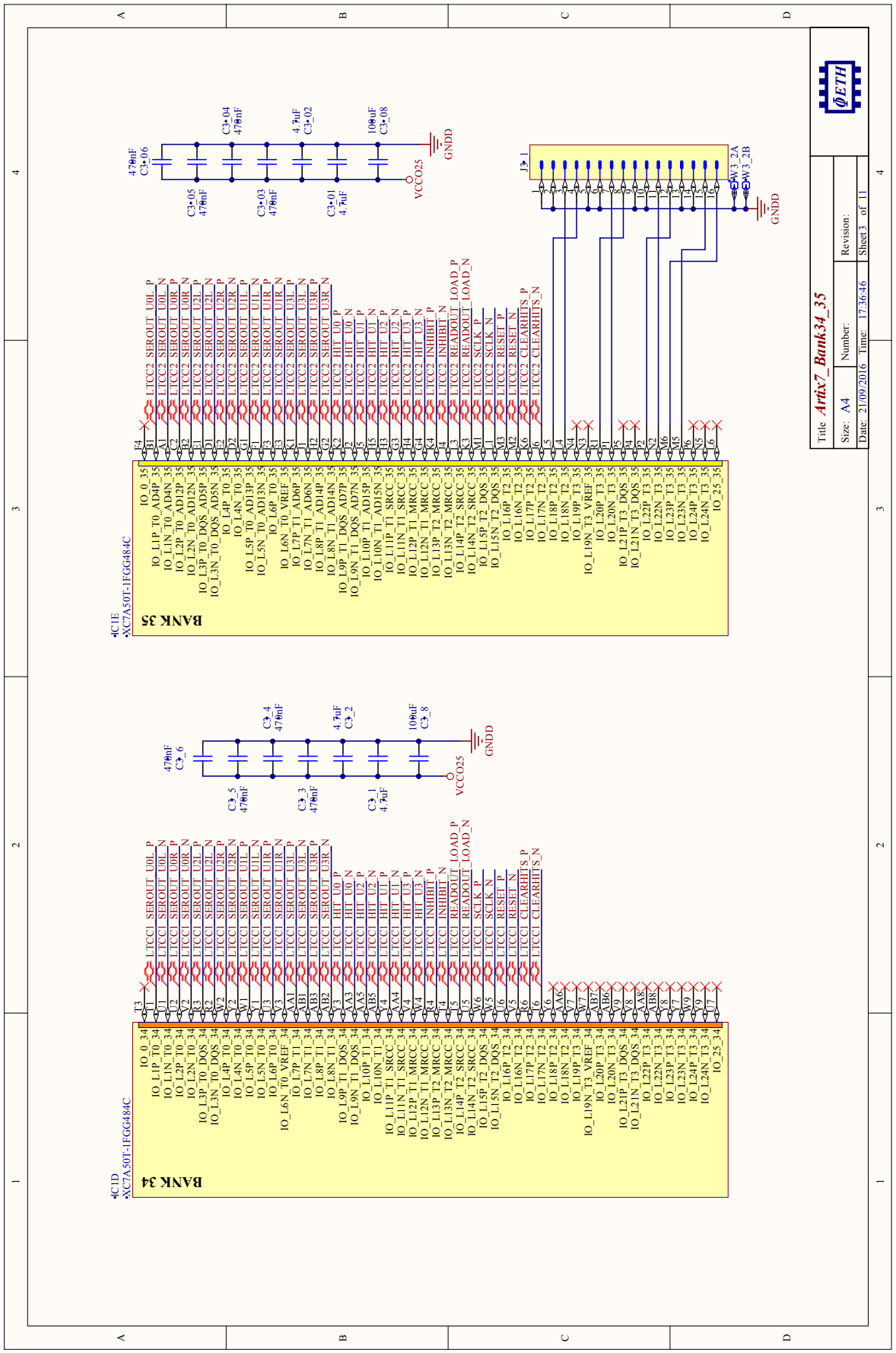
Title Artix7_Bank34_35
Size: A4
Number:
Revision:
Date: 21/09/2016
Time: 17:36:46
Sheet 3 of 11
ETH
BANK 34
BANK 35
XC7A50T-1FGG484C
GNDD
VCCO25
LTCC1_SEROUT_U0L_P
LTCC1_SEROUT_U0L_N
LTCC1_SEROUT_U0R_P
LTCC1_SEROUT_U0R_N
LTCC1_SEROUT_U2L_P
LTCC1_SEROUT_U2L_N
LTCC1_SEROUT_U2R_P
LTCC1_SEROUT_U2R_N
LTCC1_SEROUT_U1L_P
LTCC1_SEROUT_U1L_N
LTCC1_SEROUT_U1R_P
LTCC1_SEROUT_U1R_N
LTCC1_SEROUT_U3L_P
LTCC1_SEROUT_U3L_N
LTCC1_SEROUT_U3R_P
LTCC1_SEROUT_U3R_N
LTCC1_HIT_U0_P
LTCC1_HIT_U0_N
LTCC1_HIT_U2_P
LTCC1_HIT_U2_N
LTCC1_HIT_U1_P
LTCC1_HIT_U1_N
LTCC1_HIT_U3_P
LTCC1_HIT_U3_N
LTCC1_INHIBIT_P
LTCC1_INHIBIT_N
LTCC1_READOUT_LOAD_P
LTCC1_READOUT_LOAD_N
LTCC1_SCLK_P
LTCC1_SCLK_N
LTCC1_RESET_P
LTCC1_RESET_N
LTCC1_CLEARHITS_P
LTCC1_CLEARHITS_N
LTCC2_SEROUT_U0L_P
LTCC2_SEROUT_U0L_N
LTCC2_SEROUT_U0R_P
LTCC2_SEROUT_U0R_N
LTCC2_SEROUT_U2L_P
LTCC2_SEROUT_U2L_N
LTCC2_SEROUT_U2R_P
LTCC2_SEROUT_U2R_N
LTCC2_SEROUT_U1L_P
LTCC2_SEROUT_U1L_N
LTCC2_SEROUT_U1R_P
LTCC2_SEROUT_U1R_N
LTCC2_SEROUT_U3L_P
LTCC2_SEROUT_U3L_N
LTCC2_SEROUT_U3R_P
LTCC2_SEROUT_U3R_N
LTCC2_HIT_U0_P
LTCC2_HIT_U0_N
LTCC2_HIT_U1_P
LTCC2_HIT_U1_N
LTCC2_HIT_U2_P
LTCC2_HIT_U2_N
LTCC2_HIT_U3_P
LTCC2_HIT_U3_N
LTCC2_INHIBIT_P
LTCC2_INHIBIT_N
LTCC2_READOUT_LOAD_P
LTCC2_READOUT_LOAD_N
LTCC2_SCLK_P
LTCC2_SCLK_N
LTCC2_RESET_P
LTCC2_RESET_N
LTCC2_CLEARHITS_P
LTCC2_CLEARHITS_N
IO_0_34
IO_L1P_T0_34
IO_L1N_T0_34
IO_L2P_T0_34
IO_L2N_T0_34
IO_L3P_T0_DQS_34
IO_L3N_T0_DQS_34
IO_L4P_T0_34
IO_L4N_T0_34
IO_L5P_T0_34
IO_L5N_T0_34
IO_L6P_T0_34
IO_L6N_T0_VREF_34
IO_L7P_T1_34
IO_L7N_T1_34
IO_L8P_T1_34
IO_L8N_T1_34
IO_L9P_T1_DQS_34
IO_L9N_T1_DQS_34
IO_L10P_T1_34
IO_L10N_T1_34
IO_L11P_T1_SRCC_34
IO_L11N_T1_SRCC_34
IO_L12P_T1_MRCC_34
IO_L12N_T1_MRCC_34
IO_L13P_T2_MRCC_34
IO_L13N_T2_MRCC_34
IO_L14P_T2_SRCC_34
IO_L14N_T2_SRCC_34
IO_L15P_T2_DQS_34
IO_L15N_T2_DQS_34
IO_L16P_T2_34
IO_L16N_T2_34
IO_L17P_T2_34
IO_L17N_T2_34
IO_L18P_T2_34
IO_L18N_T2_34
IO_L19P_T3_34
IO_L19N_T3_VREF_34
IO_L20P_T3_34
IO_L20N_T3_34
IO_L21P_T3_DQS_34
IO_L21N_T3_DQS_34
IO_L22P_T3_34
IO_L22N_T3_34
IO_L23P_T3_34
IO_L23N_T3_34
IO_L24P_T3_34
IO_L24N_T3_34
IO_25_34
IO_0_35
IO_L1P_T0_AD4P_35
IO_L1N_T0_AD4N_35
IO_L2P_T0_AD12P_35
IO_L2N_T0_AD12N_35
IO_L3P_T0_DQS_AD5P_35
IO_L3N_T0_DQS_AD5N_35
IO_L4P_T0_35
IO_L4N_T0_35
IO_L5P_T0_AD13P_35
IO_L5N_T0_AD13N_35
IO_L6P_T0_35
IO_L6N_T0_VREF_35
IO_L7P_T1_AD6P_35
IO_L7N_T1_AD6N_35
IO_L8P_T1_AD14P_35
IO_L8N_T1_AD14N_35
IO_L9P_T1_DQS_AD7P_35
IO_L9N_T1_DQS_AD7N_35
IO_L10P_T1_AD15P_35
IO_L10N_T1_AD15N_35
IO_L11P_T1_SRCC_35
IO_L11N_T1_SRCC_35
IO_L12P_T1_MRCC_35
IO_L12N_T1_MRCC_35
IO_L13P_T2_MRCC_35
IO_L13N_T2_MRCC_35
IO_L14P_T2_SRCC_35
IO_L14N_T2_SRCC_35
IO_L15P_T2_DQS_35
IO_L15N_T2_DQS_35
IO_L16P_T2_35
IO_L16N_T2_35
IO_L17P_T2_35
IO_L17N_T2_35
IO_L18P_T2_35
IO_L18N_T2_35
IO_L19P_T3_35
IO_L19N_T3_VREF_35
IO_L20P_T3_35
IO_L20N_T3_35
IO_L21P_T3_DQS_35
IO_L21N_T3_DQS_35
IO_L22P_T3_35
IO_L22N_T3_35
IO_L23P_T3_35
IO_L23N_T3_35
IO_L24P_T3_35
IO_L24N_T3_35
IO_25_35
SW3_2A
SW3_2B

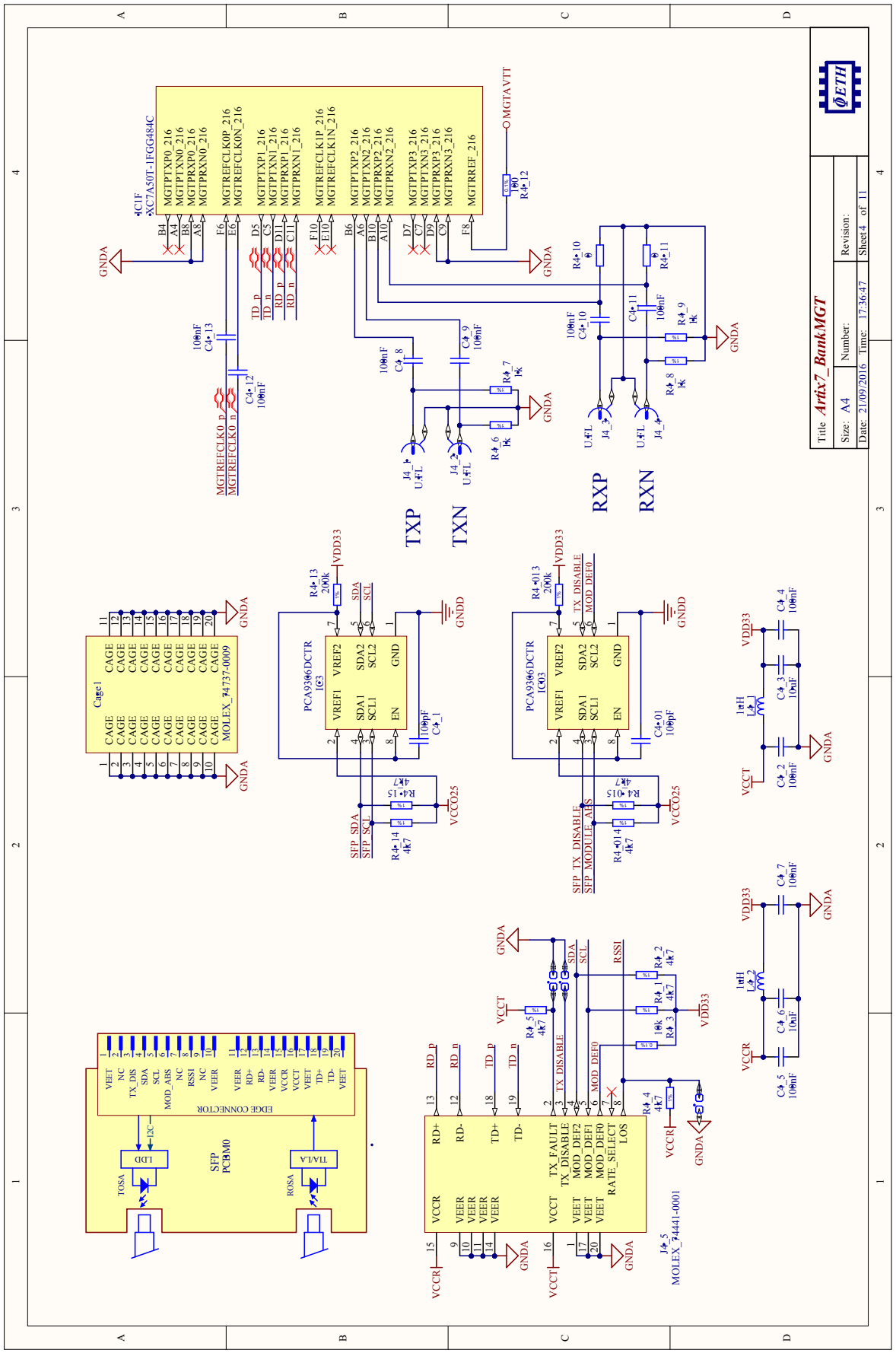
Title Artix7_BankMGT
Size: A4
Number:
Revision:
Date: 21/09/2016
Time: 17:36:47
Sheet 4 of 11
ETH
TXP
TXN
RXP
RXN
MGTAVTT
GNDA
GNDD
VCCO25
VDD33
VCCT
VCCR
SFP_SDA
SFP_SCL
SFP_TX_DISABLE
SFP_MODULE_ABS
RSSI
MGTREFCLK0_p
MGTREFCLK0_n
TD_p
TD_n
RD_p
RD_n
SFP PCBM0
TOSA
ROSA
LDD
TIA/LA
EDGE CONNECTOR
MOLEX_74737-0009
MOLEX_74441-0001
PCA9306DCTR
XC7A50T-1FGG484C

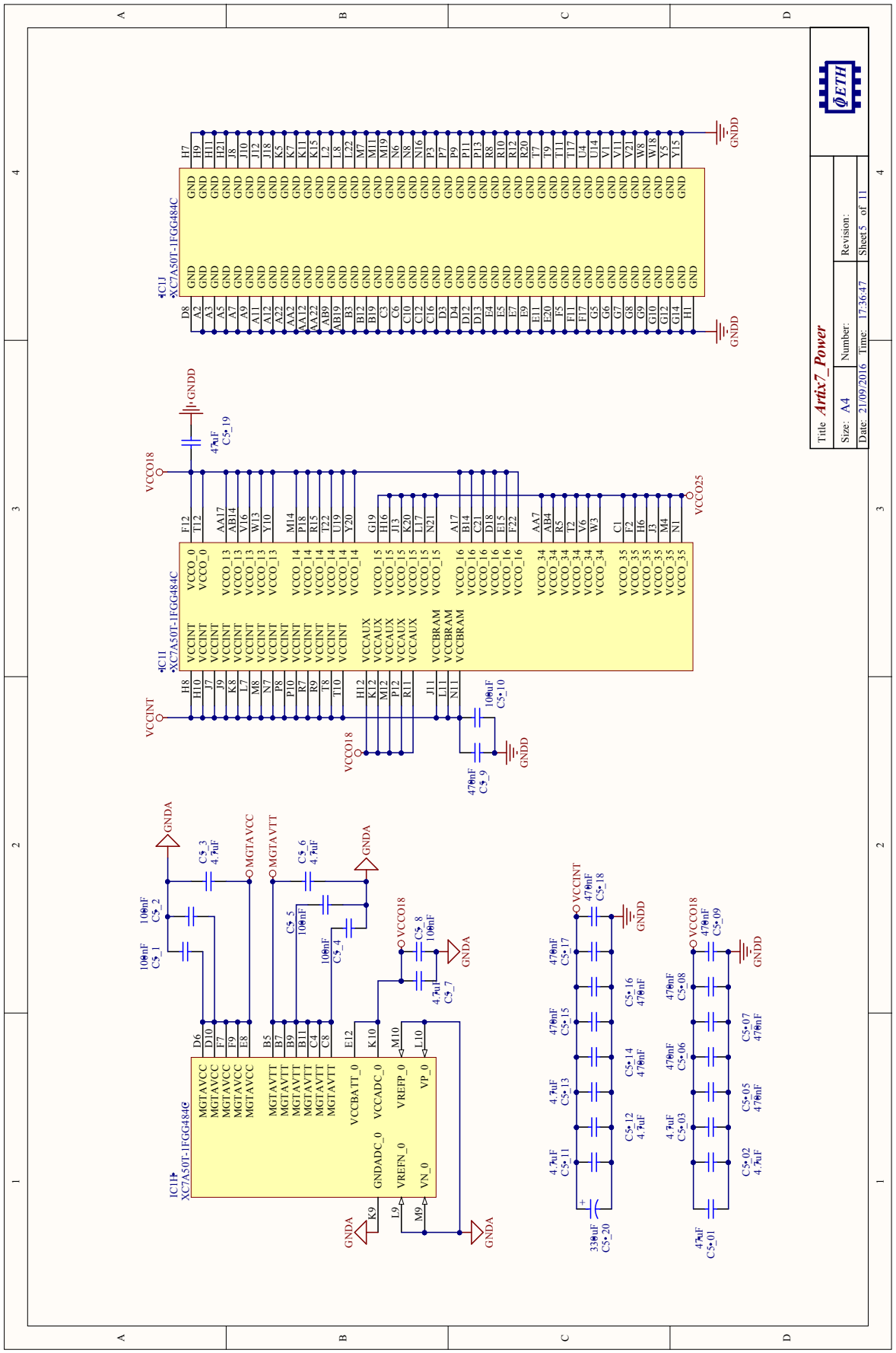
Title Artix7_Power
Size: A4
Number:
Revision:
Date: 21/09/2016
Time: 17:36:47
Sheet 5 of 11
ETH
IC1J XC7A50T-1FGG484C
IC1I XC7A50T-1FGG484C
IC1H XC7A50T-1FGG484C
GNDD
GNDA
VCCINT
VCCO18
VCCO25
MGTAVCC
MGTAVTT
100nF C5_1
100nF C5_2
4.7uF C5_3
100nF C5_4
100nF C5_5
4.7uF C5_6
100nF C5_8
4.7uF C5_7
47uF C5_19
100uF C5_10
470nF C5_9
4.7uF C5_11
4.7uF C5_12
4.7uF C5_13
470nF C5_14
470nF C5_15
470nF C5_16
470nF C5_17
47nF C5_18
330uF C5_20
4.7uF C5_01
4.7uF C5_02
4.7uF C5_03
470nF C5_05
470nF C5_06
470nF C5_07
470nF C5_08
470nF C5_09
L9
M9

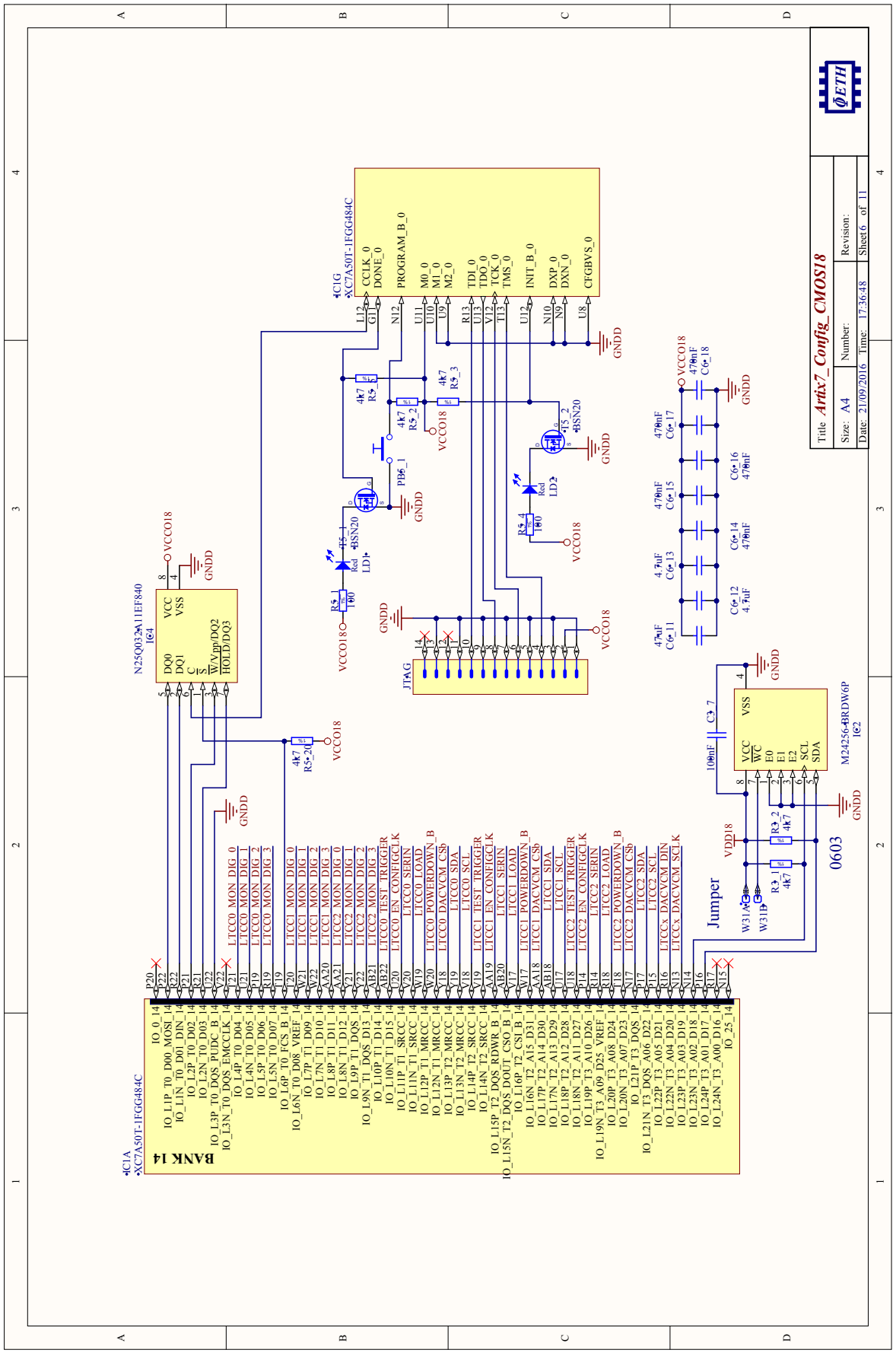
Title Artix7_Config_CMOS18
Size: A4
Number:
Revision:
Date: 21/09/2016
Time: 17:36:48
Sheet 6 of 11
ETH
BANK 14
XC7A50T-1FGG484C
XC7A50T-1FGG484C
N25Q032A11EF840
M24256-BRDW6P
JTAG
Jumper
0603
VCCO18
GNDD
VDD18

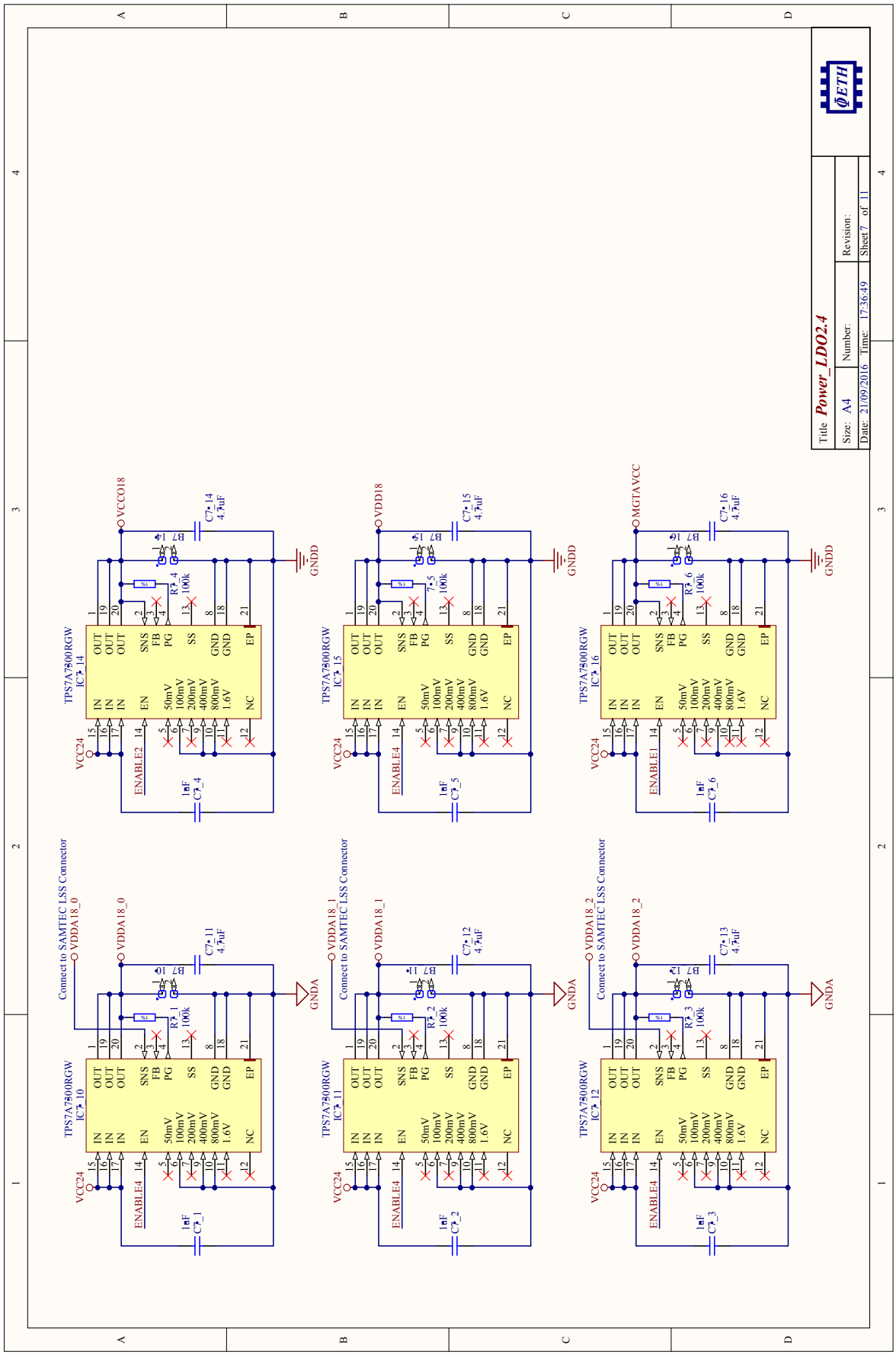
Title Power_LDO2.4
Size: A4
Number:
Revision:
Date: 21/09/2016
Time: 17:36:49
Sheet 7 of 11
ETH
VCC24
VCCO18
VDD18
MGTAVCC
VDDA18_0
VDDA18_1
VDDA18_2
GNDA
GNDD
Connect to SAMTEC LSS Connector
TPS7A7900RGW
ENABLE1
ENABLE2
ENABLE4
1nF
4.7uF
100k

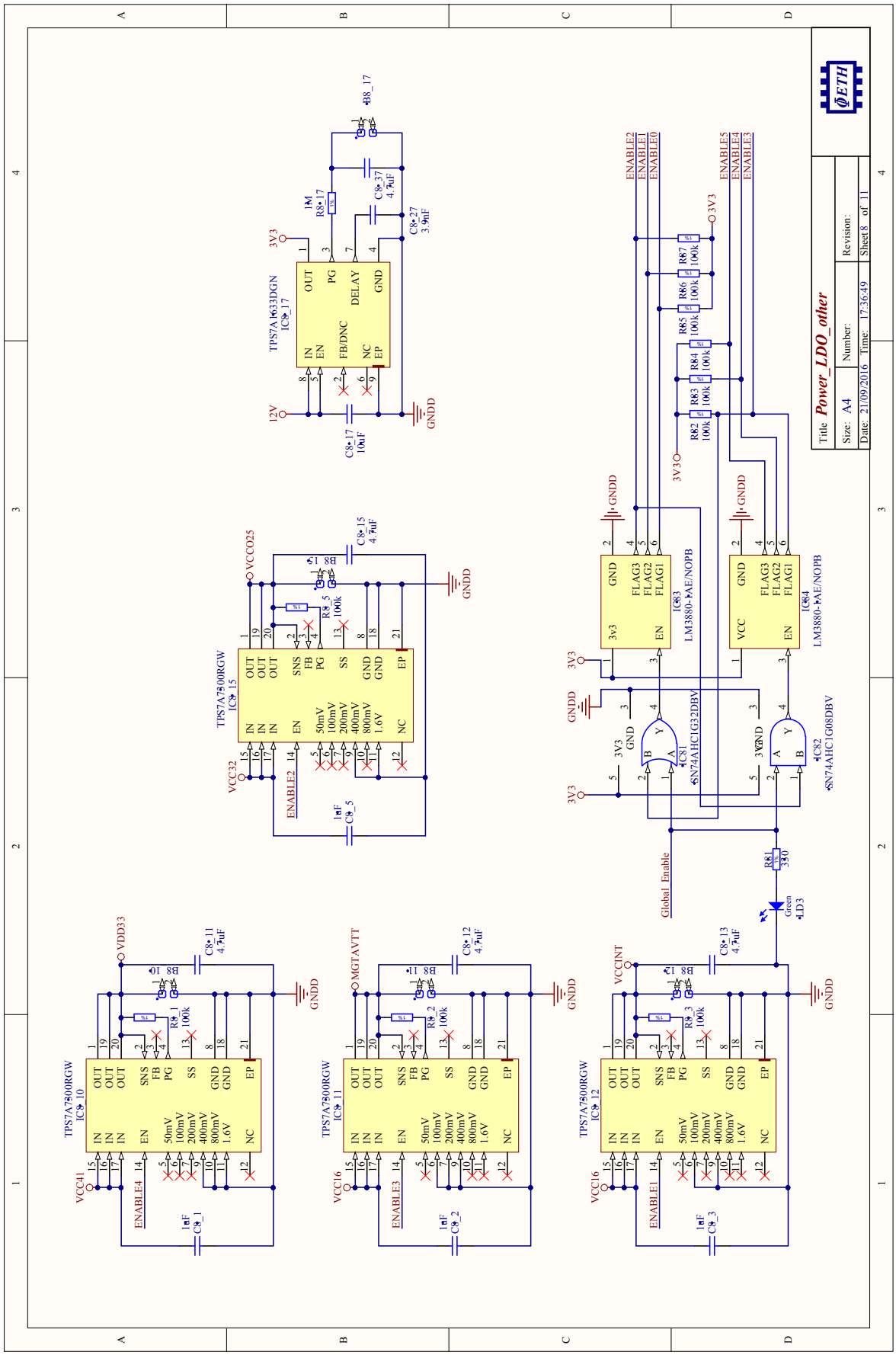
Title Power_LDO_other
Size: A4
Number:
Revision:
Date: 21/09/2016
Time: 17:36:49
Sheet 8 of 11
TPS7A7300RGW
TPS7A1633DGN
LM3880-AAE/NOPB
SN74AHC1G32DBV
SN74AHC1G08DBV
VDD33
MGTAVTT
VCCINT
VCC41
VCC16
VCC32
VCCO25
12V
3V3
GNDD
ENABLE0
ENABLE1
ENABLE2
ENABLE3
ENABLE4
ENABLE5
Global_Enable
Green
LD3

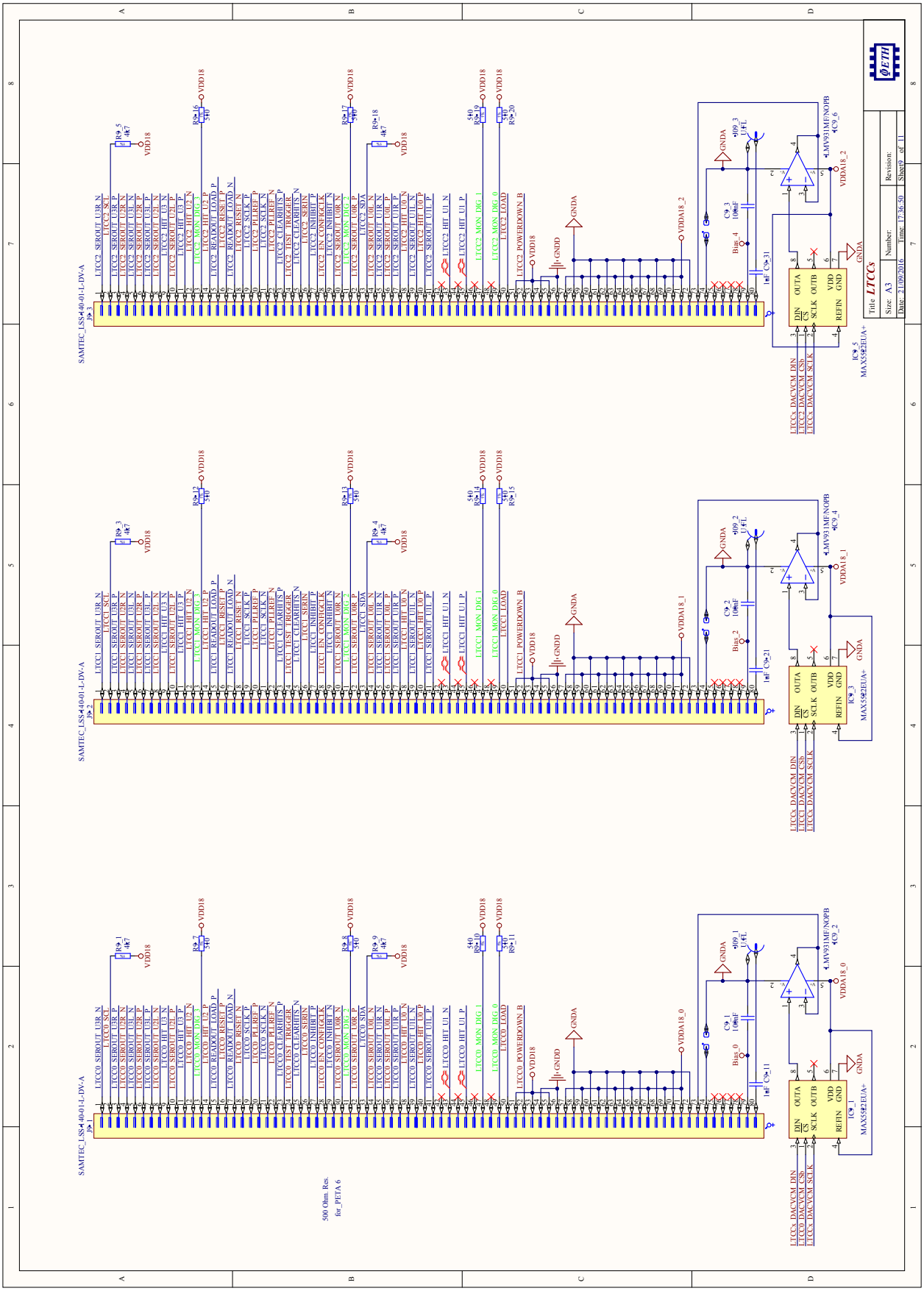
SAMTEC_LSS-140-01-L-DV-A
LTCC2_SEROUT_U3R_N
LTCC2_SEROUT_U3R_P
LTCC2_SEROUT_U2R_N
LTCC2_SEROUT_U2R_P
LTCC2_SEROUT_U3L_N
LTCC2_SEROUT_U3L_P
LTCC2_SEROUT_U2L_N
LTCC2_SEROUT_U2L_P
LTCC2_HIT_U3_N
LTCC2_HIT_U3_P
LTCC2_HIT_U2_N
LTCC2_HIT_U2_P
LTCC2_READOUT_LOAD_N
LTCC2_READOUT_LOAD_P
LTCC2_RESET_N
LTCC2_RESET_P
LTCC2_SCLK_N
LTCC2_SCLK_P
LTCC2_PLLREF_N
LTCC2_PLLREF_P
LTCC2_TEST_TRIGGER_N
LTCC2_TEST_TRIGGER_P
LTCC2_CLEARHITS_N
LTCC2_CLEARHITS_P
LTCC2_SERIN
LTCC2_INHIBIT_N
LTCC2_INHIBIT_P
LTCC2_SCLK
LTCC2_MON_DIG_2
LTCC2_SEROUT_U0R_N
LTCC2_SEROUT_U0R_P
LTCC2_SEROUT_U0L_N
LTCC2_SEROUT_U0L_P
LTCC2_SEROUT_U1R_N
LTCC2_SEROUT_U1R_P
LTCC2_SEROUT_U1L_N
LTCC2_SEROUT_U1L_P
LTCC2_HIT_U0_N
LTCC2_HIT_U0_P
LTCC2_HIT_U1_N
LTCC2_HIT_U1_P
LTCC2_MON_DIG_1
LTCC2_MON_DIG_0
LTCC2_LOAD
LTCC2_POWERDOWN_B
VDD18
GNDA
VDDA18_2
R9_5 4K7
R9_16 510
R9_17 510
R9_18 4K7
R9_19 510
R9_20 510
C9_3 100nF
Bias_4
C9_31 1nF
C9_6
VDDA18_2
IC9_5 MAX5582EUA+
LTCCx_DACVCM_DIN
LTCC2_DACVCM_CSb
LTCCx_DACVCM_SCLK
SAMTEC_LSS-140-01-L-DV-A
LTCC1_SEROUT_U3R_N
LTCC1_SEROUT_U3R_P
LTCC1_SEROUT_U2R_N
LTCC1_SEROUT_U2R_P
LTCC1_SEROUT_U3L_N
LTCC1_SEROUT_U3L_P
LTCC1_SEROUT_U2L_N
LTCC1_SEROUT_U2L_P
LTCC1_HIT_U3_N
LTCC1_HIT_U3_P
LTCC1_HIT_U2_N
LTCC1_HIT_U2_P
LTCC1_READOUT_LOAD_N
LTCC1_READOUT_LOAD_P
LTCC1_RESET_N
LTCC1_RESET_P
LTCC1_SCLK_N
LTCC1_SCLK_P
LTCC1_PLLREF_P
LTCC1_PLLREF_N
LTCC1_TEST_TRIGGER_P
LTCC1_TEST_TRIGGER_N
LTCC1_CLEARHITS_N
LTCC1_SERIN
LTCC1_INHIBIT_P
LTCC1_INHIBIT_N
LTCC1_SCLK
LTCC1_MON_DIG_2
LTCC1_SEROUT_U0R_N
LTCC1_SEROUT_U0R_P
LTCC1_SEROUT_U0L_N
LTCC1_SEROUT_U0L_P
LTCC1_SEROUT_U1R_N
LTCC1_SEROUT_U1R_P
LTCC1_SEROUT_U1L_N
LTCC1_SEROUT_U1L_P
LTCC1_HIT_U0_N
LTCC1_HIT_U0_P
LTCC1_HIT_U1_N
LTCC1_HIT_U1_P
LTCC1_MON_DIG_1
LTCC1_MON_DIG_0
LTCC1_LOAD
LTCC1_POWERDOWN_B
VDD18
GNDA
VDDA18_1
R9_3 4K7
R9_12 510
R9_13 510
R9_14 510
R9_15 510
R9_4 4K7
C9_2 100nF
Bias_2
C9_21 1nF
C9_4
VDDA18_1
IC9_3 MAX5582EUA+
LTCCx_DACVCM_DIN
LTCC1_DACVCM_CSb
LTCCx_DACVCM_SCLK
SAMTEC_LSS-140-01-L-DV-A
LTCC0_SEROUT_U3R_N
LTCC0_SEROUT_U3R_P
LTCC0_SEROUT_U2R_N
LTCC0_SEROUT_U2R_P
LTCC0_SEROUT_U3L_N
LTCC0_SEROUT_U3L_P
LTCC0_SEROUT_U2L_N
LTCC0_SEROUT_U2L_P
LTCC0_HIT_U3_N
LTCC0_HIT_U3_P
LTCC0_HIT_U2_N
LTCC0_HIT_U2_P
LTCC0_READOUT_LOAD_N
LTCC0_READOUT_LOAD_P
LTCC0_RESET_N
LTCC0_RESET_P
LTCC0_SCLK_N
LTCC0_SCLK_P
LTCC0_PLLREF_P
LTCC0_PLLREF_N
LTCC0_TEST_TRIGGER_P
LTCC0_TEST_TRIGGER_N
LTCC0_CLEARHITS_N
LTCC0_SERIN
LTCC0_INHIBIT_P
LTCC0_INHIBIT_N
LTCC0_SCLK
LTCC0_MON_DIG_2
LTCC0_SEROUT_U0R_N
LTCC0_SEROUT_U0R_P
LTCC0_SEROUT_U0L_N
LTCC0_SEROUT_U0L_P
LTCC0_SEROUT_U1R_N
LTCC0_SEROUT_U1R_P
LTCC0_SEROUT_U1L_N
LTCC0_SEROUT_U1L_P
LTCC0_HIT_U0_N
LTCC0_HIT_U0_P
LTCC0_HIT_U1_N
LTCC0_HIT_U1_P
LTCC0_MON_DIG_1
LTCC0_MON_DIG_0
LTCC0_LOAD
LTCC0_POWERDOWN_B
VDD18
GNDA
VDDA18_0
R9_1 4K7
R9_7 510
R9_8 510
R9_9 4K7
R9_10 510
R9_11 510
C9_1 100nF
Bias_0
C9_11 1nF
C9_7
VDDA18_0
IC9_1 MAX5582EUA+
LTCCx_DACVCM_DIN
LTCC0_DACVCM_CSb
LTCCx_DACVCM_SCLK
500 Ohm. Res.
for_PETA 6
Title LTCCs
Size: A3
Number:
Revision:
Date: 21/09/2016
Time: 17:36:50
Sheet 9 of 11

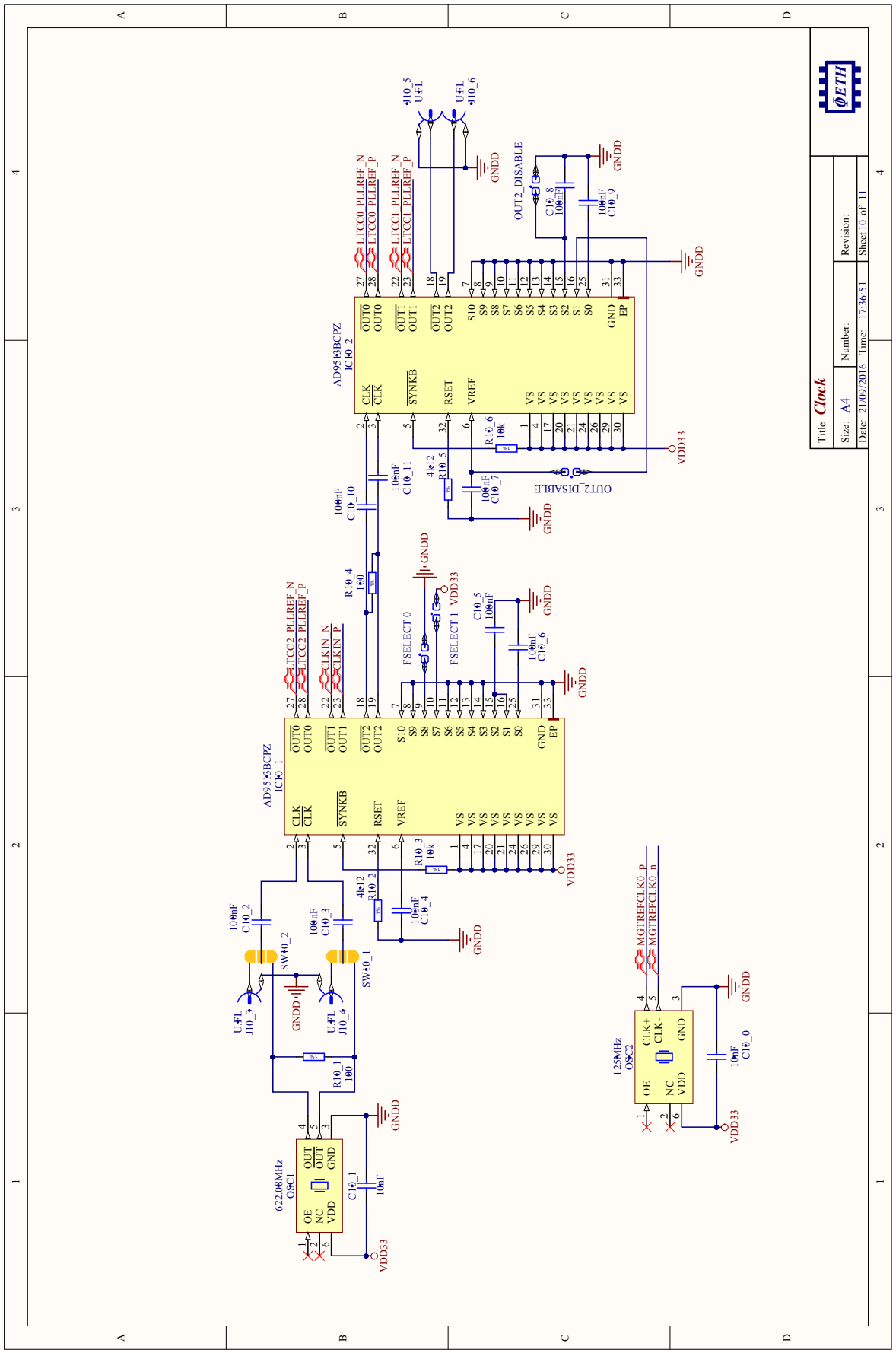
Title Clock
Size: A4
Number:
Revision:
Date: 21/09/2016
Time: 17:36:51
Sheet 10 of 11
AD9516BCPZ
IC10_1
AD9516BCPZ
IC10_2
622.08MHz
OSC1
125MHz
OSC2
OUT2_DISABLE
FSELECT 0
FSELECT 1
VDD33
GNDD
LTCC2_PLLREF_N
LTCC2_PLLREF_P
CLKIN_N
CLKIN_P
LTCC0_PLLREF_N
LTCC0_PLLREF_P
LTCC1_PLLREF_N
LTCC1_PLLREF_P
MGTREFCLK0_p
MGTREFCLK0_n

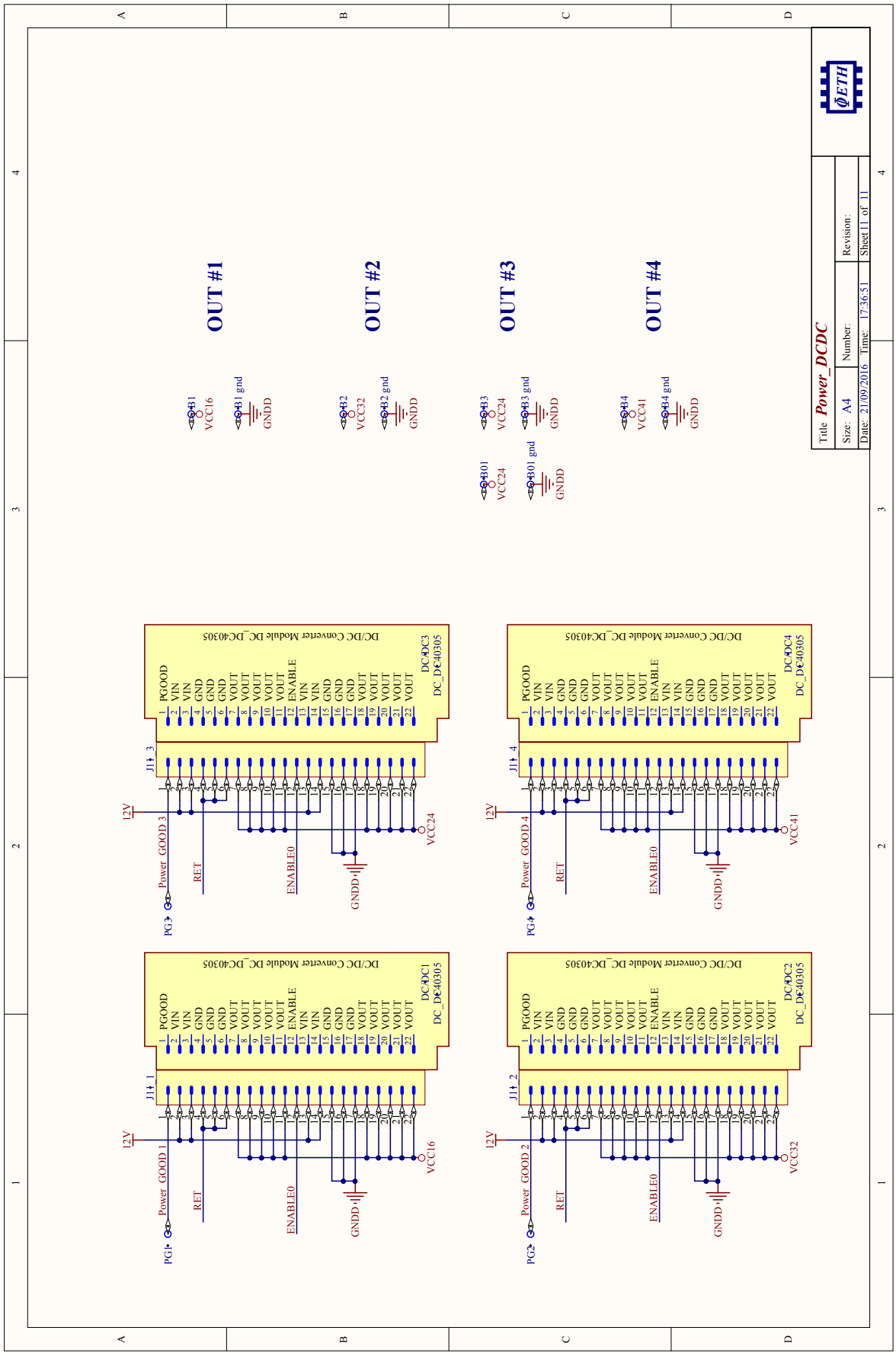
OUT #1
OUT #2
OUT #3
OUT #4
VCC16
VCC32
VCC24
VCC41
GNDD
Title Power_DCDC
Size: A4
Number:
Revision:
Date: 21/09/2016
Time: 17:36:51
Sheet 11 of 11
DC/DC Converter Module DC_DC40305
PGOOD
VIN
GND
VOUT
ENABLE
12V
RET
ENABLE0
Power_GOOD 1
Power_GOOD 2
Power_GOOD 3
Power_GOOD 4
PG1
PG2
PG3
PG4

C

CALCULATIONS AND SETUPS

C.1 MEASUREMENT OF INDUCTANCE

The custom DC-DC converters need to be equipped with a magnetic field tolerant inductance. Aircore coils with an inductance around a micro-Henry as needed for the designs under consideration are not commercially available with a sufficient current rating. Furthermore, two different geometries, toroid and circular, are to be investigated for their interference with the MRI. To ensure the correct inductance, the inductance of each wound coil has to be measured. In a method proposed by [71] this is done using a waveform generator and an oscilloscope as shown in figure 57.

The waveform generator is configured to output a sinusoidal wave of 1 V peak-to-peak amplitude when the inductor L ist not connected. This is the voltage U_{gen}. When the inductor is in place, the voltage measured at the oscilloscope is U_{scope}. The resistance R_{term} and the inductance with its serial resistance act as a frequency-dependent voltage divider

$$U_{scope} = \frac{j\omega L + R_L}{j\omega L + R_{term} + R_L} U_{gen}, \tag{62}$$

where $\omega = 2\pi f$ is the angular frequency and f is the frequency. The absolute value of the voltage ratio is

$$\left| \frac{U_{scope}}{U_{gen}} \right|^2 = \frac{R_L^2 + \omega^2 L^2}{R_{term}^2 + R_L^2 + 2R_{term}R_L + \omega^2 L^2} \tag{63}$$

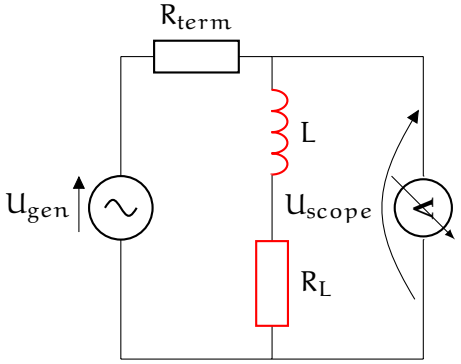

Figure 57: Measuring an unknown inductance L with a series resistance R_L using a waveform generator with an output impedance R_{term}.

With the inductor in place, the frequency f is adjusted such that the the peak-to-peak amplitude of the sinusoidal voltage is 0.5 V. This yields a relationship for L

$$\frac{1}{4} = \frac{R_L^2 + \omega^2 L^2}{R_{term}^2 + R_L^2 + 2R_{term}R_L + \omega^2 L^2} \tag{64}$$

$$\Leftrightarrow L = \sqrt{\frac{R_{term}^2 - 3R_L^2 + 2R_{term}R_L}{12\pi^2}} \cdot \frac{1}{f}. \tag{65}$$

In the special case of negligible serial resistance R_L and a termination resistance of $R_{term} = 50\,\Omega$, the formula reduces to

$$L = \frac{R_{term}}{2\sqrt{3}\pi}\frac{1}{f} = \frac{4.59}{f}.$$

BIBLIOGRAPHY

[1] B. Weber et al. "Quantitative Cerebral Blood Flow Measurements in the Rat Using a Beta-Probe and H215O." In: *Journal of Cerebral Blood Flow & Metabolism* (Dec. 2003), pp. 1455–1460. ISSN: 0271-678X. DOI: 10.1097/01.wcb.0000095799.98378.7d. URL: http://dx.doi.org/10.1097/01.WCB.0000095799.98378.7D.

[2] A. Nordberg et al. "The use of PET in Alzheimer disease." In: *Nature Reviews Neurology* 6.2 (Feb. 2010), pp. 78–87. ISSN: 1759-4766. DOI: 10.1038/nrneurol.2009.217. URL: http://dx.doi.org/10.1038/nrneurol.2009.217.

[3] S. M. Landau et al. "Comparing positron emission tomography imaging and cerebrospinal fluid measurements of β-amyloid." In: *Annals of Neurology* 74.6 (Dec. 2013), pp. 826–836. ISSN: 0364-5134. DOI: 10.1002/ana.23908. URL: http://dx.doi.org/10.1002/ana.23908.

[4] F. C. Maier et al. "Longitudinal PET-MRI reveals β-amyloid deposition and rCBF dynamics and connects vascular amyloidosis to quantitative loss of perfusion." In: *Nature Medicine* 20.12 (Nov. 2014), pp. 1485–1492. ISSN: 1546-170X. DOI: 10.1038/nm.3734. URL: http://dx.doi.org/10.1038/nm.3734.

[5] J. Sevigny et al. "The antibody aducanumab reduces Aβ plaques in Alzheimer's disease." In: *Nature* 537.7618 (Aug. 2016), pp. 50–56. ISSN: 1476-4687. DOI: 10.1038/nature19323. URL: http://dx.doi.org/10.1038/nature19323.

[6] M. M. Ter-Pogossian et al. "A Positron-Emission Transaxial Tomograph for Nuclear Imaging (PETT) 1." In: *Radiology* 114.1 (Jan. 1975), pp. 89–98. ISSN: 1527-1315. DOI: 10.1148/114.1.89. URL: http://dx.doi.org/10.1148/114.1.89.

[7] M. E. Phelps et al. "Application of annihilation coincidence detection to transaxial reconstruction tomography." In: *J Nucl Med* 16.3 (Mar. 1975), pp. 210–224. URL: http://www.ncbi.nlm.nih.gov/pubmed/1113170.

[8] S. Vandenberghe et al. "Recent developments in time-of-flight PET." In: *EJNMMI Physics* 3.1 (Feb. 2016). ISSN: 2197-7364. DOI: 10.1186/s40658-016-0138-3. URL: http://dx.doi.org/10.1186/s40658-016-0138-3.

[9] M. Berger et al. "XCOM: Photon Cross Sections Database." In: *NIST Standard Reference Database 8 (XGAM)* (1998). URL: https://www.nist.gov/pml/xcom-photon-cross-sections-database.

[10] C. Melcher and J. Schweitzer. "A promising new scintillator: cerium-doped lutetium oxyorthosilicate." In: *Nuclear Instruments and Methods in Physics Research Section A: Accelerators, Spectrometers, Detectors and Associated Equipment* 314.1 (Apr. 1992), pp. 212–214. ISSN: 0168-9002. DOI: 10.1016/0168-9002(92)90517-8. URL: http://dx.doi.org/10.1016/0168-9002(92)90517-8.

[11] S. E. Brunner et al. "Studies on the Cherenkov Effect for Improved Time Resolution of TOF-PET." In: *IEEE Transactions on Nuclear Science* 61.1 (Feb. 2014), pp. 443–447. ISSN: 1558-1578. DOI: 10.1109/tns.2013.2281667. URL: http://dx.doi.org/10.1109/TNS.2013.2281667.

[12] K. Olive. "Review of Particle Physics." In: *Chinese Physics C* 40.10 (Oct. 2016), p. 100001. ISSN: 1674-1137. DOI: 10.1088/1674-1137/40/10/100001. URL: http://dx.doi.org/10.1088/1674-1137/40/10/100001.

[13] *Atomic and nuclear properties of lutetium silicon oxide (Lu2SiO5)*. URL: http://pdg.lbl.gov/2016/AtomicNuclearProperties/HTML/lutetium_silicon_oxide.html.

[14] S. Derenzo et al. "The quest for the ideal inorganic scintillator." In: *Nuclear Instruments and Methods in Physics Research Section A: Accelerators, Spectrometers, Detectors and Associated Equipment* 505.1 (2003). Proceedings of the tenth Symposium on Radiation Measurements and Applications, pp. 111–117. ISSN: 0168-9002. DOI: http://dx.doi.org/10.1016/S0168-9002(03)01031-3. URL: http://www.sciencedirect.com/science/article/pii/S0168900203010313.

[15] H. Ibach and H. Lüth. *Festkörperphysik*. Springer Berlin Heidelberg, Jan. 24, 2009. URL: https://link.springer.com/book/10.1007/978-3-540-85795-2.

[16] P. A. Cutler et al. "Scintillation Non-Proportionality of Lutetium- and Yttrium-Based Silicates and Aluminates." In: *IEEE Transactions on Nuclear Science* 56.3 (June 2009), pp. 915–919. ISSN: 0018-9499. DOI: 10.1109/tns.2009.2016421. URL: http://dx.doi.org/10.1109/TNS.2009.2016421.

[17] J. T. M. de Haas and P. Dorenbos. "Advances in Yield Calibration of Scintillators." In: *IEEE Transactions on Nuclear Science* 55.3 (June 2008), pp. 1086–1092. ISSN: 0018-9499. DOI: 10.1109/tns.2008.922819. URL: http://dx.doi.org/10.1109/TNS.2008.922819.

[18] *Non-homogeneous Poisson Processes*. The University of Alabama in Huntsville. Feb. 2017. URL: http://www.math.uah.edu/stat/poisson/Nonhomogeneous.html.

[19] *Opto-semiconductor handbook chapter 3*. Hamamatsu Photonics K.K. URL: http://www.hamamatsu.com/resources/pdf/ssd/e03_handbook_si_apd_mppc.pdf.

[20] Z. J. O. Sadygov. "Avalanche Detector." RU. 2102820C1. Jan. 1998. URL: https://depatisnet.dpma.de/DepatisNet/depatisnet?action=bibdat&docid=RU000002102820C1.

[21] G. Bondarenko, V. M. Golovin, and M. L. Tarasov. "Avalanche Photodetector." RU. 2142175C1. Nov. 1999. URL: https://depatisnet.dpma.de/DepatisNet/depatisnet?action=bibdat&docid=RU000002142175C1.

[22] D. Renker. "Geiger-mode avalanche photodiodes, history, properties and problems." In: *Nuclear Instruments and Methods in Physics Research Section A: Accelerators, Spectrometers, Detectors and Associated Equipment* 567.1 (Nov. 2006), pp. 48–56. ISSN: 0168-9002. DOI: 10.1016/j.nima.2006.05.060. URL: http://dx.doi.org/10.1016/j.nima.2006.05.060.

[23] *Si APD (Avalanche Photodiode) – Selection Guide*. Hamamatsu Photonics K.K. Mar. 2014. URL: https://www.hamamatsu.com/resources/pdf/ssd/si_apd_kapd0001e.pdf.

[24] M. E. Daube-Witherspoon and G. Muehllehner. "Treatment of axial data in three-dimensional PET." In: *J Nucl Med* 28.11 (1987), pp. 1717–1724.

[25] M. Defrise et al. "Exact and approximate rebinning algorithms for 3-D PET data." In: *IEEE Transactions on Medical Imaging* 16.2 (Apr. 1997), pp. 145–158. ISSN: 0278-0062. DOI: 10.1109/42.563660.

[26] T. F. Budinger et al. "Emission computer assisted tomography with single-photon and positron annihilation photon emitters." eng. In: *J Comput Assist Tomogr* 1.1 (Jan. 1977), pp. 131–145. URL: http://www.ncbi.nlm.nih.gov/pubmed/615887.

[27] J. Radon. "Über die Bestimmung von Funktionen durch ihre Integralwerte längs gewisser Mannigfaltigkeiten." In: *Berichte über die Verhandlungen der Königlich sächsischen Gesellschaft der Wissenschaften zu Leipzig; Mathematisch-physische Klasse* 69 (Apr. 1917), pp. 262–277.

[28] A. K. Louis. "Inverse und schlecht gestellte Probleme." In: (1989). DOI: 10.1007/978-3-322-84808-6. URL: http://dx.doi.org/10.1007/978-3-322-84808-6.

[29] J. Hadamard. "Sur les problèmes aux dérivées partielles et leur signification physique." In: *Princeton University Bulletin* 13.4 (Apr. 1902), pp. 49–52.

[30] H. Nyquist. "Certain Topics in Telegraph Transmission Theory." In: *Transactions of the American Institute of Electrical Engineers* 47.2 (Apr. 1928), pp. 617–644. ISSN: 0096-3860. DOI: 10.1109/T-AIEE.1928.5055024.

[31] C. E. Shannon. "Communication In The Presence Of Noise." In: *Proceedings of the IEEE* 86.2 (Feb. 1998), pp. 447–457. ISSN: 0018-9219. DOI: 10.1109/JPROC.1998.659497.

[32] P. Kinahan and J. Rogers. "Analytic 3D image reconstruction using all detected events." In: *IEEE Transactions on Nuclear Science* 36.1 (1989), pp. 964–968. ISSN: 0018-9499. DOI: 10.1109/23.34585. URL: http://dx.doi.org/10.1109/23.34585.

[33] L. A. Shepp and Y. Vardi. "Maximum Likelihood Reconstruction for Emission Tomography." In: *IEEE Transactions on Medical Imaging* 1.2 (Oct. 1982), pp. 113–122. ISSN: 1558-254X. DOI: 10.1109/tmi.1982.4307558. URL: http://dx.doi.org/10.1109/TMI.1982.4307558.

[34] U. Locans et al. "Real-Time Computation of Parameter Fitting and Image Reconstruction Using Graphical Processing Units." In: *arXiv* (Apr. 2016). eprint: 1604.02334. URL: https://arxiv.org/abs/1604.02334.

[35] E. Morris et al. "Diagnostic accuracy of 18F amyloid PET tracers for the diagnosis of Alzheimer's disease: a systematic review and meta-analysis." In: *European Journal of Nuclear Medicine and Molecular Imaging* 43.2 (Nov. 2015), pp. 374–385. ISSN: 1619-7089. DOI: 10.1007/s00259-015-3228-x. URL: http://dx.doi.org/10.1007/s00259-015-3228-x.

[36] R. Becker et al. "Monte-Carlo Simulation Based Estimation of NECR, Sensitivity, and Spatial Resolution of a Novel Preclinical PET Insert for MR." In: *Nuclear Science Symposium Conference Record (NSS/MIC)*. IEEE. IEEE, 2015.

[37] T. Harion et al. "STiC — a mixed mode silicon photomultiplier readout ASIC for time-of-flight applications." In: *Journal of Instrumentation* 9.02 (Feb. 2014), pp. C02003–C02003. ISSN: 1748-0221. DOI: 10.1088/1748-0221/9/02/c02003. URL: http://dx.doi.org/10.1088/1748-0221/9/02/C02003.

[38] I. Sacco et al. "A compact, high-density gamma-detection module for Time-of-Flight measurements in PET applications." In: *Nuclear Instruments and Methods in Physics Research Section A: Accelerators, Spectrometers, Detectors and Associated Equipment* (Nov. 2015). ISSN: 0168-9002. DOI: 10.1016/j.nima.2015.11.004. URL: http://dx.doi.org/10.1016/j.nima.2015.11.004.

[39] I. Sacco, P. Fischer, and M. Ritzert. "PETA4: a multi-channel TDC/ADC ASIC for SiPM readout." In: *Journal of Instrumentation* 8.12 (Dec. 2013), pp. C12013–C12013. ISSN: 1748-0221. DOI: 10.1088/1748-0221/8/12/c12013. URL: http://dx.doi.org/10.1088/1748-0221/8/12/C12013.

[40] S. Agostinelli et al. "Geant4—a simulation toolkit." In: *Nuclear Instruments and Methods in Physics Research Section A: Accelerators, Spectrometers, Detectors and Associated Equipment* 506.3 (July 2003), pp. 250–303. ISSN: 0168-9002. DOI: 10.1016/s0168-9002(03)01368-8. URL: http://dx.doi.org/10.1016/S0168-9002(03)01368-8.

[41] J. Allison et al. "Geant4 developments and applications." In: *IEEE Transactions on Nuclear Science* 53.1 (Feb. 2006), pp. 270–278. ISSN: 0018-9499. DOI: 10.1109/tns.2006.869826. URL: http://dx.doi.org/10.1109/TNS.2006.869826.

[42] J. Allison et al. "Recent developments in Geant4." In: *Nuclear Instruments and Methods in Physics Research Section A: Accelerators, Spectrometers, Detectors and Associated Equipment* 835 (Nov. 2016), pp. 186–225. ISSN: 0168-9002. DOI: 10.1016/j.nima.2016.06.125. URL: http://dx.doi.org/10.1016/j.nima.2016.06.125.

[43] S. Jan et al. "GATE: a simulation toolkit for PET and SPECT." In: *Physics in Medicine and Biology* 49.19 (Sept. 2004), pp. 4543–4561. ISSN: 1361-6560. DOI: 10.1088/0031-9155/49/19/007. URL: http://dx.doi.org/10.1088/0031-9155/49/19/007.

[44] G. Santin et al. "Evolution of the GATE project: new results and developments." In: *Nuclear Physics B - Proceedings Supplements* 172 (Oct. 2007), pp. 101–103. ISSN: 0920-5632. DOI: 10.1016/j.nuclphysbps.2007.07.008. URL: http://dx.doi.org/10.1016/j.nuclphysbps.2007.07.008.

[45] C. W. Stearns et al. "Random coincidence estimation from single event rates on the Discovery ST PET/CT scanner." In: *Nuclear Science Symposium Conference Record, 2003 IEEE*. Vol. 5. 2003, pp. 3067–3069. DOI: 10.1109/NSSMIC.2003.1352545. URL: http://ieeexplore.ieee.org/stamp/stamp.jsp?arnumber=1352545.

[46] K. Thielemans et al. "STIR: software for tomographic image reconstruction release 2." In: *Phys. Med. Biol.* 57.4 (Jan. 2012), pp. 867–883. ISSN: 1361-6560. DOI: 10.1088/0031-9155/57/4/867. URL: http://dx.doi.org/10.1088/0031-9155/57/4/867.

[47] J. Fischer. *SAFIR input file format for STIR*. 2015. DOI: 10.5905/ethz-1007-22. URL: http://doi.org/10.5905/ethz-1007-22.

[48] *NEMA Standards Publication NU 4-2008: Performance Measurements of Small Animal Positron Emission Tomographs*. 1300 N. 17th Street, Suite 1752 Rosslyn, VA 22209: National Electrical Manufacturers Association, 2008. URL: https://www.nema.org/

Standards/ComplimentaryDocuments/NU-4-2008-website.pdf.

[49] *NEMA Standards Publication NU 2-2012: Performance Measurements of Positron Emission Tomographs*. 1300 N. 17th Street, Suite 1752 Rosslyn, VA 22209: National Electrical Manufacturers Association, 2012.

[50] S. Strother, M. Casey, and E. Hoffman. "Measuring PET scanner sensitivity: relating countrates to image signal-to-noise ratios using noise equivalents counts." In: *IEEE Transactions on Nuclear Science* 37.2 (Apr. 1990), pp. 783–788. ISSN: 0018-9499. DOI: 10.1109/23.106715. URL: http://dx.doi.org/10.1109/23.106715.

[51] A. L. Goertzen et al. "NEMA NU 4-2008 Comparison of Preclinical PET Imaging Systems." In: *Journal of Nuclear Medicine* 53.8 (June 2012), pp. 1300–1309. ISSN: 0161-5505. DOI: 10.2967/jnumed.111.099382. URL: http://dx.doi.org/10.2967/jnumed.111.099382.

[52] P. J. Green. "On Use of the EM for Penalized Likelihood Estimation." In: *Journal of the Royal Statistical Society. Series B (Methodological)* 52.3 (1990), pp. 443–452. ISSN: 00359246. URL: http://www.jstor.org/stable/2345668.

[53] T. Harion. "The STiC ASIC High Precision Timing with Silicon Photomultipliers." PhD thesis. Universität Heidelberg, July 2015. URL: http://www.ub.uni-heidelberg.de/archiv/19194.

[54] W. Shen. "Development of high performance readout ASICs for silicon photomultipliers (SiPMs)." PhD thesis. Universität Heidelberg, Dec. 2012. URL: http://www.ub.uni-heidelberg.de/archiv/14210.

[55] W. Shen et al. "STiC - A mixed mode chip for SiPM ToF applications." In: *2012 IEEE Nuclear Science Symposium and Medical Imaging Conference Record (NSS/MIC)* (Oct. 2012). DOI: 10.1109/nssmic.2012.6551231. URL: http://dx.doi.org/10.1109/NSSMIC.2012.6551231.

[56] M. D. Rolo et al. "TOFPET ASIC for PET applications." In: *Journal of Instrumentation* 8.02 (Feb. 2013), pp. C02050–C02050. ISSN: 1748-0221. DOI: 10.1088/1748-0221/8/02/c02050. URL: http://dx.doi.org/10.1088/1748-0221/8/02/C02050.

[57] M. Ritzert. "Development and Test of a High Performance Multi Channel Readout System on a Chip with Application in PET/MR." PhD thesis. 2014. URL: http://archiv.ub.uni-heidelberg.de/volltextserver/17092/.

[58] R. Becker et al. "The SAFIR experiment: Concept, status and perspectives." In: *Nuclear Instruments and Methods in Physics Research Section A: Accelerators, Spectrometers, Detectors and Associated Equipment* (May 2016). ISSN: 0168-9002. DOI: 10.1016/j.nima.2016.05.037. URL: http://dx.doi.org/10.1016/j.nima.2016.05.037.

[59] M. S. Judenhofer and S. R. Cherry. "Applications for Preclinical PET/MRI." In: *Seminars in Nuclear Medicine* 43.1 (Jan. 2013), pp. 19–29. ISSN: 0001-2998. DOI: 10.1053/j.semnuclmed.2012.08.004. URL: http://dx.doi.org/10.1053/j.semnuclmed.2012.08.004.

[60] S. A. Schelkunoff. "The Impedance Concept and Its Application to Problems of Reflection, Refraction, Shielding and Power Absorption." In: *Bell System Technical Journal* 17.1 (Jan. 1938), pp. 17–48. ISSN: 0005-8580. DOI: 10.1002/j.1538-7305.1938.tb00774.x. URL: http://dx.doi.org/10.1002/j.1538-7305.1938.tb00774.x.

[61] E. Rogers. *Understanding Buck Power Stages in Switchmode Power Supplies*. Application Report SLVA057. Texas Instruments. Mar. 1999.

[62] J. Williams. *Application Note 32: High Efficiency Linear Regulators*. Linear Technology Corporation. 1630 McCarthy Blvd., Milpitas, CA 95035-7417, USA, 1989.

[63] *Crystal Oscillator (XO) (10 MHZ TO 1.4 GHZ)*. 1.4. Silicon Labs. 400 West Cesar Chavez Austin, TX 78701 USA, May 2013.

[64] *Si5345/44/42 Rev D Data Sheet*. Silicon Labs. Silicon Laboratories Inc. 400 West Cesar Chavez Austin, TX 78701 USA. URL: http://www.silabs.com/documents/public/data-sheets/Si5345-44-42-D-DataSheet.pdf.

[65] L. Amaral et al. "The versatile link, a common project for super-LHC." In: *Journal of Instrumentation* 4.12 (Dec. 2009), P12003–P12003. ISSN: 1748-0221. DOI: 10.1088/1748-0221/4/12/p12003. URL: http://dx.doi.org/10.1088/1748-0221/4/12/P12003.

[66] L. Olantera et al. "Versatile transceiver production and quality assurance." In: *Journal of Instrumentation* 12.01 (Jan. 2017), pp. C01097–C01097. ISSN: 1748-0221. DOI: 10.1088/1748-0221/12/01/c01097. URL: http://dx.doi.org/10.1088/1748-0221/12/01/C01097.

[67] *Avago AFBR-57R5APZ Data Sheet*. Avago Technologies. 2013. URL: http://www.fit-foxconn.com/Images/Products/Spec/AFBR-57R5APZ_20160510175041137.pdf.

[68] A. P. Dempster, N. M. Laird, and D. B. Rubin. "Maximum Likelihood from Incomplete Data via the EM Algorithm." In: *Journal of the Royal Statistical Society. Series B (Methodological)* 39.1 (1977), pp. 1–38. ISSN: 00359246. URL: http://www.jstor.org/stable/2984875.

[69] K. Lange and R. Carson. "EM reconstruction algorithms for emission and transmission tomography." In: *Journal of Assisted Computed Tomography* 8.2 (Apr. 1984), pp. 306–316. URL: https://www.ncbi.nlm.nih.gov/pubmed/6608535.

[70] J. Fessler and A. Hero. "Penalized maximum-likelihood image reconstruction using space-alternating generalized EM algorithms." In: *IEEE Transactions on Image Processing* 4.10 (1995), pp. 1417–1429. ISSN: 1057-7149. DOI: 10.1109/83.465106. URL: http://dx.doi.org/10.1109/83.465106.

[71] R. Dekker. *A Simple Method to Measure Unknown Inductors*. English. June 2016. URL: http://www.dos4ever.com/inductor/inductor.html.